DYNAMICS OF A Z-PINCH DISCHARGE IN ARGON

by

CECIL CHARLES DAUGHNEY

B.Sc., University of New Brunswick, 1961

M.Sc., University of British Columbia, 1963

A THESIS SUBMITTED IN PARTIAL FULFILLMENT OF

THE REQUIREMENTS FOR THE DEGREE OF

DOCTOR OF PHILOSOPHY

in the Department

of

PHYSICS

We accept this thesis as conforming to the

required standard.

THE UNIVERSITY OF BRITISH COLUMBIA

May, 1966

In presenting this thesis in partial fulfilment of the requirements for an advanced degree at the University of British Columbia, I agree that the Library shall make it freely available for reference and study. I further agree that permission for extensive copying of this thesis for scholarly purposes may be granted by the Head of my Department or by his representatives. It is understood that copying or publication of this thesis for financial gain shall not be allowed without my written permission.

Department of Physics

The University of British Columbia
Vancouver 8, Canada

Date May 11, 1966

THE UNIVERSITY OF BRITISH COLUMBIA

FACULTY OF GRADUATE STUDIES

PROGRAMME OF THE

FINAL ORAL EXAMINATION

FOR THE DEGREE OF

DOCTOR OF PHILOSOPHY

of

CECIL CHARLES DAUGHNEY

B.Sc., The University of New Brunswick, 1961

M.Sc. The University of British Columbia, 1963

IN ROOM 303, HENNINGS BUILDING

WEDNESDAY, MAY 11, 1966, AT 9:30 A. M.

COMMITTEE IN CHARGE

Chairman: F. Noakes

B. Ahlborn
A. J. Barnard
F. L. Curzon
R. Howard
M. M. Z. Kharadly
R. A. Nodwell

External Examiner: A. Folkierski
Imperial College
University of London

Research Supervisor: F. L. Curzon

DYNAMICS OF A Z-PINCH DISCHARGE IN ARGON

ABSTRACT

A discussion of probe measurement of the magnetic field in a plasma is presented with particular reference to the perturbation of the magnetic field caused by the probe. A correction procedure is developed to compensate for this perturbation.

Using magnetic probes, radial variation of the current density distributions are obtained for an argon plasma in a z-pinch discharge. Initial argon pressures of 100, 250, and 500 μHg are investigated. The current density distributions are determined for 1 μsec intervals between the initiation of the discharge and the occurrence of the first pinch. These current density distributions are compared with photographic observations.

The experimental results are discussed in terms of the snowplow model and the shock wave model. Mathematically, the non-linear snowplow equation is solved using an approximation technique which results in analytic solutions. The shock wave equation is solved by a graphical technique. An extension of the shock wave model is proposed for a better understanding of the experimental results.

GRADUATE STUDIES

Field of Study: Physics

Non Linear Systems	A. C. Soudack
Electronic Instrumentation	F. Bowers
Statistical Mechanics	R. Barrie
Advanced Plasma Physics	A. J. Barnard

PUBLICATIONS

1. Simple Method of Overcoming the Effects of Noise Signals Produced by Spark Gap Switches - F.L. Curzon and C.C. Daughney; Rev. Sci. Instr. 34, 430, 1963.

2. Triggering System for Pulsed Discharge Circuit S.S. Medley, F.L. Curzon and C.C. Daughney; Rev.Sci.Instr. 36, 713, 1964.

3. Investigation of Noise Signals in Pulsed Discharge Devices - S.S. Medley, F.L. Curzon, and C.C. Daughney; Can.J.Phys. 43, 1882, 1965.

ABSTRACT

A discussion of probe measurement of the magnetic field in a plasma is presented with particular reference to the perturbation of the magnetic field caused by the probe. A correction procedure is developed to compensate for this perturbation.

Using magnetic probes, radial current density distributions are obtained for an argon plasma in a z-pinch discharge. Initial argon pressures of 100, 250, and 500 μHg are investigated. The current density distributions are determined for 1 μsec intervals between the initiation of the discharge and the occurrence of the first pinch. These current density distributions are compared with photographic observations.

The experimental results are discussed in terms of the snowplow model and the shock wave model. Mathematically, the non-linear snowplow equation is solved using an approximation technique which results in analytic solutions. The shock wave equation is solved by a graphical technique. An extension of the shock wave model is proposed for a better understanding of the experimental results.

THE DYNAMICS OF A Z-PINCH DISCHARGE IN ARGON

		PAGE
	ABSTRACT	i
	TABLE OF CONTENTS	ii
	LIST OF ILLUSTRATIONS	iv
	LIST OF TABLES	vi
	ACKNOWLEDGEMENT	vii
1.0	INTRODUCTION	1
PART I	MAGNETIC PROBE MEASUREMENT	8
2.0	INTRODUCTION	9
3.0	MAGNETIC PROBES	9
3.1	MEASURING CIRCUIT	11
3.2	MAGNETIC PROBE ERROR	15
4.0	ANALOGUE EXPERIMENT	18
4.1	APPARATUS	20
4.2	EXPERIMENTAL RESULTS	22
4.3	THEORETICAL MODEL	30
4.4	CONCLUSIONS	33
5.0	MAGNETIC FIELD CORRECTION	36
5.1	NUMERICAL COMPUTATION	38
5.2	TEST FOR NUMERICAL PROGRAM	47
PART II	EXPERIMENTAL RESULTS	51
6.0	INTRODUCTION	52
7.0	APPARATUS	53
7.1	DISCHARGE PARAMETERS	60
8.0	MAGNETIC PROBE MEASUREMENT	67
8.1	MAGNETIC PROBE CALIBRATION	75
8.2	COMPUTED RESULTS	78
8.3	ANALYSIS OF ERROR	92
9.0	PHOTOGRAPHIC MEASUREMENT	103
9.1	MAGNETIC PROBE PERTURBATION	104
9.2	COLLAPSE CURVES	108
9.3	SHOCK VELOCITY MEASUREMENT	109

THE DYNAMICS OF A Z-PINCH DISCHARGE IN ARGON
(CONT'D.)

		PAGE
10.0	COMPARISON OF MAGNETIC PROBE AND FRAMING CAMERA RESULTS	115
10.1	DETERMINATION OF SHOCK AND FLOW VELOCITIES	120
10.2	DETERMINATION OF ELECTRIC FIELD	123
PART III	COMPARISON OF THEORETICAL MODELS WITH EXPERIMENTAL RESULTS	128
11.0	INTRODUCTION	129
12.0	THEORETICAL MODELS	130
13.0	DYNAMIC EQUATIONS FROM SNOWPLOW MODEL	132
13.1	ANALYTIC SOLUTION OF EQUATIONS	135
13.2	COMPARISON OF THEORETICAL AND EXPERIMENTAL RESULTS	144
14.0	DYNAMIC EQUATIONS FROM SHOCK WAVE MODEL	156
14.1	GRAPHICAL SOLUTION OF EQUATIONS	162
14.2	COMPARISON OF THEORETICAL AND EXPERIMENTAL RESULTS	168
15.0	PROPOSED MODEL OF THE Z-PINCH DISCHARGE	171
PART IV	CONCLUSIONS	184
16.0	DISCUSSION OF RESULTS	185
17.0	FINAL CONCLUSIONS	190
18.0	PROPOSALS FOR FUTURE WORK	193
APPENDIX I	CONSTRUCTION OF MAGNETIC PROBE	196
APPENDIX II	NUMERICAL PROGRAMS IN FORTRAN LANGUAGE	198
	REFERENCES	203

LIST OF ILLUSTRATIONS

FIGURE		PAGE
1	EXPERIMENTAL CONFIGURATION	2
2	MAGNETIC PROBE	10
3	MAGNETIC PROBE MEASURING CIRCUIT	12
4	FREQUENCY RESPONSE CURVES	14
5	ANALOGUE AND Z-PINCH GEOMETRY	19
6	PHOTOGRAPH OF ANALOGUE EXPERIMENT	21
7	EQUIVALENT CIRCUIT OF ANALOGUE EXPERIMENT	22
8	MAGNETIC PROBE ROTATION	24
9	ANALOGUE EXPERIMENTAL RESULTS	26
10	UNPERTURBED MAGNETIC FIELD	27
11	$\|C(z)\|$ VS $\|z\|$ ($\rho_0 = .35$)	28
12	$\|C(z)\|$ VS $\|z\|$ ($\rho_0 = .45$)	29
13	$\|C(z)\|$ VS $\|z\|$ (THEORETICAL CURVES)	32
14	$\|C(z)\|$ VS $\|z\|$ (THEORY AND EXPERIMENT $\rho_0 = .35$)	34
15	$\|C(z)\|$ VS $\|z\|$ (THEORY AND EXPERIMENT $\rho_0 = .45$)	35
16	SHEET APPROXIMATION TO CONTINUOUS CURRENT DENSITY DISTRIBUTION	39
17	ERROR IN NUMERICAL APPROXIMATION TO CORRECTION	45
18	MODIFICATION OF CORRECTION NEAR AXIS	46
19	ANALOGUE TEST CURVE	48
20	TOTAL FIELD CORRECTION	50
21	PHOTOGRAPH OF APPARATUS	54
22	SCHEMATIC DIAGRAM OF APPARATUS	55
23	FRAMING CAMERA AND CONTROL EQUIPMENT	57
24	OSCILLOSCOPE TRACE OF DISCHARGE CURRENT	62
25	OSCILLOSCOPE TRACE OF DISCHARGE VOLTAGE	64
26	OSCILLOSCOPE TRACE OF DISCHARGE LUMINOSITY	65
27	OSCILLOSCOPE TRACE OF MAGNETIC FIELD	68
28	COMPENSATED ATTENUATOR	69
29	UPPER AND LOWER OSCILLOSCOPE TRACES SUPERPOSED	71
30	FOUR SUPERPOSED OSCILLOSCOPE TRACES	71
31-33	MEASURED MAGNETIC FIELD DISTRIBUTION	72
34	CALIBRATION FOR MAGNETIC PROBE	76
35	MAGNETIC FIELD CORRECTION AT WALL OF VESSEL	79
36	RESULTS FROM TWO METHODS OF SOLUTION	80
37-42	CORRECTED CURRENT DENSITY DISTRIBUTIONS	82
43-45	CORRECTED MAGNETIC FIELD DISTRIBUTIONS	89
46	MEASURED AND COMPUTED DISTRIBUTIONS	93
47	SIMULATED HIGH CONDUCTIVITY INSIDE CURRENT SHEET	95
48	PLASMA INSTABILITY	98
49	ESTIMATED ERROR IN J DUE TO ERROR IN B	100
50	DEPENDENCE OF CURRENT DENSITY UPON MAGNETIC FIELD GRADIENT.	102
51	SIDE-ON PHOTOGRAPH OF PROBE	105
52	TOP-ON PHOTOGRAPH OF PROBE	105
53	END-ON PHOTOGRAPH OF PROBE	109

LIST OF ILLUSTRATIONS
(CONT'D.)

FIGURE		PAGE
54	COLLAPSE CURVES	110
55	RADIAL POSITION OF SHOCK FRONT	114
56	MEASUREMENT OF FORMATIVE TIME DELAY	117
57	EFFECT OF AMPLIFIER DELAY	119
58	RADIAL POSITION OF SHOCK FRONT VS TIME	121
59	RADIAL POSITION OF CURRENT DENSITY MAX.VS TIME	122
60	GRAPHICAL SOLUTION FOR w_1	142
61-63	COMPARISON OF THEORETICAL AND EXPERIMENTAL RESULTS	148
64	MODIFIED DISCHARGE CIRCUIT	152
65	SHOCK WAVE PARAMETERS	157
66	GRAPHICAL SOLUTION OF SAHA EQUATION	165
67	GRAPHICAL SOLUTIONS OF RANKINE-HUGONIOT RELATIONS	166
68	DISCONTINUITY IN PLASMA COLUMN	172
69	ELECTROMAGNETIC FIELDS IN THE JOULE REGION	174
70	PLASMA PARAMETERS IN JOULE REGION	180

LIST OF TABLES

TABLE		PAGE
I	APPARATUS	58
II	DETERMINATION OF PINCH TIME WITH PHOTOMULTIPLIER	63
III	RADIAL POSITIONS OF CURRENT DENSITY FEATURES	88
IV	COMPARISON OF COMPUTED CURRENT DENSITY FROM TWO MEASUREMENTS OF MAGNETIC FIELD	101
V	RADIAL POSITION OF SHOCK FRONT	115
VI	FORMATIVE TIME DELAY	118
VII	SHOCK FRONT AND PARTICLE FLOW VELOCITIES	123
VIII	DETERMINATION OF ELECTRIC FIELD	126
IX	DETERMINATION OF $k(\rho_0)$	141
X	DETERMINATION OF λ	154
XI	MODIFIED SNOWPLOW CALCULATION	155
XII	SHOCK WAVE PARAMETERS	157
XIII	VALUES OF STATISTICAL WEIGHTS	161
XIV	FLOW VELOCITY BEHIND SHOCK	168
XV	THICKNESS OF THE SHOCK HEATED PLASMA	169
XVI	APPARENT CONDUCTIVITY IN JOULE REGION	173
XVII	"ELECTRIC FIELD PRESSURE"	176

ACKNOWLEDGEMENT

It is a pleasure to acknowledge the stimulating supervision provided by Dr. F. L. Curzon throughout these investigations. It is a pleasure also to acknowledge the assistance of the faculty members and students of the plasma physics group. In particular, I wish to thank Dr. R. A. Nodwell and Dr. A. J. Barnard for their improvements in the presentation of the thesis.

I wish to thank Mr. W. Ratzlaff, Mr. J. Lees, Mr. P. Haas, and Mr. A. Fraser for their part in the construction of the apparatus.

I gratefully acknowledge the financial assistance awarded by the National Research Council.

REFERENCES

In the text, references are denoted by,

First Author (Year)

i.e. Allen (1957)

An alphabetical list of the complete references are given on page 203.

1.0 INTRODUCTION

The thesis is organized into four parts as outlined in the Table of Contents. However, a reading of this introduction and the conclusion (Part IV) will be sufficient for an understanding of the principal results.

The investigation which we describe belongs to the branch of physics known as plasma physics, i.e. the study of phenomena associated with ionized gases. In particular, we study the behaviour of the plasma in a z-pinch discharge. This is one of several experimental configurations where a magnetic field is used to confine the plasma. In this case, the plasma is sustained by an axial current, I (see figure 1.), which results from the discharge of energy from a capacitor bank. The self-induced magnetic field, B_θ, interacts with the axial current producing a radial force, F_r; and this force causes the plasma to constrict to a small volume along the axis of the discharge vessel. This constriction of the plasma is known as the "pinch effect".

The z-pinch discharge was first introduced in the hope of creating a thermonuclear plasma (eg. Anderson (1957)), but recent work has revealed the impracticality of these plans. The device is now used to produce a large volume of high temperature plasma which has a well defined geometry, and such a plasma is suitable for the present study of "plasma dynamics". "Plasma dynamics" refers to the motion of the plasma as a whole as opposed to the motion of the individual ions and electrons.

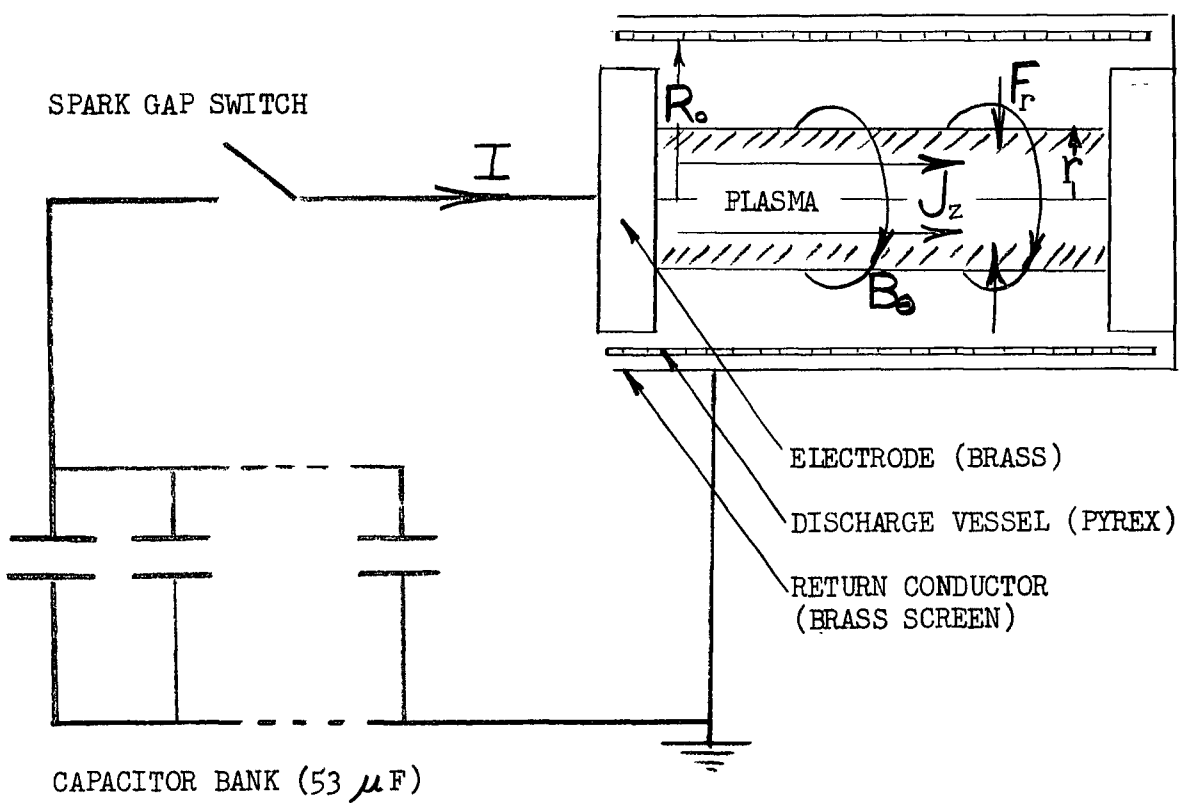

FIGURE 1. EXPERIMENTAL CONFIGURATION

J_z = Axial Current Density
B_θ = Azimuthal Magnetic Field
F_r = Radial (J_z x B_θ) Force
R_o = Radius of Discharge Vessel
r = Radius of Plasma Column
I = Discharge Current

1.0 INTRODUCTION (CONT'D.)

In this investigation we are interested in the dynamics of the pinch effect. We wish to obtain a more complete physical model of the collapsing plasma than is now available, and we wish to estimate the temperature, density, and degree of ionization of the plasma in the z-pinch discharge. In this study we must know the forces which arise from the flow of electric current and thus we must know the current density distribution as a function of time in the discharge vessel. This is the chief objective of the present investigation.

The current density distribution can be computed from the associated magnetic field distribution, and this magnetic field can be determined experimentally with the use of "magnetic probes". A magnetic probe is simply a small coil of wire which has an output voltage proportional to the change of magnetic flux through the coil. As these probes are the principal experimental tool, Part I of the thesis is a discussion of their limitations and the precautions required in their use.

The most serious problem associated with magnetic probe measurement is that the probe must be immersed in the plasma, perturbing it, and therefore modifying the magnetic field which it is supposed to measure. An appreciable modification occurs because no electric current can flow in the space occupied by the probe. The probe presents a non-conducting "hole" to the current flowing through the highly conducting plasma. This effect is investigated in detail in the analogue experiment described in section 3.

1.0 INTRODUCTION (CONT'D.)

In the analogue experiment we set up a well defined current density distribution with two concentric cylindrical sheets which carry equal and opposite electrical currents. The true magnetic field, i.e. that which would exist in the absence of a probe, can be calculated. The perturbed magnetic field can be measured. (The probe "punctures" the current sheets). Hence the difference of these two magnetic field distributions gives the correction for the magnetic field of a given current sheet. Knowledge of this correction allows us to correct the magnetic field measured by the probe in the z-pinch discharge. In this case, a total magnetic field correction is obtained by integrating the corrections from each element of current (chosen to be a cylindrical sheet) over the whole current density distribution. This integration is performed by a numerical procedure and it is discussed in section 5.

Using one of the analogue experimental curves in the numerical correction procedure we can test the accuracy of the correction. The computed current density distribution is compared with the known current distribution of the single current sheet of a given radius. Thus we conclude Part I knowing that we can correct the measured magnetic field which we obtain with a given magnetic probe.

In Part II we present all results of experimental measurement on the z-pinch discharge. The probe measures the magnetic field as a function of time at the radial position of the probe coil. However, as the z-pinch discharge is reproducible from discharge to discharge

we can construct a plot of magnetic field as a function of radius for a given time. The magnetic field distribution is obtained at 1μsec intervals up to the pinch time (the time required for the first constriction of the plasma) for each of three initial pressures of argon (100,250 and 500μHg.) We correct these measured results and we compute the radial current density distribution from the corrected magnetic field. These current density distributions have two interesting properties. First, there is a distinct current density maximum, and second, there is a region of almost constant current density - a "plateau" region. (See figures 37-42).

We supplement the magnetic probe technique with photographic techniques which have been used previously on the z-pinch discharge. First, a very high speed framing camera allows us to photograph the radius of the luminous plasma as a function of time. (Curzon (1962)). Secondly, an extension of this technique has been developed by Folkierski (1963) which allows us to observe the propagation of the shock front in the discharge plasma. We expect to observe such a shock front in the z-pinch discharge because of the rapid radial motion of the collapse (typically 10^4 meter per sec.). We conclude Part II with a correlation of the prominent features of the current density distribution with those of the photographic measurements.

In Part III we use two theoretical models to predict the experimentally measured plasma dynamics. These predictions compare favourably with the observed results and thus we are justified in

in using these theoretical models to obtain additional information about the plasma (for example, temperature and density).

The first theoretical model is the snowplow model of Rosenbluth (1954). The current is assumed to form a very thin sheet near the vessel wall which then collapses toward the axis of the vessel gathering all the gas as it does so. With this model, we can develop both an equation of motion for the collapsing current sheet and an equation for the current in the discharge circuit. These two equations must be solved simultaneously for the radius of the current sheet and the discharge current as functions of time. An approximation technique is used to solve these second order differential equations - one of which is non linear.

The second theoretical model is known as the shock wave model and it has been discussed in connection with shock tube flow by Reynolds (1961). In simple shock theory, the Rankine-Hugoniot relations are derived from the conservation of mass, momentum, and energy across the shock discontinuity. In a plasma, these relations must be supplemented by Saha's equation for the determination of the microscopic constituents of the plasma. We solve these equations with a graphical technique.

Both of these models provide useful concepts for the understanding of the z-pinch discharge. However, neither of the models predicts the relatively large thickness of the luminous plasma, the "plateau" region of the current density distribution or the unusual dependence

upon initial pressure and time of the electric field in the plasma. These facts lead us to propose a new model of the plasma in the collapse stage of the z-pinch discharge. The model is characterized by two distinct layers. The inner layer has a higher particle density and a lower temperature than the outer layer. The model is discussed in section 15.0 with particular reference to peculiarities mentioned above.

Finally, in Part IV we present the conclusions of our investigation.

PART I

MAGNETIC PROBE MEASUREMENT

2.0 INTRODUCTION

It is recognized that the introduction of a probe into a plasma must cause some perturbation, and indeed, Ecker (1962) has shown this to be the case in a theoretical treatment of probe error. However, he has used a numerical technique to solve the problem and this is not easily adaptable to a given experimental configuration.

In this Part of the thesis, we first describe our magnetic probe (section 3) and then examine the probe perturbation by means of an analogue experiment (section 4). The results of the analogue experiment compare extremely well with the simple case of a plane current sheet punctured by a probe as examined theoretically by Malmberg (1964) (section 4.3). Finally we develop the numerical program for the application of these results to the z-pinch discharge (section 5).

3.0 MAGNETIC PROBES

A magnetic probe consists of a small wire coil which must be supported and shielded inside the plasma in a manner, for example, as described by Segre (1960) or as illustrated in figure 2. The details of construction are given in Appendix I, but a few of the most important ideas are presented here.

The probe is shielded mechanically from the hot plasma by a quartz guide tube (see figure 5) and it is shielded electrically by a very thin silver film which is at ground potential. The thickness of the silver film ($\sim 10^{-3}$ m.m.) is much less than the skin depth ($\sim 10^{-1}$ m.m.)

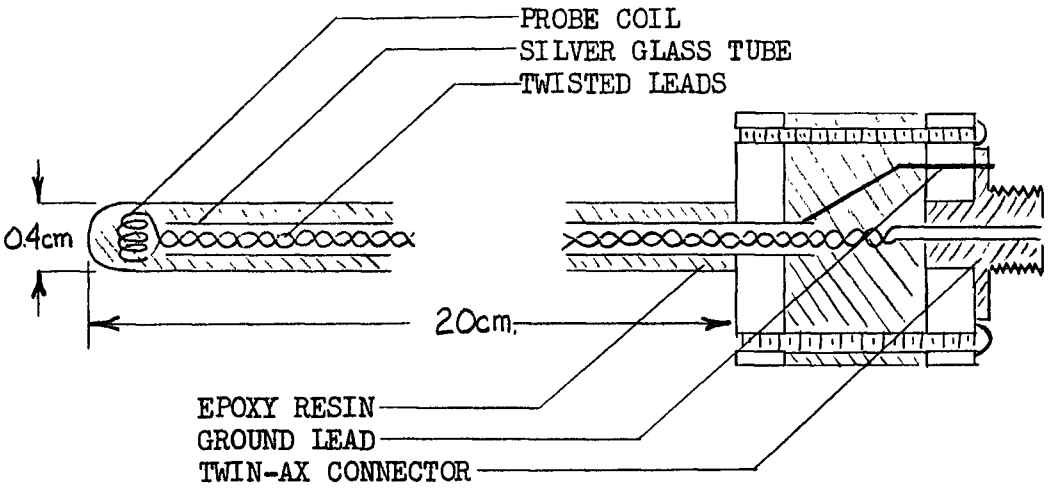

FIGURE 2. MAGNETIC PROBE

3.0 MAGNETIC PROBES (CONT'D.)

and thus no currents are induced in the shield which would perturb the magnetic field at the probe coil. It is possible to obtain undesireable signals which are caused by magnetic flux threading through the probe leads. These signals may be eliminated by tightly winding together the leads to the probe coil. In this way the flux through one loop in the leads approximately cancels the flux through the adjacent loop, and the net noise signal is zero.

The magnetic probe produces an output voltage which is proportional to the rate of change of magnetic flux passing through the plane of the probe coil. Thus the integral of the probe signal

3.0 MAGNETIC PROBES (CONT'D.)

is proportional to the magnetic field. The integration is performed by a simple RC-circuit with a time constant of 112 μsec (see figure 3).

3.1 MEASURING CIRCUIT

In the presence of pulsed discharge circuits, such as the z-pinch discharge, there are two sources of noise signals which distort the experimental signal and must, therefore, be eliminated. The first source of noise is "capacitative pickup". There will be a stray capacitance (C) between the discharge circuit and the measuring circuit and as the voltage (V) on the discharge circuit and the discharge frequency (w) are very high (approximately 10^4 volts and 10^5 c/sec respectively), the resulting noise signals ($\propto$wCV) on the measuring circuit may be appreciable. The second source of noise is "radiative pickup". High frequency noise signals are radiated when the spark gap switch in the discharge circuit (see figure 1) is "closed" initially. See, for example, Medley (1965).

Capacitative pickup can be eliminated by using the balanced differential circuit which is shown in figure 3. An "A-B", D-type Tektronix preamplifier is used in the oscilloscope, and further, the integrators are provided with a rheostat which is adjusted to give an optimum common mode rejection of approximately 10^4:1 for frequencies ranging from approximately 10^2 to 10^5 cps.

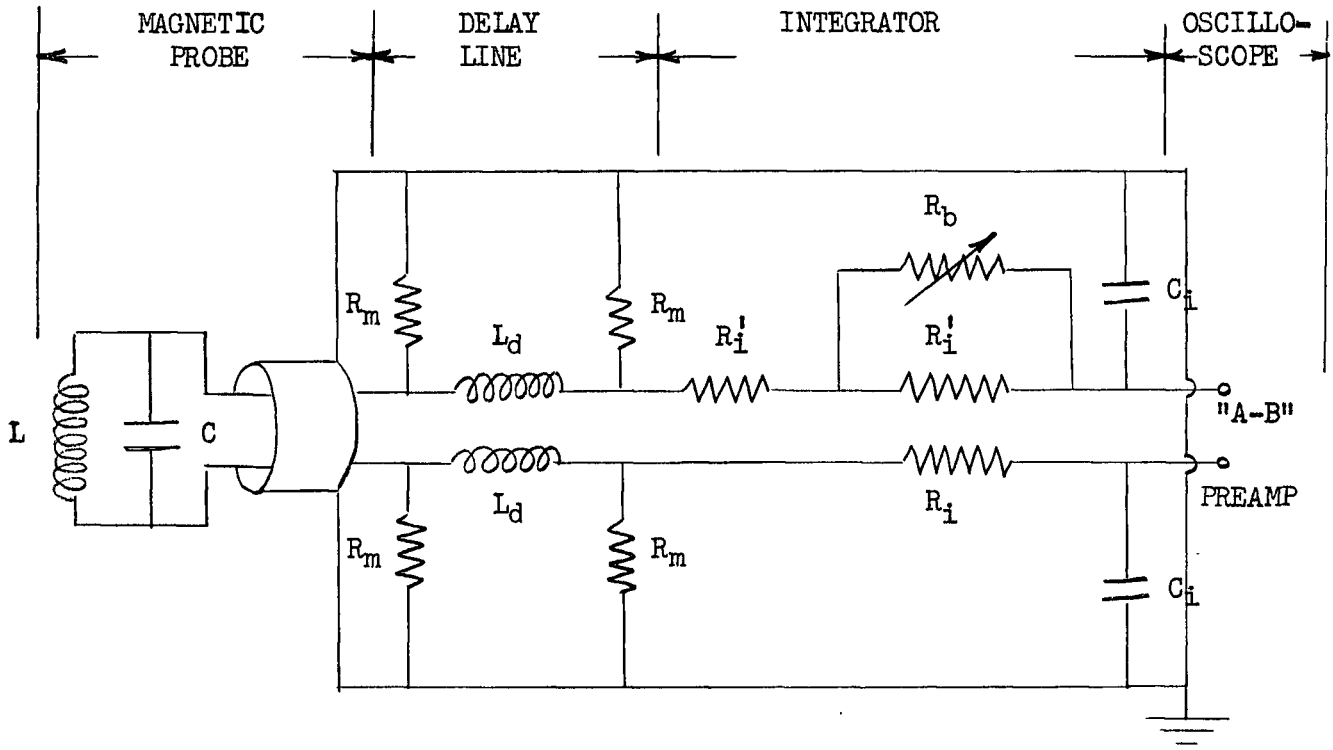

FIGURE 3. MAGNETIC PROBE MEASURING CIRCUIT

L,C = A.C. equivalent circuit of magnetic probe
L = .45 μH
C = 15 pF

R_m = Matching resistance = 220Ω
L_d = .5 μsec delay line

R_i = Integrating resistance = 2.2 kΩ
R_i' = Integrating resistance = 1.5 kΩ
R_b = Balancing resistance = 0 - 2.5 kΩ
C_i = Integrating capacitor = .05 μF

3.1 MEASURING CIRCUIT (CONT'D.)

Radiated noise signals are minimized by coaxiallizing the main spark gap switch and the triggering circuitry (see figure 27). The measuring circuit is also coaxiallized and shielded. These precautions reduce the noise signal but it is still significant for 0.5 μsec. Thus the measuring circuit of figure 3 is provided with a 0.5 μsec delay line which allows the desired signal to be delayed until the radiated noise signal has decayed. A complete discussion of noise signals and elimination of noise signals is given by Medley (1965b).

The frequency response of the measuring circuit must also be examined. If we consider first the probe and delay line, then we wish the output to be proportional to the input for all frequencies. The input signal will be proportional to dB/dt. However, the probe has an inductance and capacitance, and therefore it has a resonance at a particular frequency. Following the procedure outlined by Segre (1960), we can critically damp this resonance by terminating the probe with its characteristic impedance of 120Ω. Similarly, however, the delay line has a resonant frequency and a characteristic impedance of 220Ω.

In our experiment we terminate the delay line properly and we measure the frequency response of the probe and delay line to check that it remains "flat" up to frequencies of approximately 10^6cps. This is sufficient for a study of magnetic field signals associated with the z-pinch discharge. It can be seen in figure 4 that the

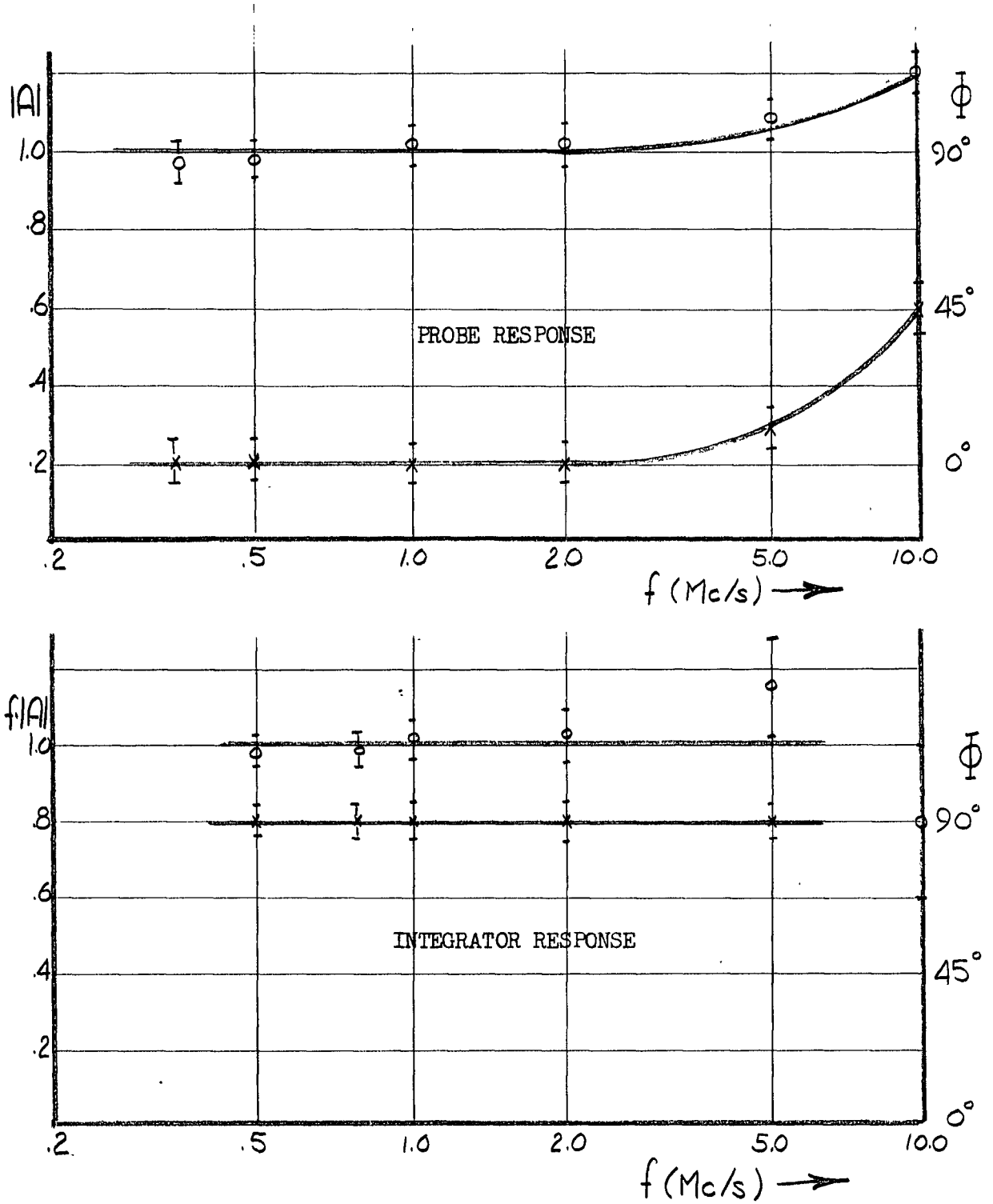

FIGURE 4. FREQUENCY RESPONSE CURVES

Φ = Phase shift
$|A|$ = Gain
f = Frequency

3.1 MEASURING CIRCUIT (CONT'D.)

frequency response is "flat" up to approximately 5×10^6 cps and that the measuring circuit introduces no phase change below this frequency. (Note: If it were necessary, the frequency response could be improved by terminating both probe and delay line with their respective characteristic impedances, but this procedure further attenuates the signal.)

We have shown now that the output signal from the probe and delay line is a faithful representation of the input signal. However, the input signal is proportional to dB/dt and we are interested in measuring B. Thus we integrate the signal with the RC network shown in figure 3. The condition for faithful integration is that the product of gain and frequency should be constant for all frequencies and furthermore the integrator should introduce a 90° phase change in signals of all frequencies. Both of these conditions are fulfilled as may be seen in figure 4.

We are justified in considering these two portions of the measuring circuit separately as the integrator presents a large impedance to the delay line and hence does not "load" it when the two circuits are used together as shown in figure 3.

3.2 MAGNETIC PROBE ERROR

The most serious problem in probe measurement of the current density distribution is the perturbation of the current caused by the presence of the probe in the plasma. In the literature, the

problem has received only preliminary investigation. Lovberg (1959) suggested that only a small error in the magnetic field would occur, because the field at any point is largely determined by contributions from the more remote portions of the current density. However, when Ecker (1962) considered the problem theoretically, he found the probe error to be appreciable, particularly for the region at the boundary of the current distribution.

Ecker considered a time independent current distribution and he calculated the magnetic field resulting from the flow of current around the magnetic probe. He also calculated the magnetic field for the unperturbed current distribution and the difference of these two fields he called the probe error. The calculations were performed numerically on several rotationally symmetric current distributions. Although Ecker's results illustrate the importance of considering probe error, they are impractical for use in the correction of experimentally measured magnetic fields. The chief advantage of the error considerations in the following two sections of this thesis is that they may be readily applied to any linear or inverse pinch device.

Ecker introduced terminology which will be useful in the following descriptions. "Boundary error" refers to the error introduced in the magnetic field when a non-conducting hole is formed in a conducting medium. "Conductivity error" refers to the error in the magnetic field caused by the cooling effect of impurities from the probe which

are "boiled off" into the plasma. Note that the impurities effectively increase the radius of the low conductivity hole. Hence we can combine the treatment of conductivity error with that of boundary error by considering the boundary error caused by an effective probe size which is greater than the actual probe size.

Experimentally, the problem has received little attention. Harding (1958) examined the influence of two probes, one upon the other, for probe separations of approximately 70 cm. He observed no change in the general field configuration at one probe when the other probe was introduced into the plasma. Dippel (1959) performed an analogue experiment to investigate the effect of the probe on measurement of the magnetic field. He investigated the field associated with a cylindrical conductor of known conductivity. The field was measured for several diameters of the probe hole and these results were then compared with the theoretical magnetic field. The theoretical magnetic field is easily calculated as the skin depth of the current distribution in the conductor is known. He repeated the experiment for conductors of various conductivity and he concluded that the probe error becomes negligible only for large skin depths, i.e. low conductivity. From his data we observe that the measured magnetic field is approximately independent of the conductivity over the range of 2×10^4 mho/m to 4×10^7 mho/m which he has examined. This implies that in all cases the skin depth is small compared to the characteristic length of the field correction (see section 4.2, figure 9) and thus we can consider his current distribution to be a

sheet like our proposed analogue experiment. It is then encouraging to observe in his data that the probe error is insensitive to the exact radius of the probe hole. The probe error varies by approximately 50% when the probe radius varies by approximately 80%. Thus it appears that the effective probe radius is not critical and a rough estimate of conductivity error will be sufficient. We concentrate upon an examination of boundary error with the intention of compensating for the error rather than trying to reduce the error to a negligible effect.

In compensating for the error it is advantageous to make the probe perturbation as geometrically simple as possible. In the actual discharge vessel, a quartz tube is placed diametrically through the vessel and the magnetic probe is moved within the tube (see figure 5). In this way the perturbation of the plasma is independent of the probe position. A similar arrangement is used in the analogue experiment and this is discussed in the next section.

4.0 ANALOGUE EXPERIMENT

The purpose of the analogue experiment is to investigate the effect of the above described boundary error on a well defined current distribution and hence on a known "true" magnetic field. As the experiment is designed to correct measurement on the z-pinch discharge which is characterized by a rotationally symmetric current sheet, the analogue magnetic field is defined by two concentric cylinders of aluminum foil (see figure 5). The outer cylinder

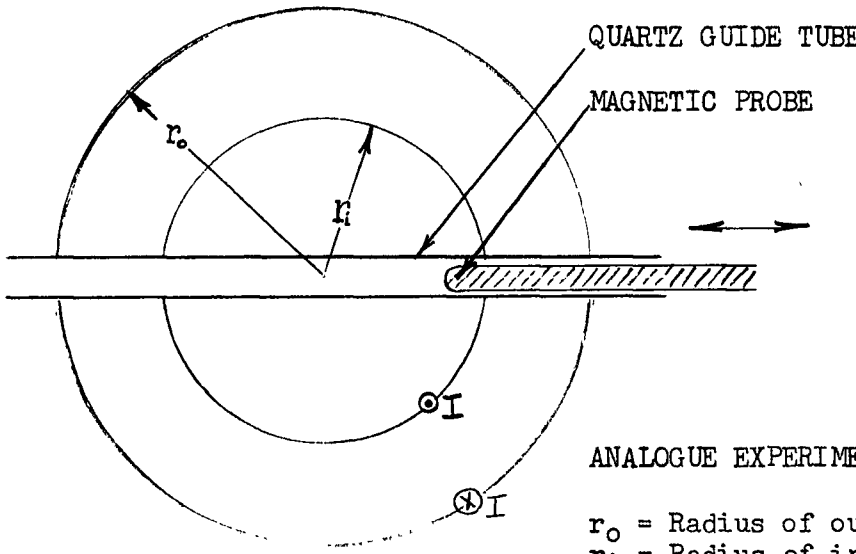

ANALOGUE EXPERIMENT

r_o = Radius of outside sheet = 9 cm.
r_i = Radius of inside sheet
I = Current

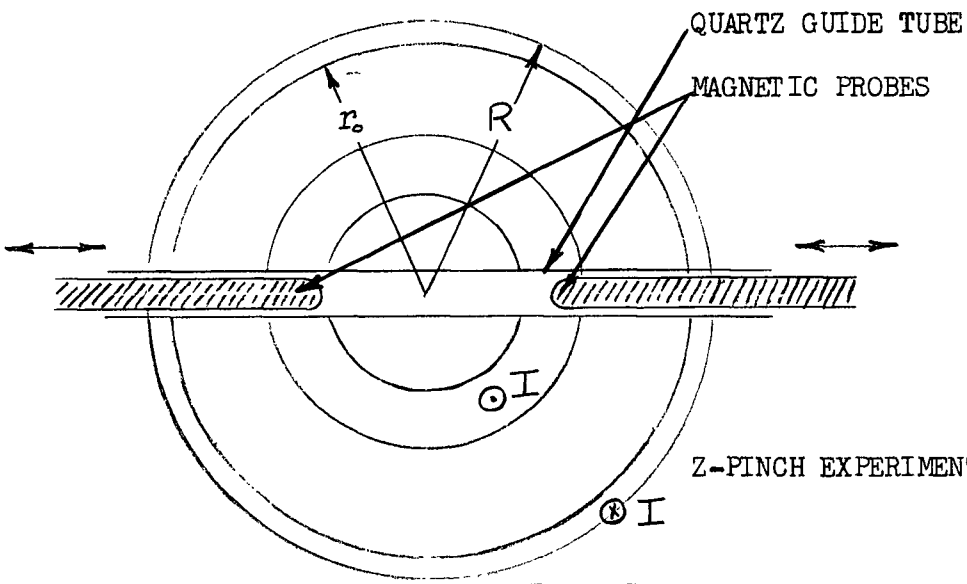

Z-PINCH EXPERIMENT

R = Radius of return conductor = 8.5 cm.
r_o = Radius of discharge vessel = 7.5 cm.
I = Discharge current

FIGURE 5. ANALOGUE AND Z-PINCH GEOMETRY

4.0 ANALOGUE EXPERIMENT (CONT'D.)

represents the return conductor of the actual discharge circuit and the inner conductor, which can be varied in diameter, corresponds to the plasma current.

A sinusoidal current supply is available and it is desireable to use the magnetic probes which will be used in the later experiments. The frequency (w) of the supply is approximately $4 \times 10^{7} sec^{-1}$ The output voltage (V) from the probe is given by:

$$Ve^{jwt} = KwIe^{jwt}$$

where K, a geometrical factor, is 2.5×10^{-10} h.

I is the current in the sheet, and,

w is the frequency of oscillation.

For an output voltage of approximately 10^{-2} volts which allows use of an oscilloscope, the required current (I) is of the order of 1 amp. Such a current at this frequency suggests that the concentric conductors of the analogue experiment be included as the inductance of a parallel resonant circuit.

4.1 APPARATUS

The analogue experiment is scaled to approximate the actual experiment. The outer aluminum conductor has a radius of 9.1 cm. and the inner conductor radius can be selected from any of 1.4, 2.6, 4.1, 5.3, and 6.8 cm. These conductors are 60 cm in length and approximately .02 mm thickness. A photograph of the experiment is shown in figure 6 and an equivalent electrical circuit is shown in figure 7.

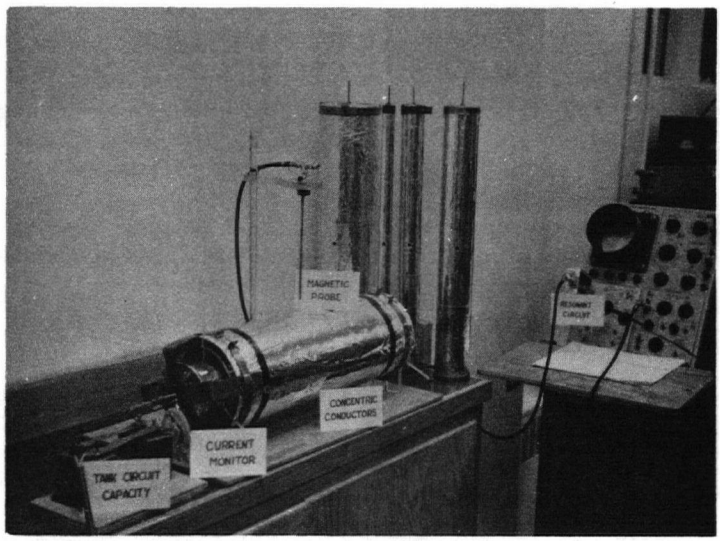

FIGURE 6. PHOTOGRAPH OF ANALOGUE EXPERIMENT

4.1 APPARATUS (CONT'D.)

The coaxial conductors form part of a parallel resonant circuit and the power supply has a variable frequency range which allows tuning to the resonant frequency for each of the various inner conductors. To increase further the output signal voltage, a series resonant circuit is used as shown in figure 7. This circuit can also be tuned to the resonant frequency of the analogue circuit. A Rogowski coil is used to monitor the current in the analogue circuit while measurement of the magnetic field is taken.

As in the actual discharge, a glass tube is placed diametrically through the concentric aluminum sheets and the probe can be moved

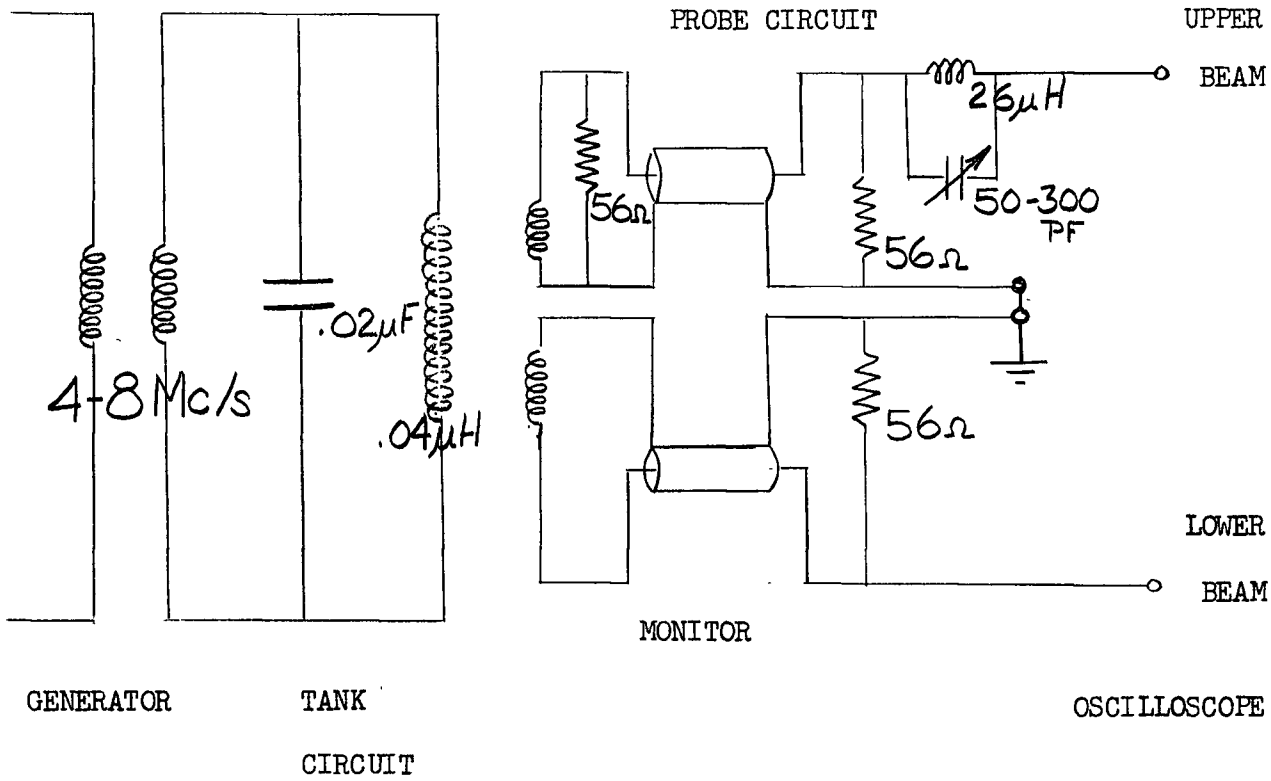

FIGURE 7. EQUIVALENT CIRCUIT OF ANALOGUE EXPERIMENT

4.1 APPARATUS (CONT'D.)

within it. The experiment consists of measuring the probe output as a function of radial position both inside and outside the current carrying conductors. A travelling microscope is used to measure probe positions and a dual beam oscilloscope is used to observe the probe and monitor signals.

4.2 EXPERIMENTAL RESULTS

In the analogue experiment we are trying to determine the correction for the magnetic field ($\Delta B(r)$), which is defined as the difference between the unperturbed or true magnetic field (Bu(r))

and the perturbed or measured magnetic field (Bp(r)). For the region between the concentric cylinders, see figure 5, the unperturbed magnetic field is known from Amperes law to fall off as $1/r$. The perturbed field, so called because of the circular hole punched in the aluminum conductor for the probe, is measured as described in section 4.1. Hence, the correction is easily obtained for a thin cylindrical current sheet as the difference between these two fields.

Before we proceed with the experiment, the output of the magnetic probe should be checked to ensure that the only coupling between the probe and the analogue circuit is provided by magnetic flux through the probe coil. In section 3.0 we have discussed two further possibilities for coupling. We have attempted to avoid capacitative coupling by using a grounded shield around the probe and we have attempted to avoid voltages induced in the probe leads by tightly winding the leads together. It is the effectiveness of these precautions which we wish to check.

If we rotate the magnetic probe about its own axis when the probe coil is held at a given radial position between the conductors of the analogue experiment, then we expect the signal to vary as shown in figure 8A. Note that we observe only the amplitude of the probe signal by choosing a sufficiently slow sweep rate of the oscilloscope.

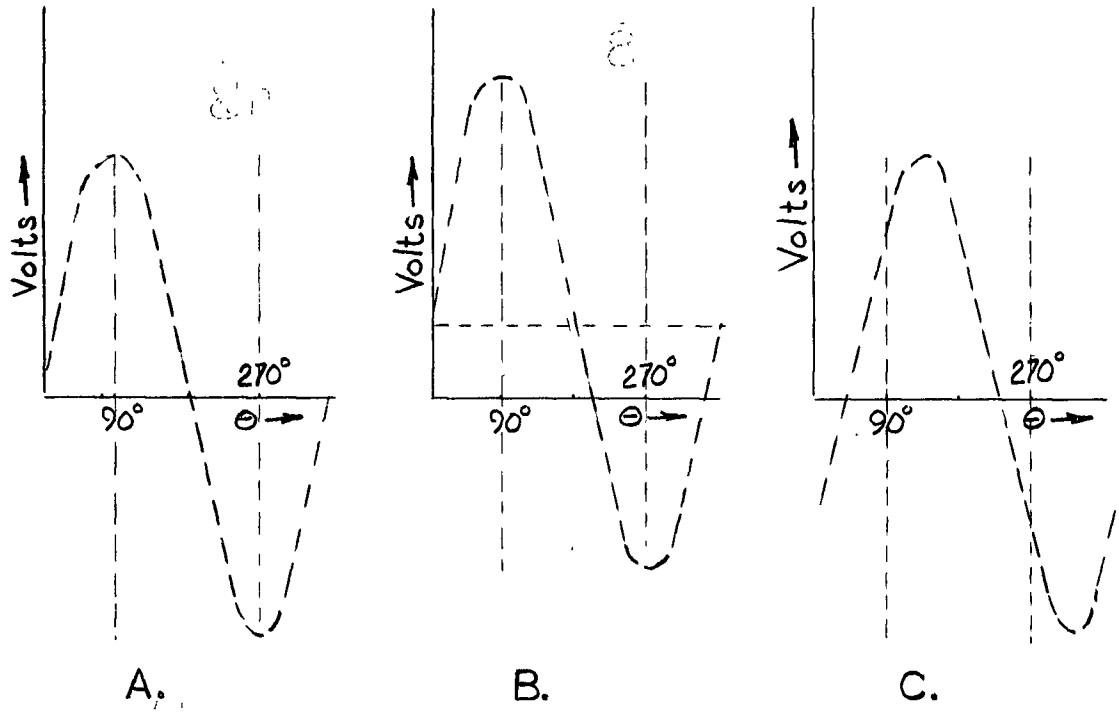

FIGURE 8. DEPENDENCE OF PROBE OUTPUT UPON ANGLE OF PROBE ROTATION

θ - Angle between axis of probe coil and the direction of current flow.

8A - Desired output.
8B - Output indicates spurious electrostatic signal.
8C - Output indicates spurious magnetic signal.

4.2 EXPERIMENTAL RESULTS (CONT'D.)

If there are any capacitative signals, these will not vary appreciably as the probe is rotated about its axis, and the base line will appear shifted as in figure 8B by an amount proportional to the capacitative signal.

4.2 EXPERIMENTAL RESULTS (CONT'D.)

If the probe leads are not tightly wound, then they will present a net area to the magnetic flux which is at some angle to the plane of the probe coil. Thus the resultant signal will be the sum of the voltages induced in the leads and in the coil. As the probe is rotated about its axis, this resultant signal will, in general, have maxima and minima which are shifted away from 90° and 270° as shown in figure 8C.

The magnetic probe was rejected unless the output varied in the manner shown in figure 8A.

A typical result from the analogue experiment is shown in figure 9. This result corresponds to a probe radius (ρ_p) of .45 cm, an inner conductor radius (r_i) of 2.6 cm, and an outer conductor radius of 9.1 cm (see also figure 5). The unperturbed magnetic field distribution is also included in figure 9. This curve is obtained by plotting the measured points of figure 9 on a $1/r$ - scale as shown in figure 10. The straight line section is then extrapolated to r_i and r_o and thus we obtain values of Bu(r) which are then transferred back to figure 9. The insert in figure 9 represents a plot of $\Delta B(r)$ - the difference of Bu(r) and Bp(r).

Note that the spatial resolution of the probe is limited by the diameter of the coil which is approximately 1 mm. However, $\Delta B(r)$ extends over a distance of approximately 10 mm., and it is, therefore, a real correction and not a property of the probe.

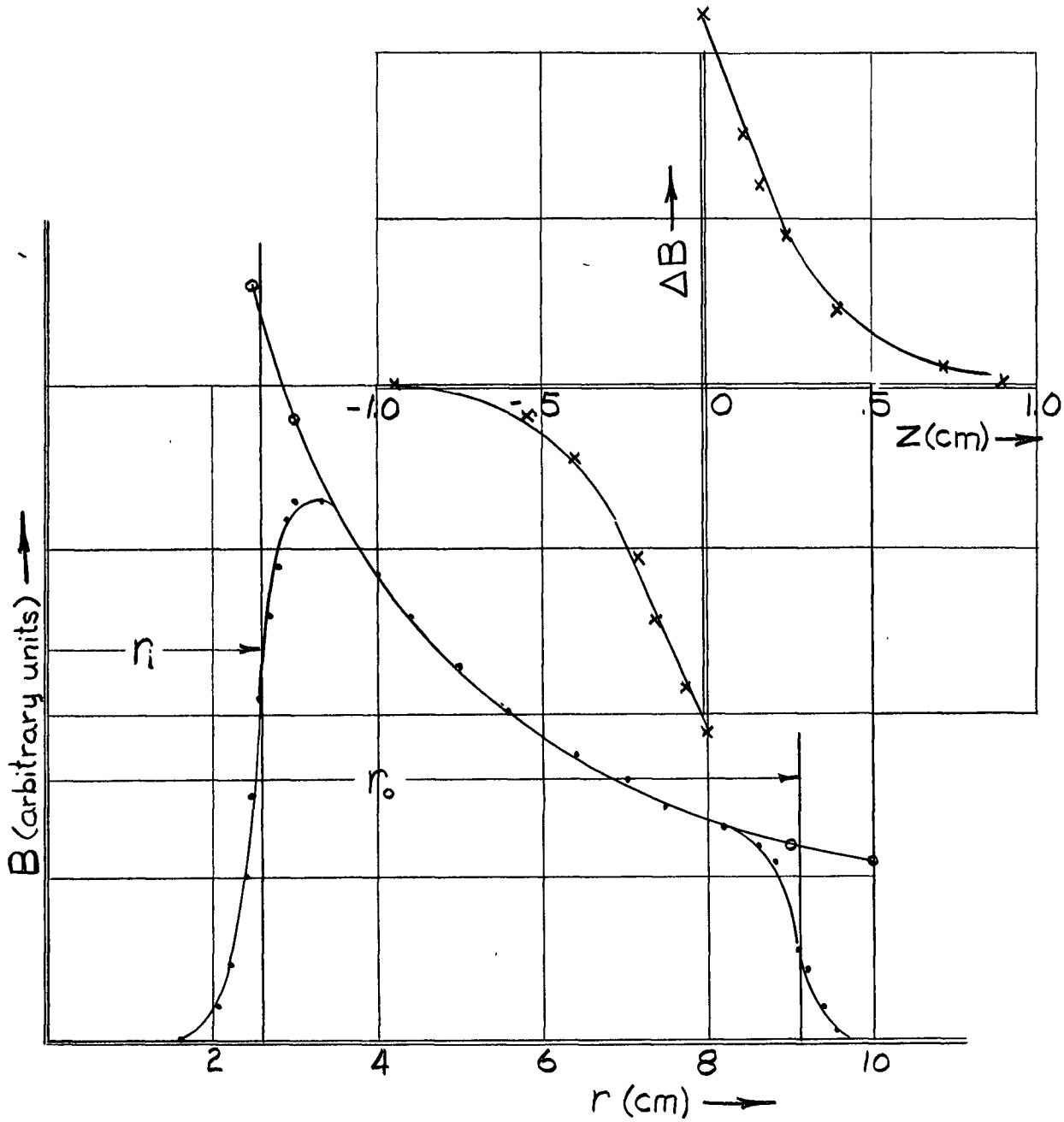

FIGURE 9. ANALOGUE EXPERIMENTAL RESULTS

r_i = Radius of inner current sheet
r_o = Radius of outer current sheet
z = Distance from inner current sheet
• Measured magnetic field
o True magnetic field (figure 10.)
x True magnetic field minus measured magnetic field.

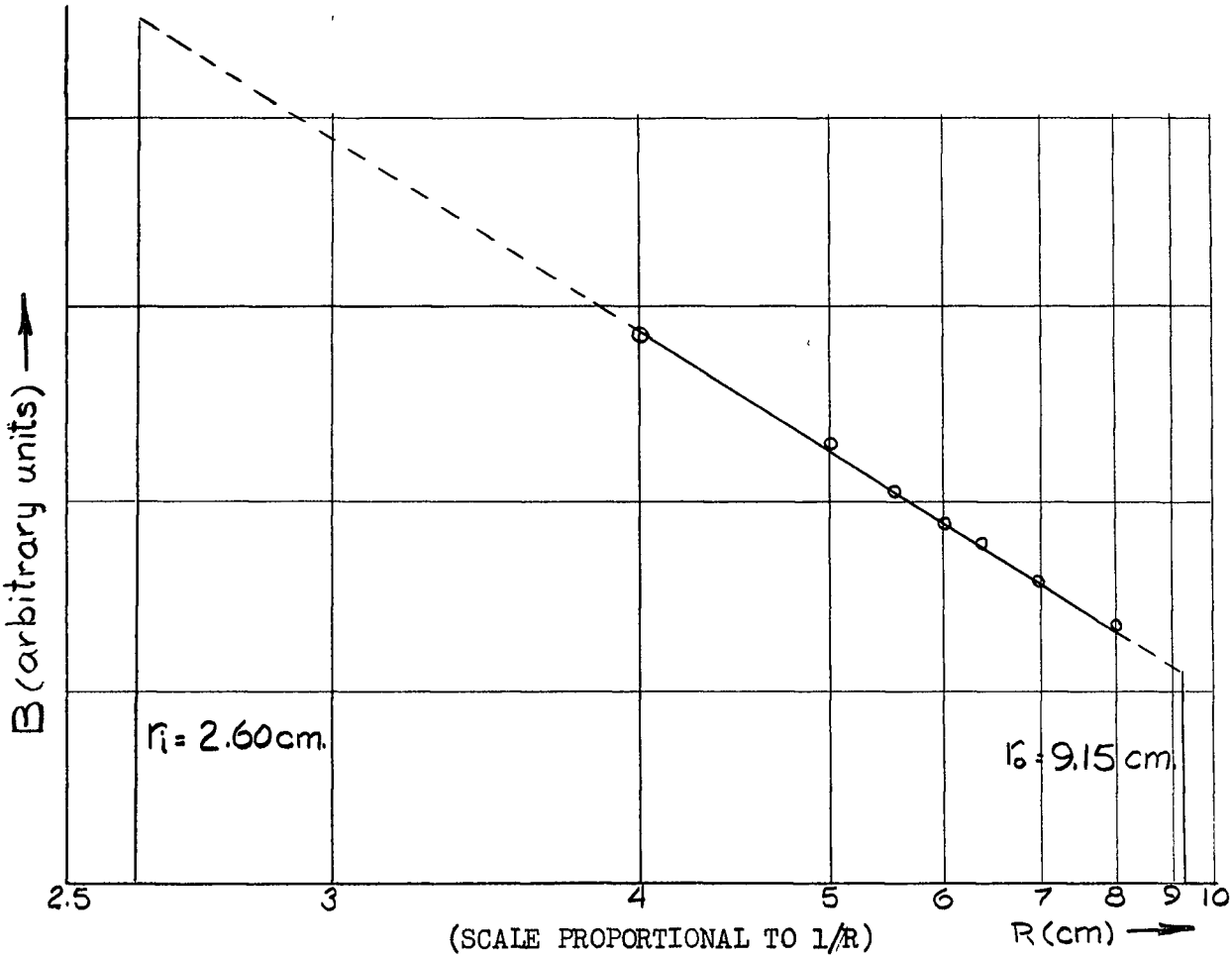

FIGURE 10. UNDERTURBED MAGNETIC FIELD

o Experimental points from figure 9.

— — Extrapolated magnetic field distribution.

4.2 EXPERIMENTAL RESULTS (CONT'D.)

The experiment is repeated for each of the inner conductors mentioned in section 4.1 and then the entire procedure is repeated for a probe radius of .35 cm. In order to examine the results of the analogue experiment more easily we define the field correction $\Delta B(z)$, where z is the distance of the field point from the position of the current sheet, i.e., $z = r - r_i$.

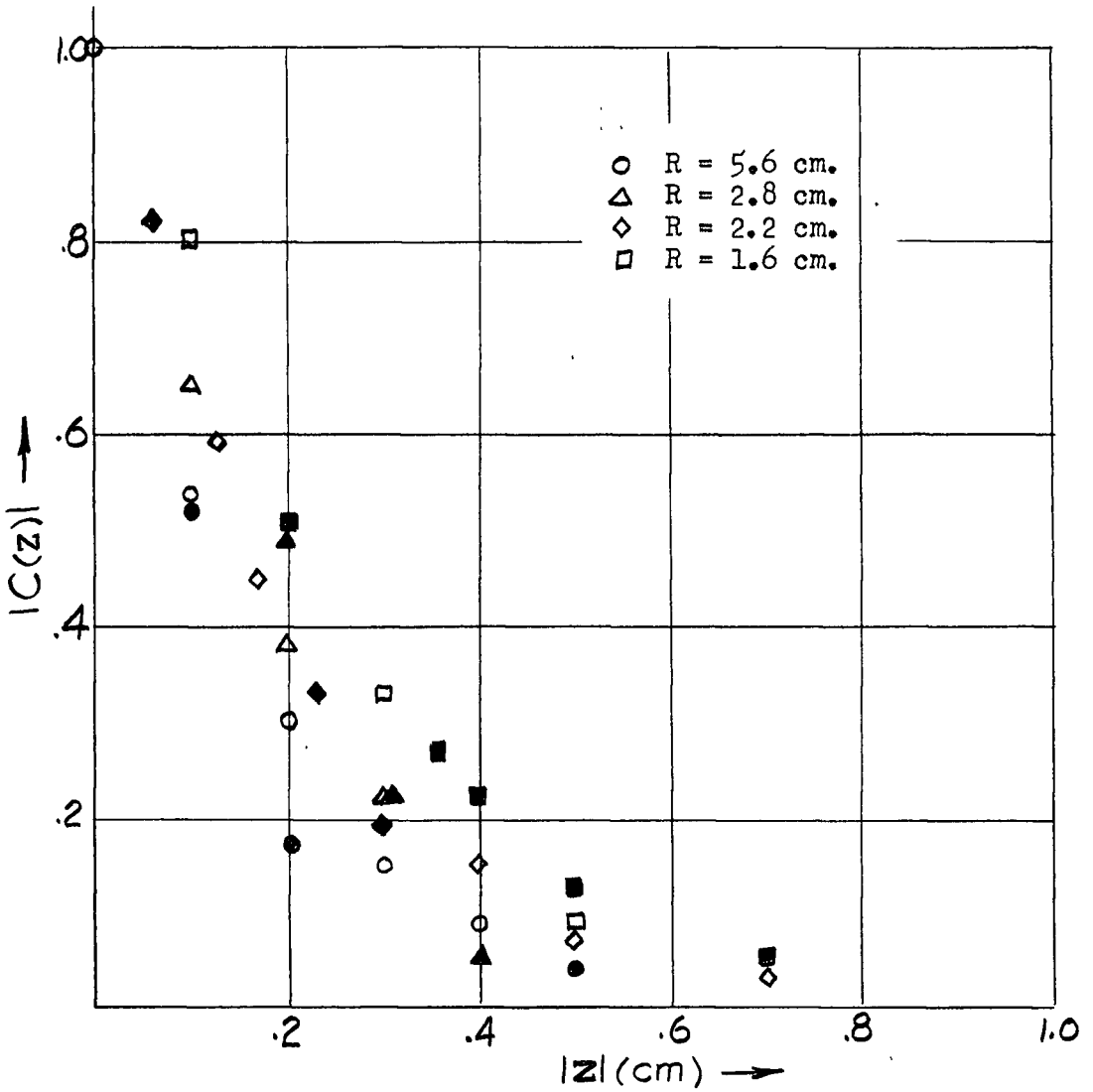

FIGURE 11. $|C(z)|$ vs $|z|$ (ρ_0 = .35 cm.)

○ △ ◇ □ correspond to positive values.
● ▲ ◆ ■ correspond to negative values.

4.2 EXPERIMENTAL RESULTS (CONT'D.)

Furthermore we let

$$B(z) = KC(z)$$

Where K is a constant of proportionality

and C(z) is a dimensionless correction

with the normalization C(0) = 1

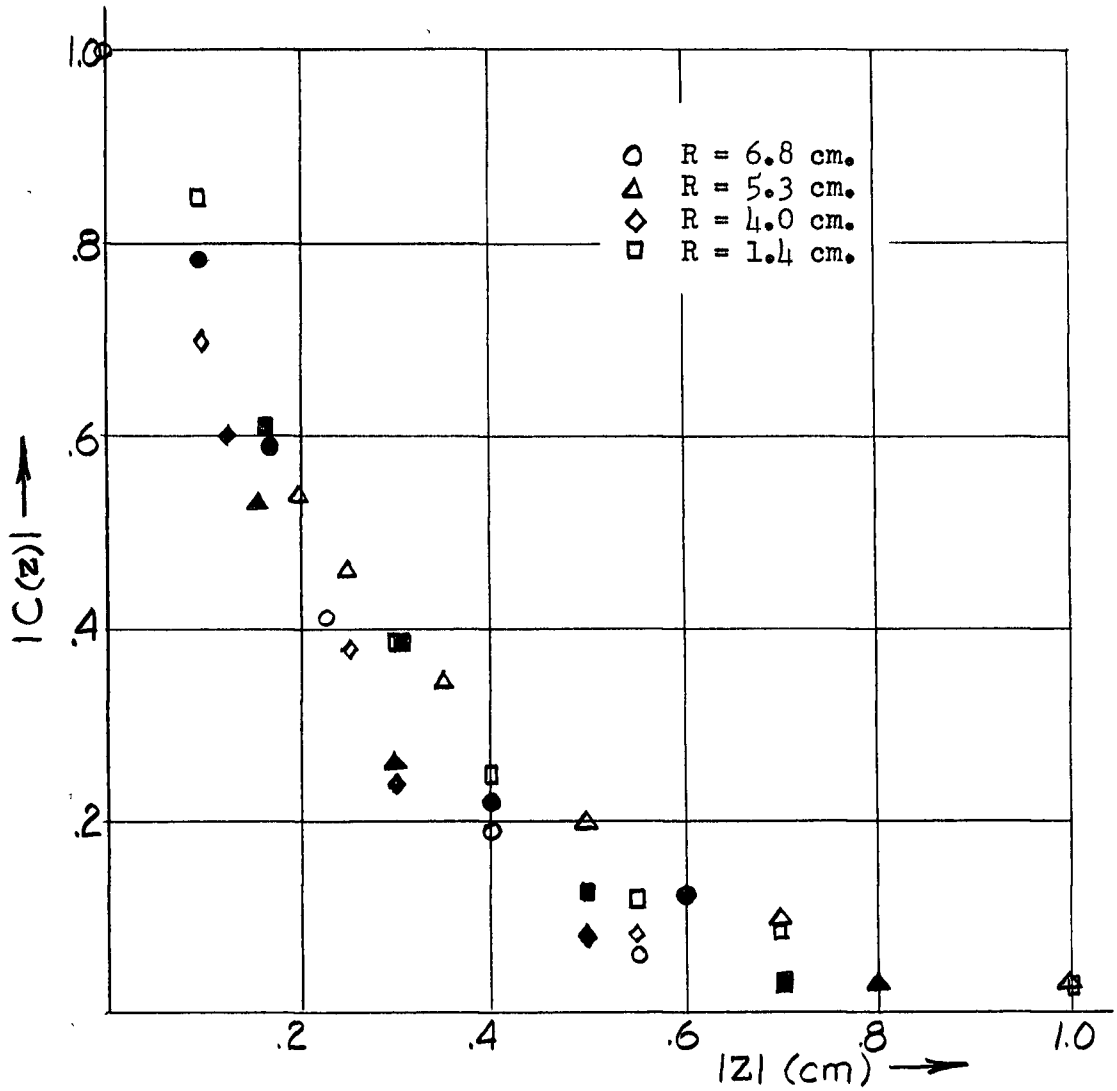

FIGURE 12. $|C(z)|$ VS $|Z|$ ($\rho_o = .45$ cm.)

○△◇□ correspond to positive values.
●▲◆■ correspond to negative values.

4.2 EXPERIMENTAL RESULTS (CONT'D.)

In figure 11 we plot the correction $|C(z)|$ versus $|z|$ for all measurements taken with a probe of radius .35 cm. Two points are to be noted. First, the points corresponding to positive and negative z do not differ for a given sheet radius i.e. the correction $C(z)$ appears to be anti-symmetric. Second, the points corresponding to current sheets of differing radius do not differ appreciably,

4.2 EXPERIMENTAL RESULTS (CONT'D.)

i.e. it is reasonable to assume that the correction $C(z)$ is independent of the radius of the current sheet. The second point is even more obvious in figure 12 where we have made the same plot, $|C(z)|$ vs. $|z|$, for the measurements taken with a .45 cm. radius probe.

4.3 THEORETICAL MODEL

The analogue experiment is designed to measure the magnetic field as a function of position along the axis of a non-conducting cylinder (the probe) placed diametrically through two coaxial, cylindric, current carrying sheets. It is a complicated mathematical problem to predict such a radially dependent magnetic field. In the present treatment we consider a simplified model which, it is hoped, will aid in the interpretation of the experimental results.

In the limit that r_o and r_i, the radii of the current carrying sheets, are large, the sheet in the vicinity of the probe hole is approximately plane. A solution for this problem has been obtained by Malmberg (1964).

$$B = B_o \left(1 + \frac{z/\rho_o}{\pi (1 + z^2/\rho_o^2)} - \frac{1}{\pi} \cot^{-1}(z/\rho_o) \right)$$

where B is the perturbed magnetic field

B_o is the unperturbed magnetic field

ρ_o is the probe radius.

4.3 THEORETICAL MODEL (CONT'D.)

In our previous notation (see page 25) we have written:

$$Bu(r) - Bp(r) = \Delta B(Z)$$

where $Bu(r)$ is the unperturbed magnetic field

$Bp(r)$ is the perturbed magnetic field

$\Delta B(z)$ is the field correction

$Z = r - x$ is the distance between the field point r and the current sheet at x.

Furthermore,

$$\Delta B(Z) = KC(Z)$$

Thus we now have:

$$K = B_o = \frac{\mu_o \tau J_o}{2}$$

where

μ_o is the permeability

τ is the thickness of the current sheet

J_o is the current density in the sheet

and,

$$C(z) = \frac{2}{\pi}\left(\frac{Z/\rho_o}{(1 + Z^2/\rho_o^2)} - \cot^{-1}\frac{Z}{\rho_o} \right)$$

As the current distribution in the sheet is perturbed appreciably over a distance of only a few times the probe radius, then there is a contribution to the correction from a correspondingly small area of the current distribution. In our analogue experiment the current sheet is approximately planar over this small area and hence even this simple model gives reasonable

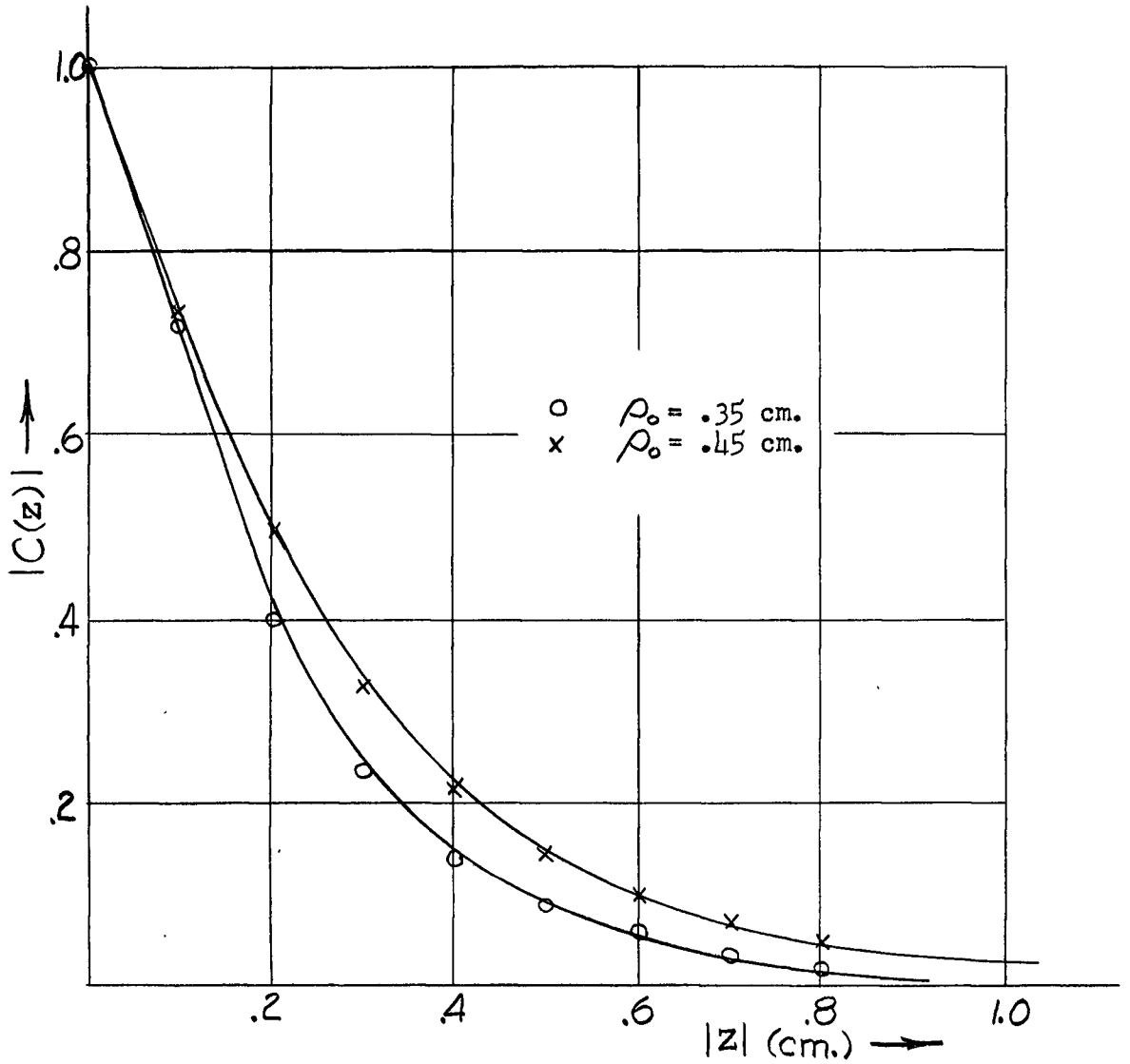

FIGURE 13. $|C(z)|$ vs $|z|$ (THEORETICAL CURVES)

4.3 THEORETICAL MODEL (CONT'D.)

predictions. The correction $C(z)$ is plotted against z in figure 13 for the two cases of interest - $\rho_o = .35$ cm. and, $\rho_o = .45$ cm.

4.4 CONCLUSIONS

Consider the procedure which we will be following in the next sections. We will have a measured magnetic field which we will wish to correct in order to calculate the associated true current density distribution. However, we must correct the magnetic field by an amount which is itself a function of the "true" current density distribution. Mathematically, this problem is more easily set up if we have an analytic expression for the correction. Thus we compare our experimental points of section 4.2 with the theoretically predicted curves of section 4.3. The agreement is excellent for both the case of $\rho_o = .35$ cm. (figure 14) and $\rho_o = .45$ cm. (figure 15).

For comparison, we have also included in figure 14 the experimental points which are obtained from a measurement of the magnetic field outside the return conductor of the actual z-pinch discharge vessel. This apparatus is described in a later section of the thesis (section 7.0), but it is sufficient to state here that the return conductor is a thin, fine-meshed, brass screen with a hole of approximately .35 cm. for the probe. These points are obtained when the plasma is away from the wall of the discharge vessel (500μHg argon; 4.5μsec) and hence we expect the error in the magnetic field to be associated with the return conductor alone. These points also agree with the theoretical prediction.

It is observed that the correction is a function of the radius of the probe hole. In section 3.2 we have included conductivity error in our discussion with the introduction of an effective probe

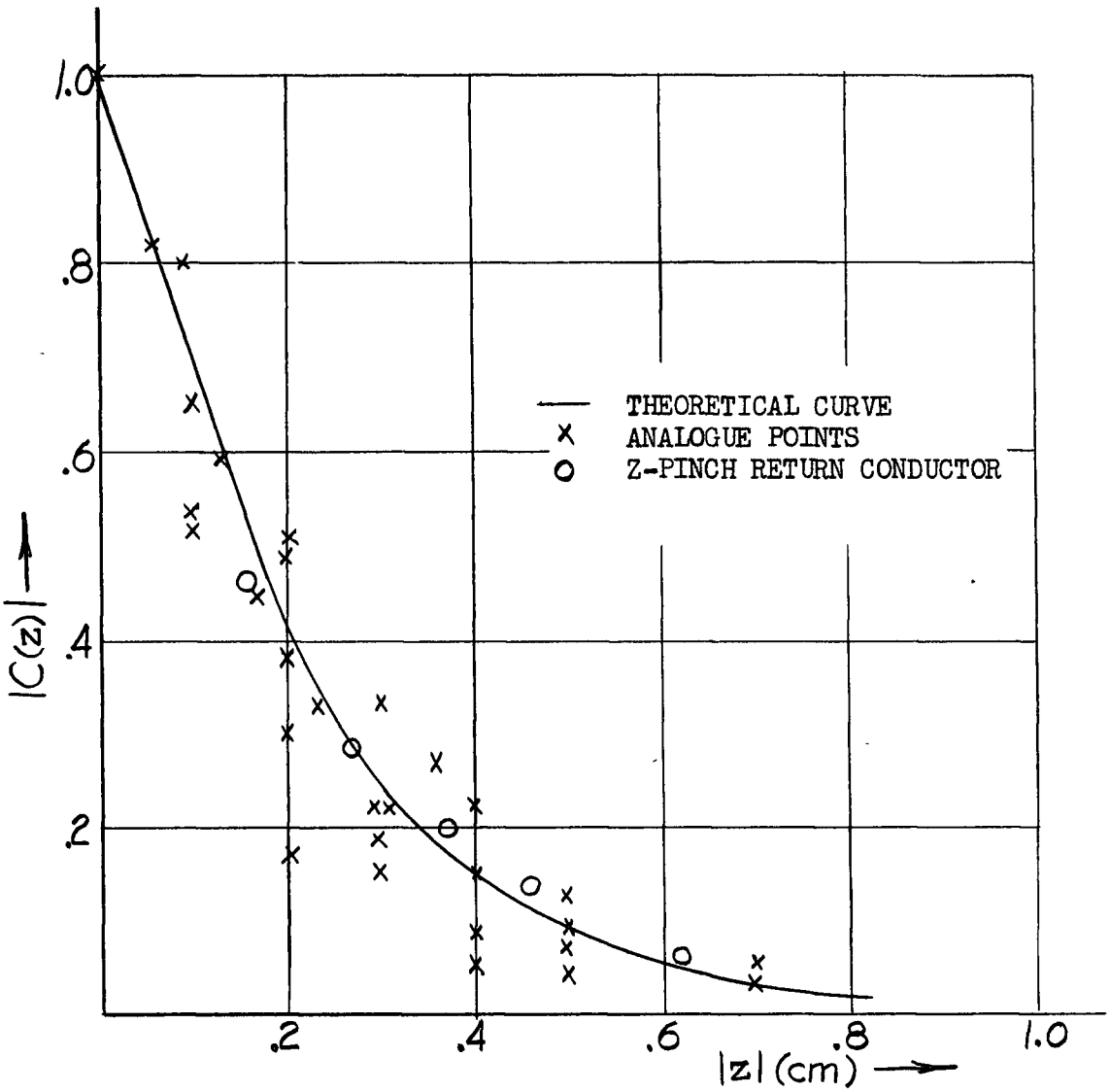

FIGURE 14. $|C(z)|$ vs. $|z|$ ($\rho_o = .35$ cm.)

4.4 CONCLUSIONS (CONT'D.)

radius. Work of Dippel (1959) suggested that the exact value of the effective radius was not critical. Similarly, in figure 13, where we have plotted the curves of $\rho_o = .35$ cm., and, $\rho_o = .45$ cm., we observe that a 25% change in ρ_o results in less than 10% change in field correction over that region where the correction is appreciable.

We conclude that an investigation of boundary error allows for a correction of the greatest perturbations caused by the immersion of

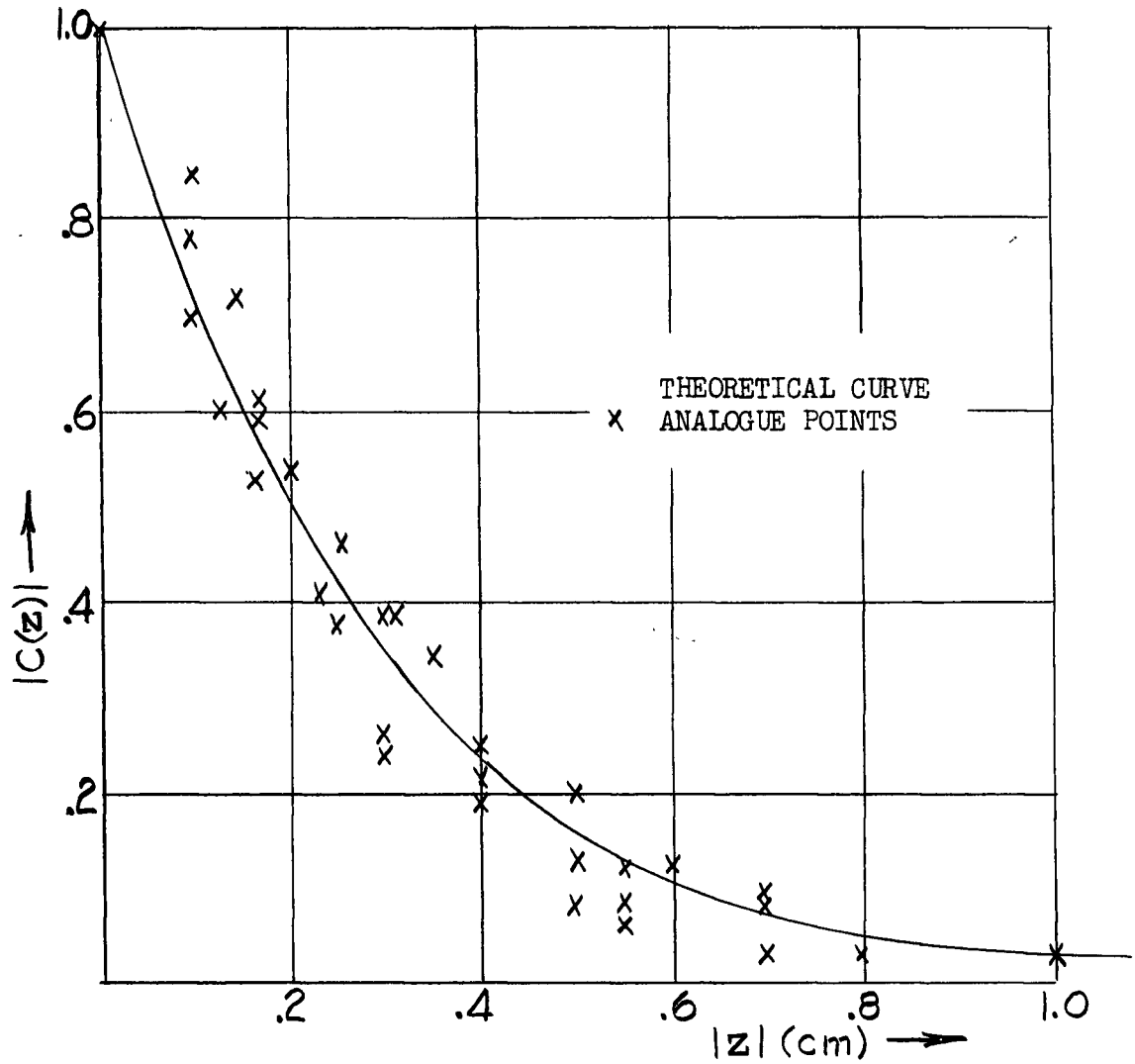

FIGURE 15. $|C(z)|$ vs. $|z|$ ($\rho_c = .45$ cm.)

4.4 CONCLUSIONS (CONT'D.)

the probe in the plasma. We conclude that the analytic expression derived by Malmberg (1964) is a reasonable approximation to the correction.

5.0 MAGNETIC FIELD CORRECTION

In this section we consider the correction of that magnetic field which is obtained from measurement on the z-pinch discharge. The apparatus and the experimental procedure will be explained in later sections (sections 7 and 8, respectively), but in this section we simply assume the measured, or perturbed, magnetic field (B_p) is known.

Under experimental conditions the current density distribution is unknown and yet the field correction (ΔB) is a function of current density (see section 4.3). The correction procedure is performed in the following way.

Assume that we know the unperturbed field B_u, then we can obtain the "true" current density from a solution of Maxwell's equation:

$$\nabla \times \underline{B} = \mu_o \underline{J}$$

Using the cylindrical geometry of the z-pinch discharge and the fact that we have only an azimuthal magnetic field, we have:

$$J(r) = \frac{1}{\mu_o r} \frac{\partial}{\partial r} (rB(r))$$

where r is measured from the axis of the discharge vessel.

We must now determine the field correction $\Delta B(r)$. For this discussion, we use the variable "r" for the field point and the variable "x" for the source point, i.e. the position of an element of current density. The current density is thus $J(x)$. In this notation, the field correction $\Delta B(z)$, of the analogue experiment becomes $\Delta B(r-x)$ since z, the distance from field to source point, is given by $(r-x)$.

5.0 MAGNETIC FIELD CORRECTION (CONT'D.)

If we have a single current sheet of radius x_o, then from section 4.4:

$$B(r-x_o) = \frac{\mu_o \gamma J(x_o)}{\pi}\left(\frac{(r-x_o)/\rho_o}{(1+(r-x_o)^2/\rho_o^2)} - \cot^{-1}\frac{(r-x_o)}{\rho_o}\right)$$

However, if we have a current distribution J(x), then the total correction factor ($\Delta B(r)$) must be calculated as the integral over all elements of the current distribution.

$$\Delta B(r) = \int_o^R \Delta B(r-x)dx = \frac{\mu_o}{2}\int_o^R J(x)\, C(r-x)dx$$

where $$C(r-x) = \frac{2}{\pi}\left(\frac{(r-x)/\rho_o}{(1+(r-x)^2/\rho_o^2)} - \cot^{-1}\frac{(r-x)}{\rho_o}\right)$$

and where R is the inner radius of the discharge vessel.

Finally we must add this field correction to the measured magnetic field to get the unperturbed field.

$$Bu(r) = Bp(r) + \Delta B(r).$$

Thus the equation which must be solved for Bu(r) is:

$$Bu(r) = Bp(r) + \frac{1}{2}\int_o^R \frac{C(r-x)}{x}\frac{d}{dx}\left[x\, Bu(x)\right]dx$$

where Bp(r) and C(r-x) are known functions.

We may also set up the problem to obtain an equation for the current density directly.

$$\Delta B(r) = \frac{\mu_o}{2}\int_o^R J(x)\, C(r-x)dx$$

and, $$Bu(r) = \frac{\mu_o}{r}\int_o^r x\, J(x)\, dx$$

5.0 MAGNETIC FIELD CORRECTION (CONT'D.)

Thus,

$$\frac{\mu_o}{r}\int_o^r x\,J(x)\,dx = Bp(r) + \frac{\mu_o}{2}\int_o^R J(x)\,C(r-x)\,dx$$

We must solve this equation for $J(x)$ in terms of the known functions $Bp(r)$ and $C(r-x)$.

As we do not, in fact, have an analytic expression for the measured field Bp, but rather a set of measurements taken at given radial positions, then a numerical solution becomes necessary.

5.1 NUMERICAL COMPUTATION

In the previous section we have developed two equations which must now be solved.

1. $$\frac{\mu_o}{r}\int_o^r x\,J(x)\,dx = Bp(r) + \frac{\mu_o}{2}\int_o^R J(x)\,C(r-x)\,dx$$

2. $$Bu(r) = Bp(r) + \frac{1}{2}\int_o^R \frac{C(r-x)}{x}\,\frac{d}{dx}\,(xBu(x))\,dx$$

In order to solve the first equation for $J(x)$ we consider the following approximation. We construct a set of concentric current carrying sheets, each of thickness Υ = 1 mm., to replace the continuous current distribution of the z-pinch. The magnitude of the current density in each sheet is determined by its radial position as is shown in figure 16.

At the same time, we replace the mathematical integration over the current distribution by a summation over the constructed

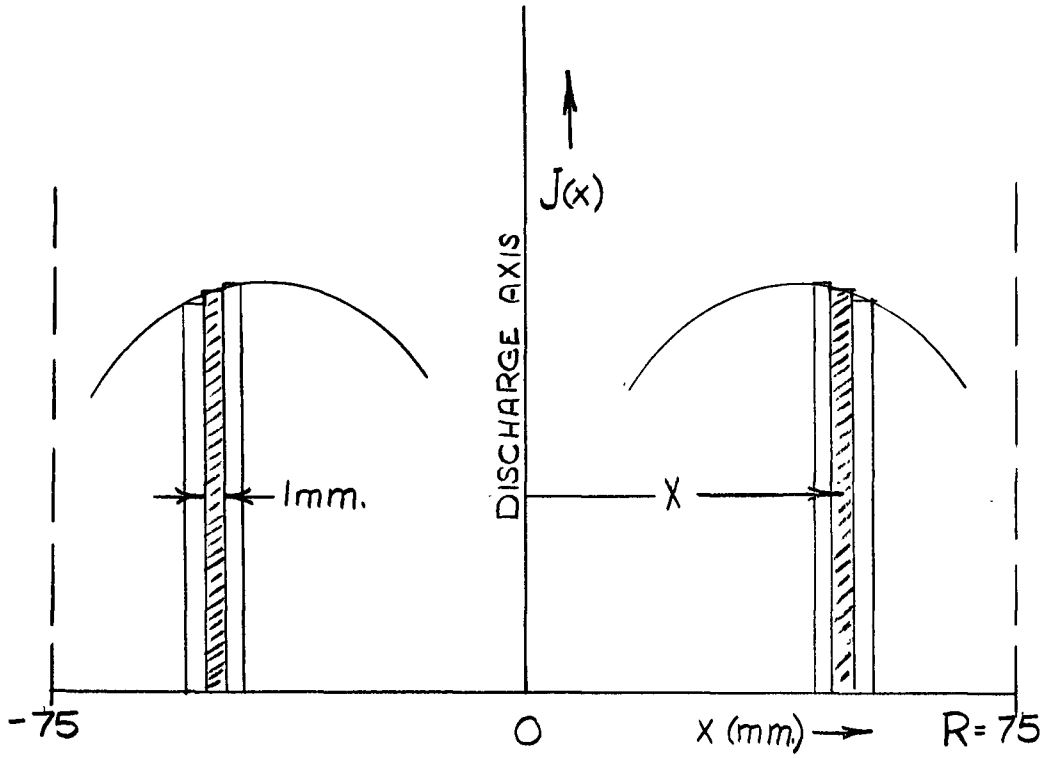

FIGURE 16. SHEET APPROXIMATION TO CONTINUOUS CURRENT DENSITY DISTRIBUTION

5.1 NUMERICAL COMPUTATION (CONT'D.)

sheets. If we have one current sheet at $x = x_o$, then from the analogue experiment (section 4.3) we have:

$$\Delta B(r-x_o) = \frac{\mu_o \gamma J(x_o)}{2} C(r-x_o)$$

But if we have a number of current sheets, we have:

$$B(r) = \sum_{x=0}^{R} \frac{\mu_o \gamma}{2} J(x)\, C(r-x)$$

Similarly,

$$Bu(r) = \frac{\mu_o}{r} \int_0^r x\, J(x)\, dx$$

becomes,

$$Bu(r) = \frac{\mu_o \gamma}{r} \sum_{x=0}^{r} x\, J(x)$$

Thus, we may write equation 1. as:

$$\frac{\mu_o \Upsilon}{r} \sum_{x=0}^{r} x\, J(x) = Bp(r) + \frac{\mu_o \Upsilon}{2} \sum_{x=0}^{R} C(r-x)\, J(x)$$

Now the interval (Υ) is 1 mm. and we have values of Bp(r) from r=0 to r=80 mm. C(r-x) is also known for 1 mm. intervals from section 4.3. Hence there are 80 equations (one for each r) of the form just shown which must be solved simultaneously for the eighty values of J(x).

To simplify the mathematical procedure these equations are written in matrix notation and the problem is then solved on a computer.

In matrix notation, the equation becomes:

$$\mu_o \Upsilon\, Srx\, Jx = (Bp)_r + \frac{\mu_o \Upsilon}{2}\, Crx\, Jx$$

where Jx is an 80 - component vector

Srx is an 80 x 80 matrix of the form:

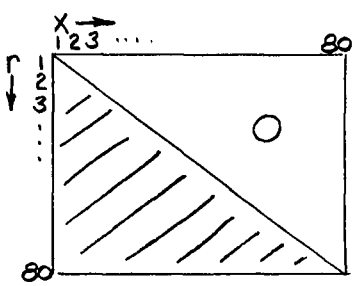

with individual elements (Srx) given by:

$$(Srx) = \frac{x}{r} \qquad \text{if} \quad x \leq r$$

$$(Srx) = 0 \qquad \text{if} \quad x > r$$

and, Crx is an 80 x 80 matrix of the form

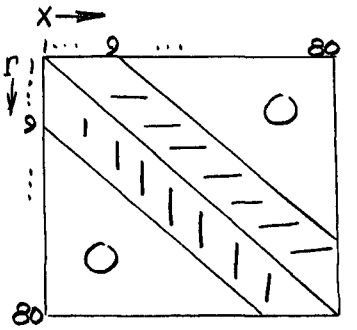

with individual elements (Crx) given by:

$$(Crx) = \frac{2}{\pi}\left(\frac{(r-x)/\rho_o}{(1 + (r-x)^2/\rho_o^2)} - \cot^{-1} \frac{(r-x)}{\rho_o} \right)$$

Since the magnitude of (Crx) falls to 1% at (r-x) = 9 mm., we consider only 9 sub-diagonals above and below the main diagonal in the matrix representation of Crx. The remainder of the matrix is zero.

The solution of equation 1. is:

$$Jx = \frac{1}{\mu_o \tau} (Srx - \frac{1}{2} Crx)^{-1} (Bp)r$$

i.e. we must invert an eighty by eighty matrix.

Similarly, we can solve equation 2. (page 38). In matrix notation this equation becomes:

$$(Bu)r = (Bp)r + \frac{1}{2} Crx\ Dxx'\ (Bu)x'$$

5.1 NUMERICAL COMPUTATION (CONT'D.)

where Dxx' is an eighty by eighty matrix of the form:

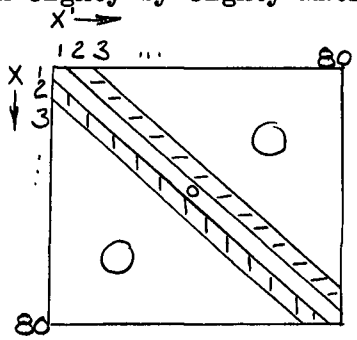

with the individual elements (Dxx') given by:

$$(Dxx') = \frac{(x' + 1)}{2x'} \delta (x-x'+1) - \frac{(x' - 1)}{2x'} \delta (x-x'-1)$$

where $\delta (x-x'+1) = 1$ if $(x-x'-1) = 0$

$\delta (x-x'+1) = 0$ if $(x-x'-1) \neq 0$

The solution of this equation is given formally by:

$$(Bu)_{x'} = (Irx' - \frac{1}{2} Crx\ Dxx)^{-1} (Bp)r$$

where Irx' is the identity matrix.

From equation 1. we solve directly for the current density Jx and from this we solve for the unperturbed magnetic field (Bu)r from:

$$(Bu)r = \mu_o \gamma\ Srx\ Jx$$

However, in equation 2. we solve directly for the unperturbed magnetic field $(Bu)_r$ and then solve for the current density Jx from:

$$Jx = \frac{1}{\mu_o \gamma} Dxx' (Bu)x'$$

We program the computer for both of these solutions and then compare the results (see section 8.3).

In the remaining portion of this section we discuss several points which arise in programming the construction of the matrix Crx.

In order to calculate any element of the matrix Crx we must have a value for the effective probe radius ρ_0. We had introduced the concept of effective probe radius in section 3.2 in order to consider so called "conductivity error". Later, in section 4.4 we found that the correction factor was insensitive to the precise value of ρ_0. The plasma in the vicinity of the probe was photographed (section 9.3) but there was no observed change in luminosity in this region which could be used as an estimate of ρ_0. Thus for our "first order" correction we use the radius of the quartz guide tube which is .37 cm.

In order to minimize the error introduced by replacing the continuous functions by discrete numerical values, we arrange the x - coordinates (the coordinates of the current density values) to coincide with the half-integers of the r - coordinates (the coordinates of the corresponding magnetic field values). The effect can best be seen in a diagram. In figure 17 we consider the correction factor due to a current sheet of thickness 1 mm. which is centered at x. In figure 17B where we have x and r coincident, i.e. obtain field values at the mid point of the current sheet, then we

have a much larger error in the numerical approximation to the correction factor than in the case with x and r values staggered.

One further consideration must be examined closely and this is the choice of Crx for the region of $x \rightarrow 0$. The correction factor must be modified for those current sheets which are within the characteristic distance of the correction factor (9 mm.) from the axis of the discharge vessel. The modification is obtained by assuming the current distribution is rotationally symmetric and then calculating the correction factor as the algebraic sum of the two over lapping correction factors as is shown in figure 18. To obtain the complete correction factor we assume that the area under the correction as a function of radius is the same both inside and outside the current sheet. The results of the analogue experiment (section 4.2) indicate that this assumption is reasonable. Thus the correction factor outside the current sheet is normalized by the area under the curve, rather than the normalization $C(0) = 1$. (See figure 18).

Once the individual matrices Crx and, either Srx or Dxx' (depending upon the method of solution), have been constructed, the problem is solved by the inversion of a matrix which is a combination of these matrices. Difficulties are encountered in this procedure because the determinant is very small. This determinant has 80 x 80 elements and the magnitude of each element is less than one.

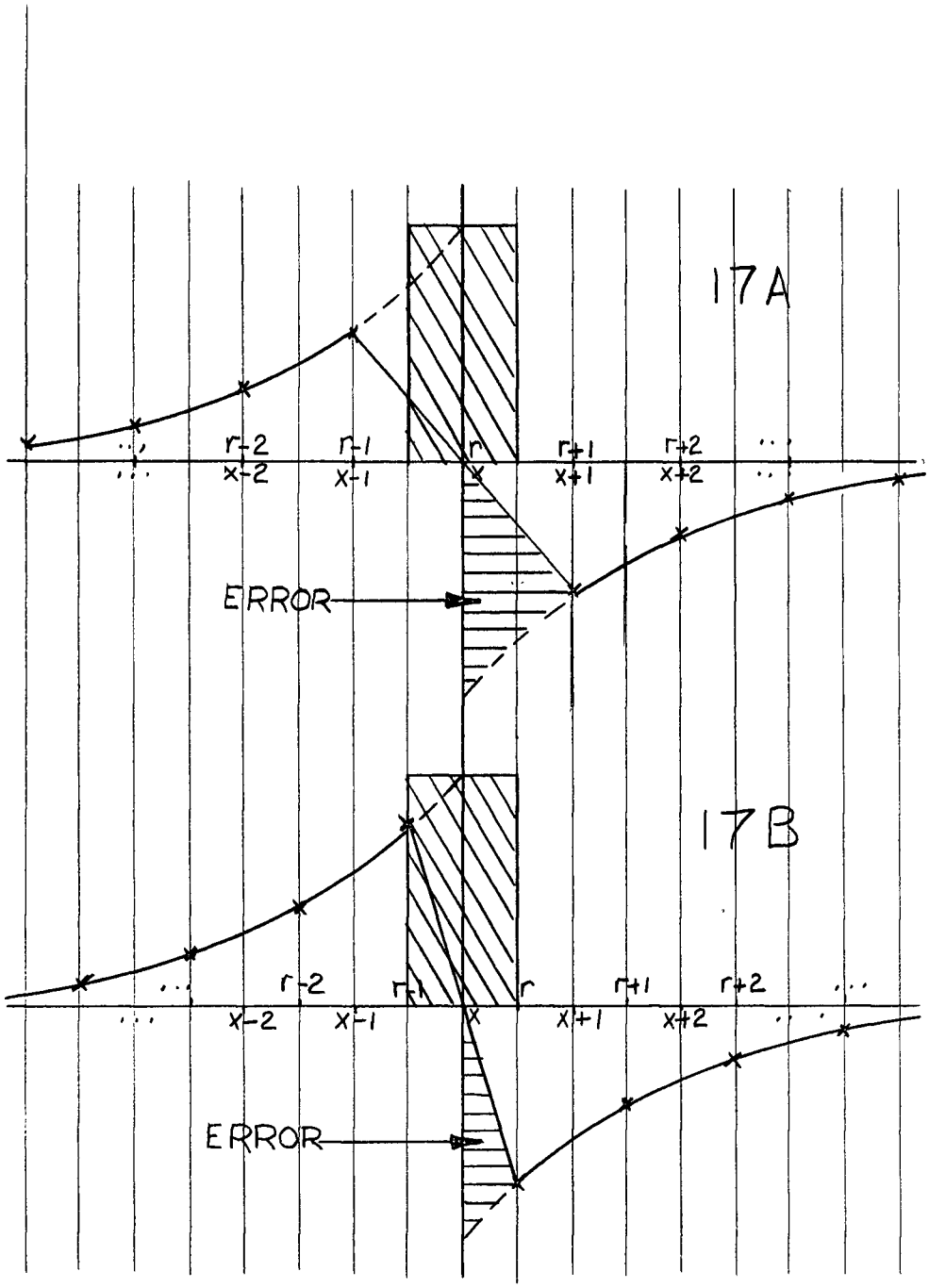

FIGURE 17. ERROR IN NUMERICAL APPROXIMATION TO CORRECTION

17 A r coincides with x
17 B r coincides with x + 1/2

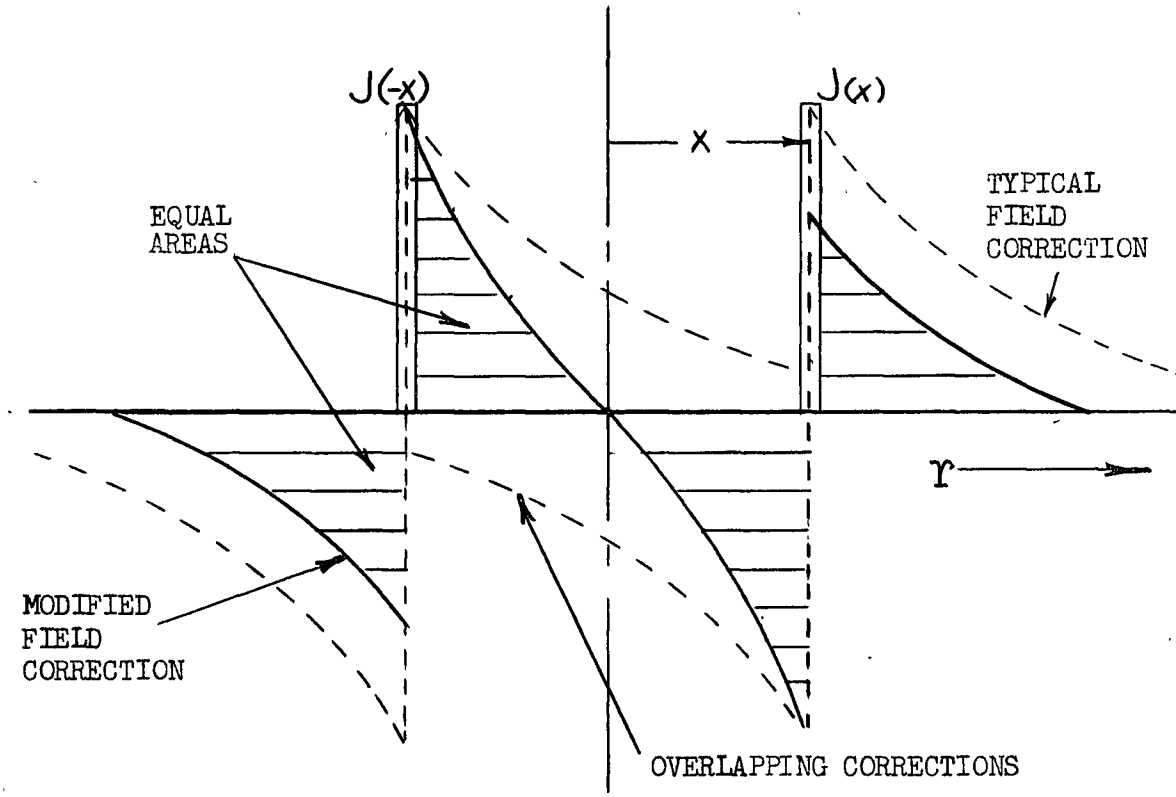

FIGURE 18. MODIFICATION OF CORRECTION NEAR AXIS

5.1 NUMERICAL COMPUTATION (CONT'D.)

The problem is solved simply by multiplying all matrix elements by 2. The resultant determinant is then of the order of 10^{-14} and this lies well within the range of the computer (10^{-38}). The final results must then all be multiplied by 2 (since it is the inverse).

A second difficulty associated with the large size of the matrices is the problem of accumulation of computer "round-off" error. This accumulation arises from the many operations involved in the inversion of an 80 x 80 matrix. The results of the program are greatly improved when the inversion is performed with variables defined in double precision. (For details of the Fortran computer program see Appendix II.)

5.1 NUMERICAL COMPUTATION (CONT'D.)

It should be pointed out that matrix inversion is not the only method of solution. Indeed, the form of equation 1. and 2., suggests the use of an iterative type procedure. Two iterative methods of solution were attempted, but in both cases spurious, negative "spikes" occurred in the current density distribution which prevented the iterations from converging. These negative spikes could be eliminated through a modification of the computer program. However, as negative current densities have been observed at the walls of the discharge vessel by Komelkov (1958), this somewhat artificial elimination in the program is most undesireable. There appeared to be no other way to get the program to converge to a solution and these methods were abandoned.

5.2 TEST FOR NUMERICAL PROGRAM

We will postpone a detailed discussion of the possible errors in applying the results of the analogue experiment to the z-pinch measurements until section 8.4. By then, we will have calculated the true magnetic field and current density distributions of the z-pinch discharge. However, we do wish to test the numerical program of the preceding section.

Fortunately, the magnetic field measurements of the analogue experiment (see figure 9.) provide an excellent test for the program. We can calculate the current distribution from the measured magnetic field using our program and then compare this result with the known distribution (essentially a δ - function).

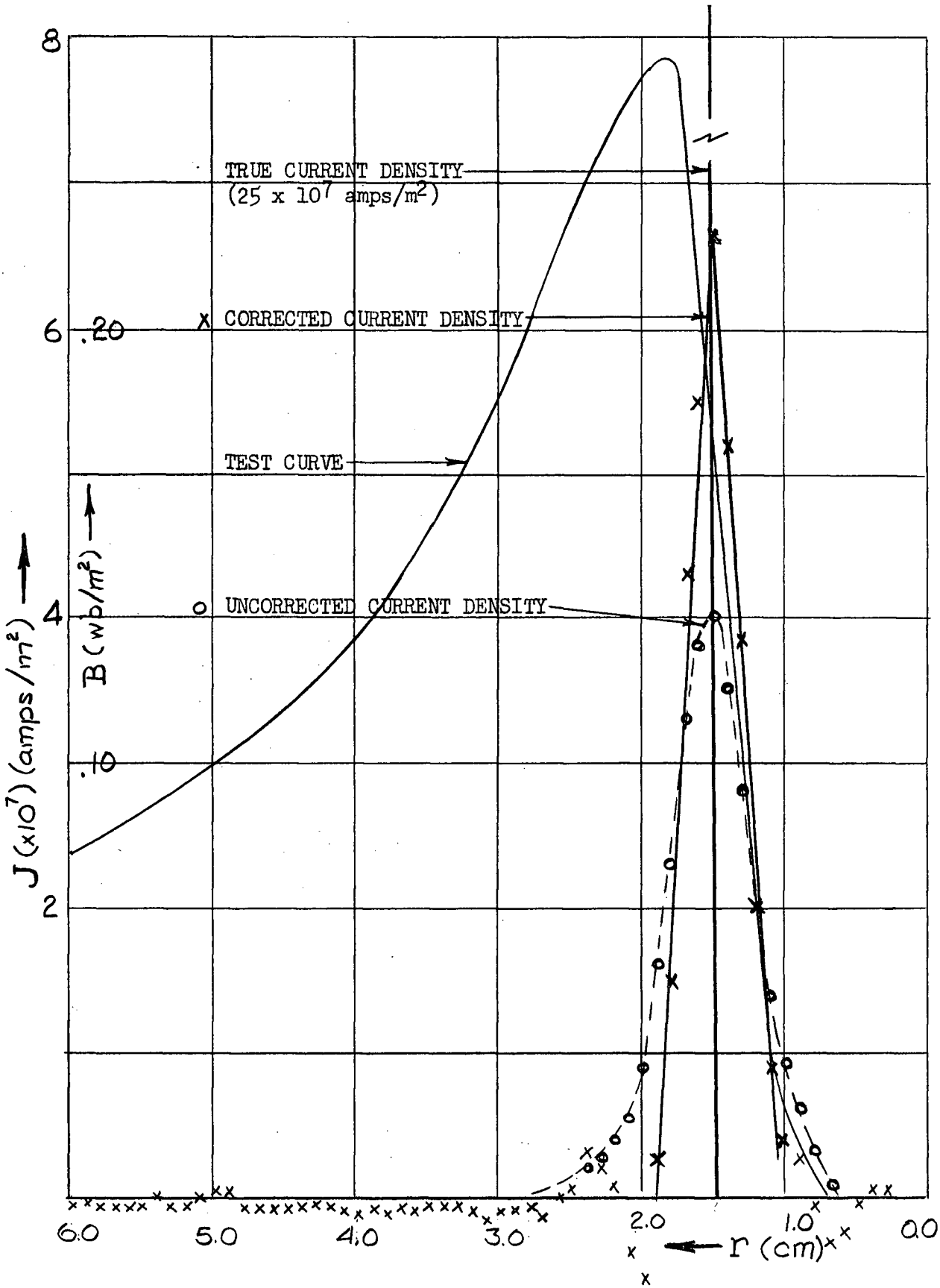

FIGURE 19. ANALOGUE TEST CURVE

5.2 TEST FOR NUMERICAL PROGRAM (CONT'D.)

The result of the correction procedure may be observed in figure 19., where we have plotted the uncorrected, corrected, and true current densities. It is apparent that the corrected current density is an improvement over the uncorrected current density, but it still falls well below the true current density which is known from the analogue experiment. A discussion of these results follows.

The correction applied to the measured curve is greatest at a point of discontinuity in the current distribution. This can be seen from the diagram of figure 20. At a point of approximately constant current density, the individual corrections cancel when the total field correction is calculated. However, at a point of discontinuity this cancellation does not occur and $\Delta B(r)$ is considerable. Although the correction is therefore greatest at a point of discontinuity, the numerical calculation is poorest at such a position because of the finite interval (here 1 mm.) which is used in the numerical approximation. This effect has already been examined in figure 17. As a result, the corrected current density curve has still only one quarter of the true magnitude, but the improvement over the uncorrected current density curve - increases peak current by 50% and reduces half width by 40% (see figure 19.) - is sufficient to give an appreciable change in the experimentally measured current density distribution. This change will be discussed in a later section (section 8.4).

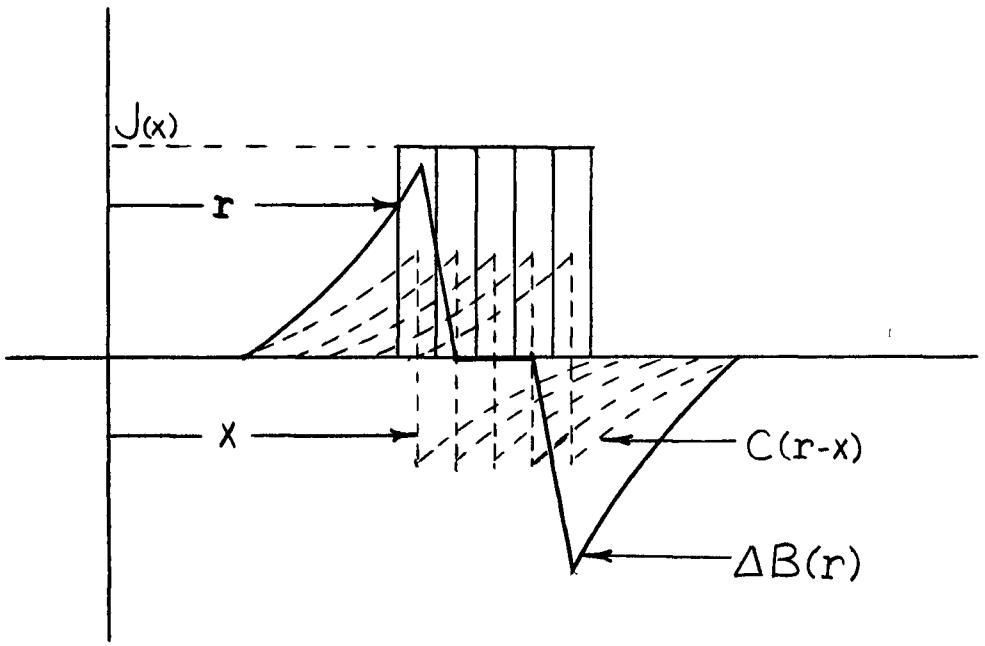

FIGURE 20. TOTAL FIELD CORRECTION

5.2 TEST FOR NUMERICAL PROGRAM (CONT'D.)

The important conclusion is the following. From these results it is apparent that any indication of a "spike" in the current density distribution represents a lower limit to the peak in the true current density.

PART II

EXPERIMENTAL RESULTS

6.0 INTRODUCTION

This investigation has been designed to study the plasma dynamics of the z-pinch discharge. In this Part we present the observations which will be compared with predictions based upon certain physical models of the plasma in Part III.

The most important result is the measurement of the current density distribution which has been corrected for the probe error as described in Part I.

However, it is desireable to have an independent method of investigation which we can use to assist in the interpretation of our magnetic probe results. As the plasma is highly luminous, and as photographic techniques have been described previously in the literature, for example Curzon(1962) and Folkierski (1963), we use these techniques to obtain results which can be compared with our current density measurements. The photographic measurements are discussed in section 9 and the comparison of photographic and magnetic probe results is given in section 10.

Thus Part II of the thesis contains a description of the experimental apparatus and continues with a presentation and discussion of all experimental results. The presentation of results is divided according to the diagnostic technique which has been used to obtain the results - magnetic probes in section 8 and the framing camera in section 9.

7.0 APPARATUS

A photograph of the apparatus is shown in figure 21. and a schematic diagram of the discharge circuit and triggering circuitry is shown in figure 22. The essential features of all components of this apparatus are given in tabular form (see Table I at end of this section). Brief descriptions are given for the three main components - the discharge vessel, the capacitor bank, and the triggering circuit. We also include a description of the framing camera which is used in the photographic studies.

Discharge Vessel:

The discharge vessel is a large Pyrex tube (17 cm. O.D., 15 cm. I.D., and 70 cm. in length) which is sealed with plane brass electrodes at each end. The vessel may be evacuated and then filled to the required pressure with the desired gas (argon for these investigations). An electric current is discharged through this gas which thus forms the plasma.

The discharge vessel is designed for use with both photographic and magnetic probe diagnostics. To allow for photographic observation perpendicular to the axis of the discharge, a fine mesh brass screen is used as the return conductor of the discharge circuit (refer to figure 21.and figure 22.). Furthermore, one of the end electrodes is perforated and it is provided with a large glass window which allows "end-on" photography, i.e. photography along the axis of the discharge vessel. (The discharge vessel is evacuated and filled through the second electrode.) To allow access to the plasma

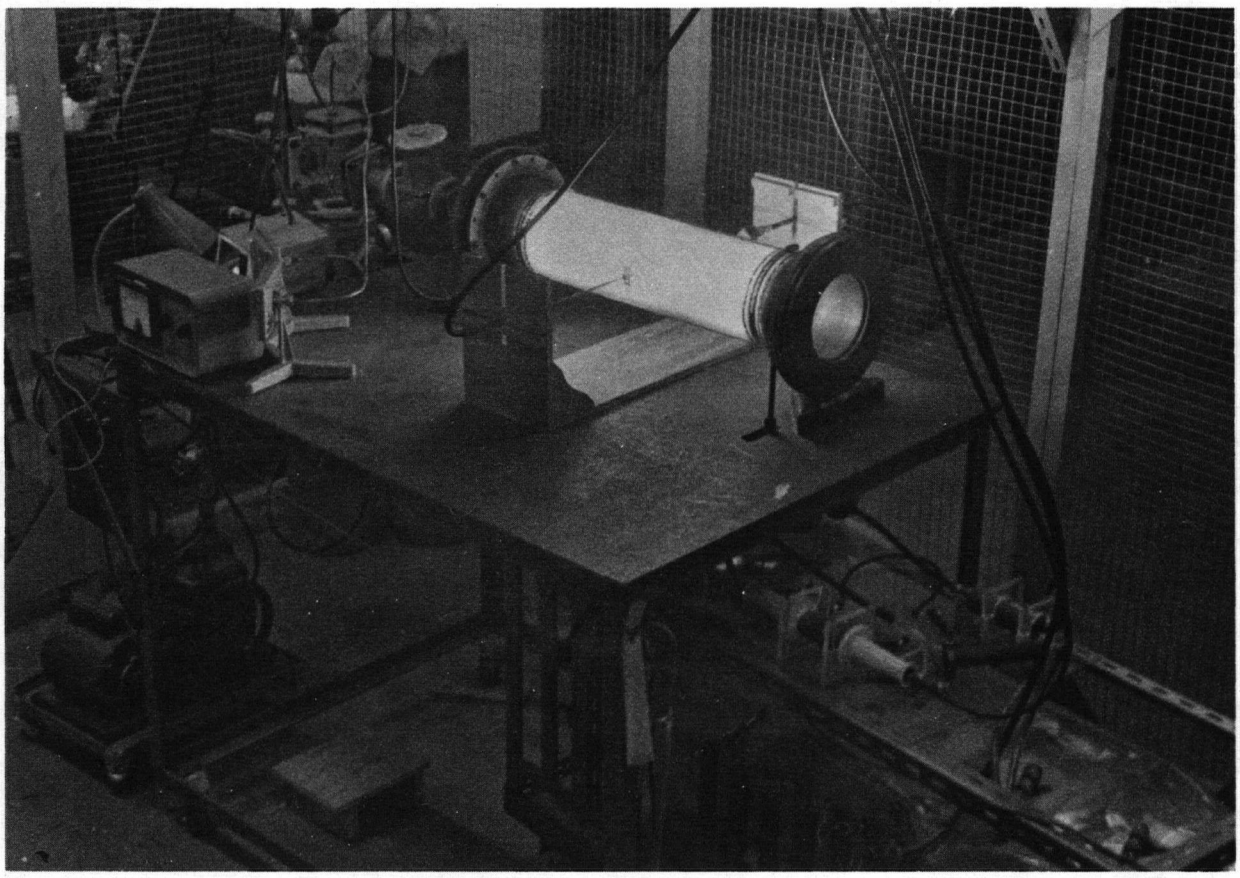

FIGURE 21. PHOTOGRAPH OF APPARATUS

7.0 APPARATUS (CONT'D.)

Discharge Vessel: (Cont'd.)

for the magnetic probes a quartz tube of .74 cm. outer diameter is placed diametrically across the Pyrex discharge vessel. This tube is sealed at the discharge vessel with Araldite epoxy resin. As a magnetic probe can be inserted through either end of the tube, we can obtain two radial observations of the magnetic field from a single discharge.

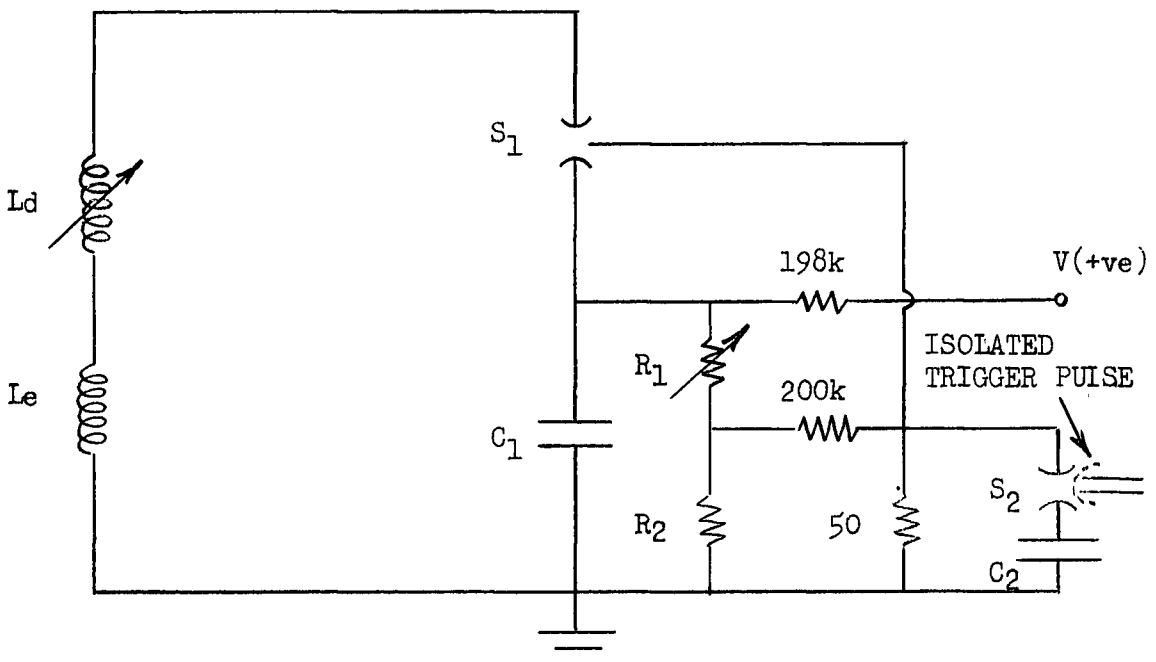

FIGURE 22. SCHEMATIC DIAGRAM OF APPARATUS

Ld = Inductance of discharge
Le = Inductance of external circuit (.12μH)
C1 = Main capacitor bank (53μF)
C2 = Trigger capacitor (.06μF)
S1 = Main spark gap switch
S2 = Trigger spark gap switch
R1 = Variable resistance (0 - 70 MΩ; 10 MΩ steps)
R2 = Voltage divider (150 MΩ)
V = Charging voltage
T = Trigger Pulse

7.0 APPARATUS (CONT'D.)

Capacitor Bank:

The capacitor bank (C1 of the schematic diagram of figure 22.) is formed by five N.R.G., low inductance, storage capacitors. These capacitors are charged to 10 kV for all experimental investigations which means that we have 2.6 kj. of stored energy.

7.0 APPARATUS (CONT'D.)

Capacitor Bank: (Cont'd.)

In the early part of the investigation the capacitors were often destroyed after repeated use ($\sim$ one hundred discharges), but since small ($\sim$166 pF.) high frequency, capacitors have been placed across each of the storage capacitors, there has been no such damage. It is thought that these capacitors may by-pass high frequency, high voltage transients on the discharge leads.

Triggering Circuit:

The triggering circuit for the present system is shown in figure 22. This circuit has two important features. First, the switch S_2 of figure 22. isolates the high voltage discharge circuit from the initial trigger generator. Secondly, this circuit is constructed coaxially in order to minimize the creation of radiated noise signals. The triggering circuit is described in detail by Medley (1965a).

Framing Camera:

A Barr and Stroud framing camera is used to obtain photographic measurements. In this camera the film remains stationary and a rotating mirror is used to pass light from the discharge through a series of fixed lenses as shown in the schematic of figure 23. In order to photograph the desired time-interval of the discharge, the position of the rotating mirror is used to trigger the discharge.

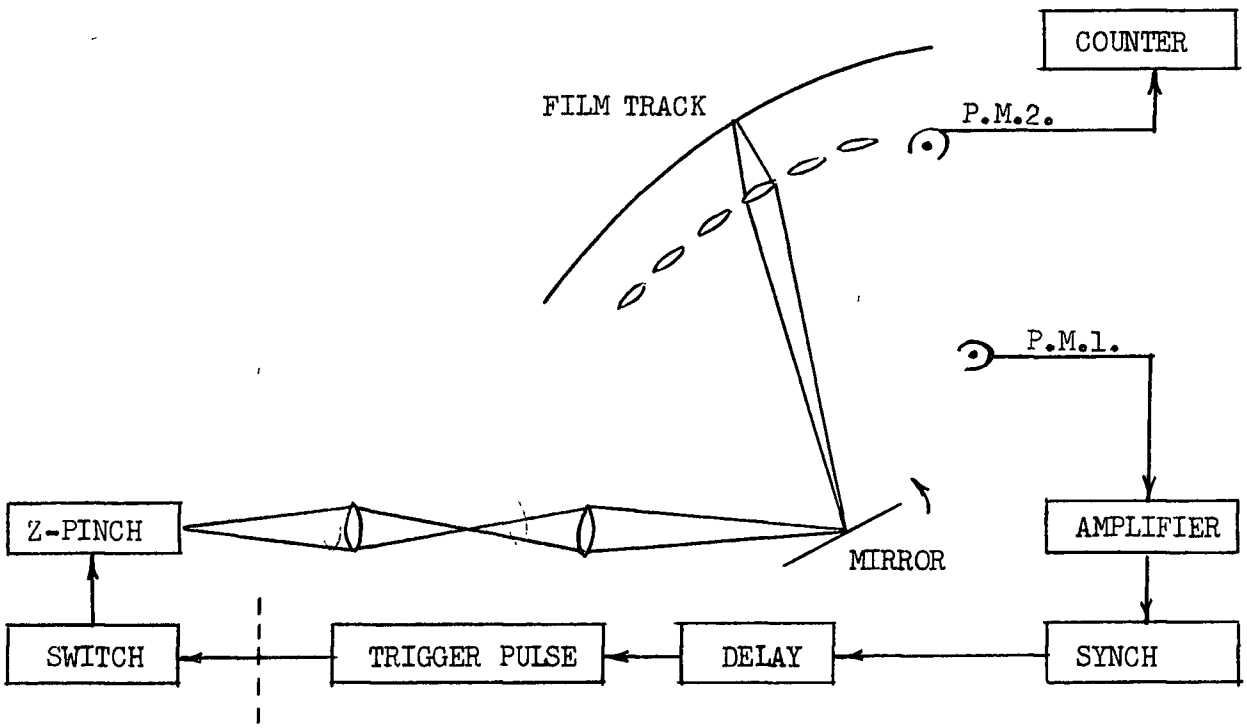

FIGURE 23. FRAMING CAMERA AND CONTROL EQUIPMENT

7.0 APPARATUS (CONT'D.)

Framing Camera: (Cont'd.)

A block diagram of the required triggering circuit is also included in figure 23., but we refer to Hodgson (1964) for a detailed explanation of the triggering operation. We will, however, explain the operation of the frequency meter designated by counter in figure 23; for this meter determines the exposure time for the photographs.

A small light source is provided in the framing camera which is focused on the rotating mirror and, at a certain mirror position, the reflection is recorded by a photo multiplier. Thus the photo

7.0 APPARATUS (CONT'D.)

Framing Camera: (Cont'd.)

multiplier records a pulse corresponding to each complete rotation of the mirror and a C.M.C. Model 201C counter is used to record the period (T) between these pulses at the time of firing the discharge. The manufacturers state that a mirror rotation of 5.5 kc/sec corresponds to a film exposure time of .125 μ sec. Thus we can determine the exposure time (e) from the period (T) as:

$$e = .125 \times 5.5 \times 10^{-3} \times T$$

where e and T are measured in micro seconds.

Typically T is of the order of 350 μ sec and thus e is approximately .24 μ sec.

TABLE I

CAPACITOR BANK AND LEADS

(N.R.G. Low Inductance Storage Capacitors)	
Total Capacity	53 μF
Total Inductance	.12 $\pm$ .01 μH
Width of Leads	15 cm.
Length of Leads	1 m.
Separation of Leads (Polyethylene)	2 mm.

DISCHARGE TUBE

Discharge Tube	Pyrex
Electrodes	Brass
Electrode Separation	59 cm.
Inside Tube Diameter	15 cm.
Outside Tube Diameter	17 cm.

7.0 APPARATUS (CONT'D.)

TABLE I (CONT'D.)

VACUUM SYSTEM

(Type 17 Balzers Oil Diffusion Pump)	
(Hyvac 14 Cenco Backing Pump)	
Base Pressure	1 μHg
Leak Rate	7 μHg/hr.

PRESSURE MEASUREMENT

(Type GP-110 Pirani Vacuum Guage)	
(Vacustat)	max. 1000 μHg

VOLTAGE MEASUREMENT

(Conway Microammeter)	
(in series with A.V.O. Multiplier)	25 kV d.c., 500 M
Charging Voltage	10.0 $\pm$ .3 kV

CURRENT MEASUREMENT

(Rogowski Coil)	
Integration Time Constant	180 μsec
Sensitivity	15.0 kamp volt.$^{-1}$
Maximum Discharge Current	150 kamp.
Discharge Current Frequency	50 kc/s

MAGNETIC FIELD MEASUREMENT

(Type 551 Tektronix Dual Beam Oscilloscope)	
(Type D "Plug in" Units)	
(Type 2620 Dumont Polaroid Oscilloscope Camera)	
Magnetic Probe Sensitivity	4.9 wbm^{-2} volt^{-1}

PHOTOGRAPHIC MEASUREMENT

(Model CP5 Barr & Stroud Framing Camera)	
(H.P. 3 Ilford Photographic Film)	
Number of Frames/Discharge	60
Exposure Time	.25 μsec
Time Between Frames	.25 μsec

7.1 DISCHARGE PARAMETERS

In this section we present four separate experimental measurements. Three of these are observations of phenomena associated with the plasma discharge; namely, the discharge current, voltage, and emission of light. The fourth is a measurement of the inductance of the discharge circuit - excluding the inductance of the discharge vessel. This inductance is required for theoretical calculations in Part III.

Discharge Current:

The discharge current is measured with a Rogowski coil which is effectively a large magnetic probe. It is constructed from a 15 cm. length of the inner conductor of RG65 A/U delay line. The coil is placed between the flat copper leads to the discharge vessel with the axis of the coil perpendicular to the direction of current flow in the leads.

Like the magnetic probe the output signal of the Rogowski coil must be integrated to obtain a signal proportional to the magnetic field or the discharge current. The same R.C. - type integrator is used as has been described for the magnetic probe in section 3.1, but now the integration time constant is 180 μ sec.

Again, as with the probe, we must check the frequency response of the Rogowski coil and measuring circuit (including the integrator). The signal cable is terminated with 47Ω as is, then, the Rogowski coil.

7.1 DISCHARGE PARAMETERS (CONT'D.)

Discharge Current: (Cont'd.)

This impedance is much less than the characteristic impedance of the Rogowski coil (1000Ω) and we expect, therefore, that signals at high frequencies will be attenuated (see Segre (1960)). Still, the conditions for reliable integration of the input signal (see section 3.1) are satisfied for frequencies (f) less than 500 kc/s (experimentally verified) and as the frequency of the discharge current is approximately 50 kc/s (see, for example, figure 29.), then more accurate matching is unnecessary.

Typical current traces corresponding to the three initial pressures of 100, 250, and 500 μHg argon are illustrated in figure 24. These particular traces are obtained by magnifying the polaroid film from the oscilloscope camera with a photographic enlarger. The traces are normalized in the following way.

An enlargement of a graticule area of 100 μsec-volts is also included in figure 24. This area is used to calibrate a planimeter which is then used to determine the area under the current traces in μsec-volts. It is known that this area must be equivalent to the total charge on the capacitor bank:

$$\int I dt = Q = CV$$

where I is the discharge current

Q is the charge on the capacitor

C is the capacitance

V is the charging voltage.

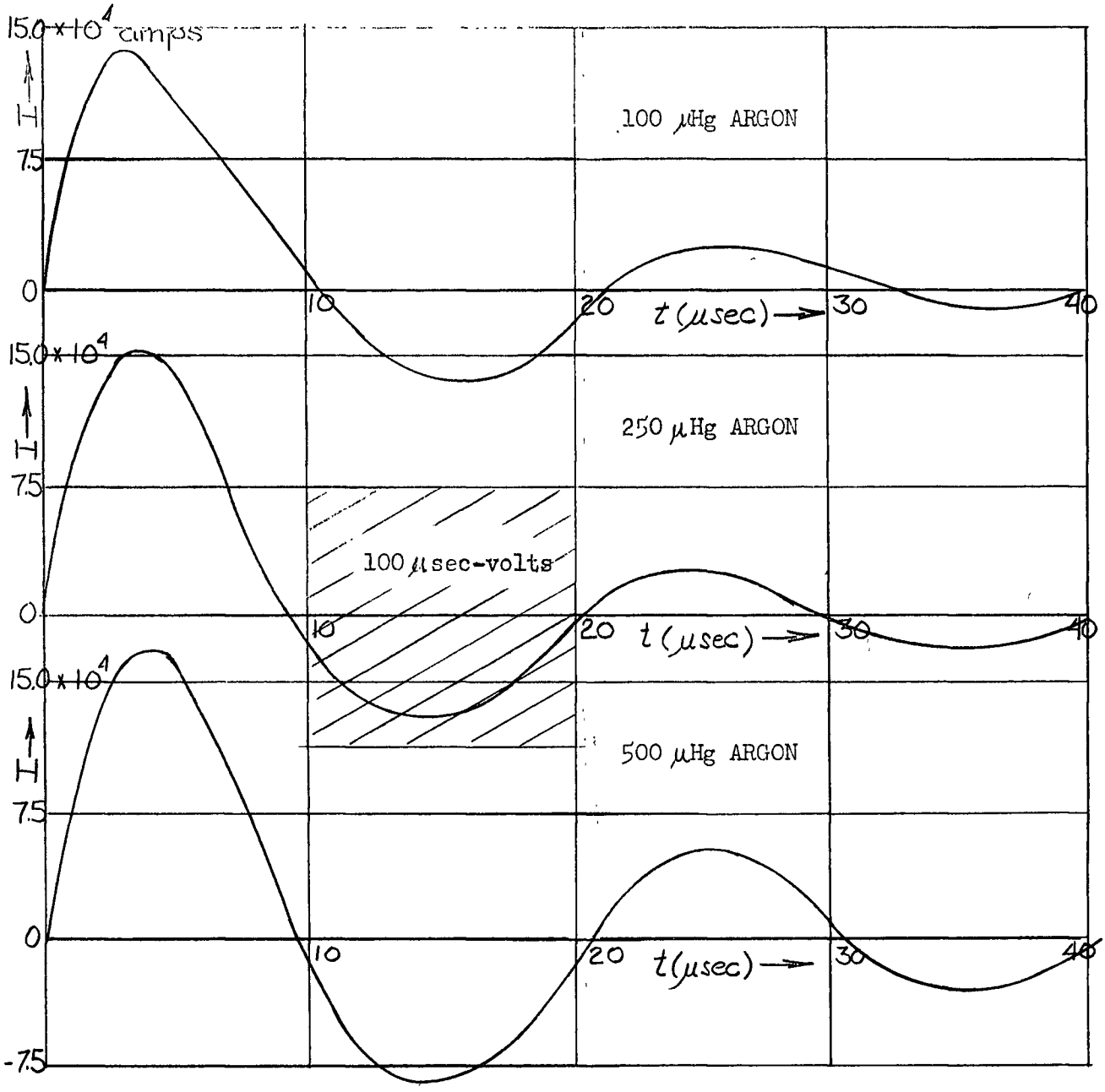

FIGURE 24. DISCHARGE CURRENT

7.1 DISCHARGE PARAMETERS (CONT'D.)

Discharge Current: (Cont'd.)

We conclude that 1 volt of deflection on the oscilloscope is equivalent to a discharge current of 15,000 amperes. The error associated with the calibration procedure is relatively large (10%). The largest source of error is in the planimeter measurement of the area under the current trace.

Discharge Voltage:

Voltage measurement is obtained by using a 1000:1 Tektronix high voltage probe Type P6013. The measurement is taken across the discharge end of the current leads. The results are shown in figure 25., and it is obvious that considerable noise signals are associated with this measuring technique (observe the accompanying current wave forms in figure 25. as compared with those of figure 24.) However, for the present purpose an estimate is sufficient, and it is noted that any detail in figure 25. is unreliable. At higher pressures the voltage across the discharge tube is approximately constant at 2.5 - 3.0 kV for the first 4 μsec.

INITIAL PRESSURE	PEAK LUMINOSITY
100 μHg Argon	5.5 $\pm$ .5 μsec
250 μHg Argon	7.7 $\pm$ .5 μsec
500 μHg Argon	10.0 $\pm$ .5 μsec

TABLE II TIME OF MAXIMUM LUMINOSITY

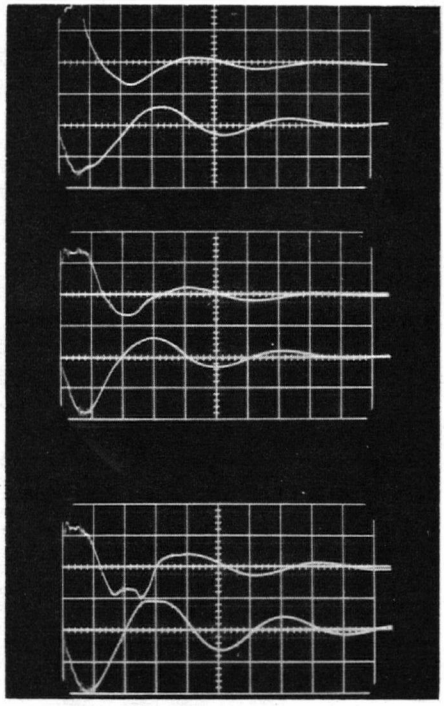

FIGURE 25. OSCILLOSCOPE TRACES OF DISCHARGE VOLTAGE

Upper Trace: Voltage across discharge leads (2,000 volts/cm.)
Lower Trace: Current from Rogowski coil (75,000 amps/cm.)

Time Base: 5 μsec/cm.

7.1 DISCHARGE PARAMETERS (CONT'D.)

Discharge Luminosity:

The intensity of the light emitted by the discharge is monitored with a Phillips photo multiplier Type CVP-150. The photo multiplier is placed at the side of the discharge vessel at the height of the

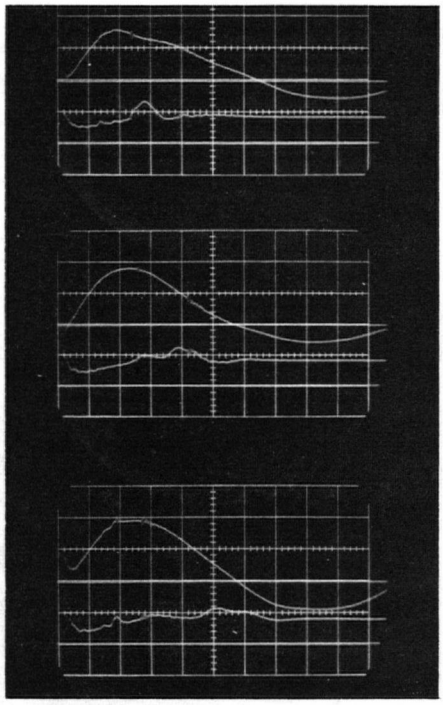

FIGURE 26. OSCILLOSCOPE TRACES OF DISCHARGE LUMINOSITY

Upper Trace: Rogowski coil (75,000 amps/cm.)
Lower Trace: Photo multiplier (10 volts/cm.)

Time Base: 2 μ sec/cm.

7.1 DISCHARGE PARAMETERS (CONT'D.)

Discharge Luminosity: (Cont'd.)

discharge axis, and it samples the light emitted from a section of the discharge midway between the magnetic probe guide and the discharge electrode. The photo multiplier has a 1000 Ω load

Discharge Luminosity: (Cont'd.)

resistance and it has 850 volts d.c. anode potential. The light input to the photo multiplier is attenuated by a factor of 1000 by using a neutral density 3.00 filter and signal output is displayed on an oscilloscope and photographed on polaroid film. The resulting photograph for the three initial pressures of argon - 100, 250, and 500 μHg, is shown in figure 26. and the time corresponding to the peak light emission is given in Table II for the three initial pressures. We assume that peak light emission coincides with the time of the pinch, i.e. the plasma has been constricted to its minimum volume.

External Circuit Inductance:

The external circuit inductance, i.e. the inductance of discharge capacitors and leads, is determined by the following procedure. The electrodes of the main spark gap switch (see figure 22.) are placed in contact thus shorting out the switch. The capacitor bank is charged to a few hundred volts with the discharge circuit open-circuited at the discharge tube. The discharge leads are then connected - shorting out the discharge vessel inductance and completing the circuit (see figure 22.) - and the ringing frequency of the circuit current is monitored with the Rogowski coil. Assuming the capacitance of the circuit is known (C_1 of figure 22.) then the inductance may be calculated. The external inductance is calculated to be .12 $\pm$ .01 μH.

8.0 MAGNETIC PROBE MEASUREMENT

In this section we describe the experimental procedure which is used to obtain measurement of the magnetic field in the z-pinch discharge. Probes of the type described in section 3. are inserted into each end of the quartz guide tube which runs diametrically across the discharge vessel midway between the electrodes. The outputs from the probes are displayed simultaneously on a dual beam oscilloscope. We are assuming that the discharge plasma is rotationally symmetric and thus we can meaningfully compare the two signals.

The radial position of the probe coil is determined by first centering the probe coil on the axis of the discharge vessel (using a travelling microscope). With the probe in this position, the probe stem is marked at a point coinciding with the end of the quartz guide tube. Then the probe stem is marked off in 2.5 mm. intervals relative to this "zero" mark. Thus we place the probes at the desired radial positions, trigger the discharge, and measure the magnetic field as a function of time at these given radial positions (see, for example, figure 27.).

However, in order to calculate the current density distribution we have seen in section 5 that we require the radial distribution of the magnetic field at a given time and not the magnetic field as a function of time at a given radius (as we measure experimentally). If we assume that the discharge process is reproducible from discharge to discharge, and if we assume that the oscilloscope is

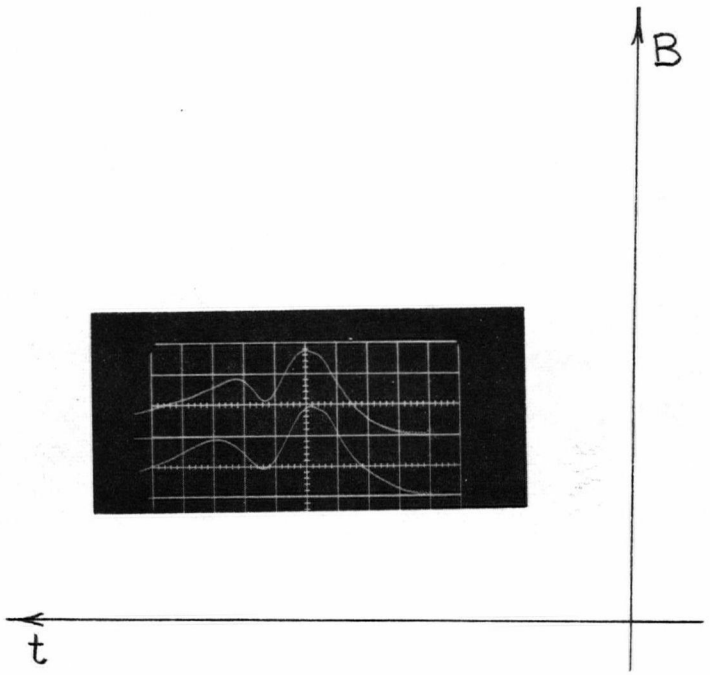

FIGURE 27. OSCILLOSCOPE TRACES OF MAGNETIC FIELD

Upper Trace: r = 2.25 cm. (.245 wb/m^2/cm.)
Lower Trace: r = 3.0 cm. (.245 wb/m^2/cm.)

Time Base: 1 μsec/cm.
Time Delay: 0.5 μsec
Initial Pressure: 100 μHg.

8.0 MAGNETIC PROBE MEASUREMENT (CONT'D.)

triggered at the same point in the development of the discharge for each discharge, then from each of our observed traces of the magnetic field at given radius we can pick out the value of the field at a selected time and thus construct the desired radial distribution of the magnetic field corresponding to the selected time.

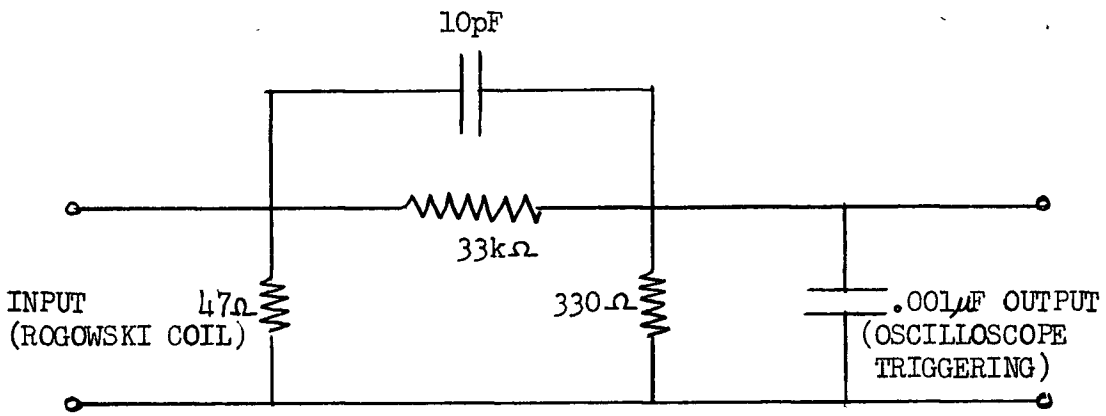

FIGURE 28. COMPENSATED ATTENUATOR

8.0 MAGNETIC PROBE MEASUREMENT (CONT'D.)

This measured magnetic field distribution is then corrected by the procedure outlined in section 5.

In the above procedure we have made three assumptions which we must now verify. But first we must describe the method of triggering the oscilloscope traces.

Throughout the experimental measurements, we have triggered the time base of the oscilloscope by using the external triggering mode with a signal supplied from the Rogowski coil. In this case, the signal is not integrated as we are interested in the fast rise time (.2 μ sec) of the large dI/dt signal (500 volts). This signal must be attenuated and the compensated attenuator of figure 28. is used which thus retains the fast rise time.

8.0 MAGNETIC PROBE MEASUREMENT (CONT'D.)

Now, to experimentally check the three previous assumptions - rotational symmetry, reproducibility of the plasma discharge, and reproducibility of triggering - we perform the following two tests. In figure 29., we superimpose the two traces from the probes which are placed at corresponding radial positions on opposite sides of the discharge. The result shows that the discharge is symmetrical within our measuring accuracies and it also illustrates the equivalence of the two probe measuring circuits. In figure 30., we superimpose the traces of several discharge shots for fixed probe positions and again within experimental accuracies the triggering and discharge reproducibilities are apparent. A previous investigation by Andrianov (1959) has also illustrated that the z-pinch plasma is reproducible up to times corresponding to the first constriction of the discharge plasma.

The experimental procedure is to record magnetic field (B) vs. time (t) at 2.5 mm. intervals from radius (r) equal to 0 to 85 mm. Then from this set of results it is possible to determine magnetic field (B) vs. radius (r). We choose to examine B(r) at 1 μ sec intervals with t=0 corresponding to the initiation of discharge current. The experimental results are shown in figures 31 - 33. The calibration of the magnetic probe is given in the following section, and in section 8.2 we compute the corrected magnetic field and current density distributions.

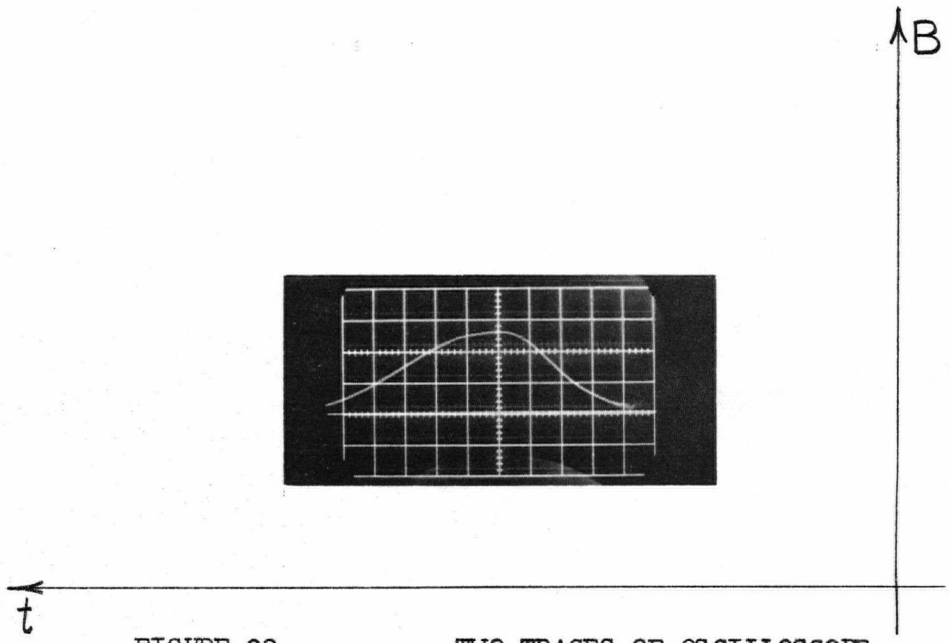

FIGURE 29. TWO TRACES OF OSCILLOSCOPE SUPERIMPOSED

Upper Trace: r = 6.25 cm. (.196 wb/m^2/cm.)
Lower Trace: r = 6.25 cm. (.196 wb/m^2/cm.)

Time Base: 1 μsec/cm.
Time Delay: 0.5 μsec
Pressure: 500 μHg Argon

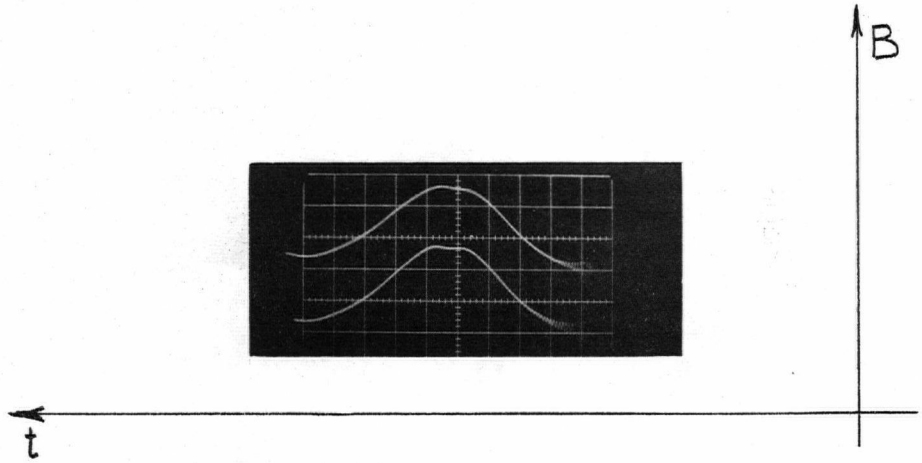

FIGURE 30. TRACES FROM FOUR DISCHARGES SUPERIMPOSED

Upper Trace: r = 5.0 cm. (.245 wb/m^2/cm.)
Lower Trace: r = 5.0 cm. (.245 wb/m^2/cm.)

Time Base: 1 μsec/cm.
Pressure: 250 μHg Argon
Time Delay: 0.5 μsec.

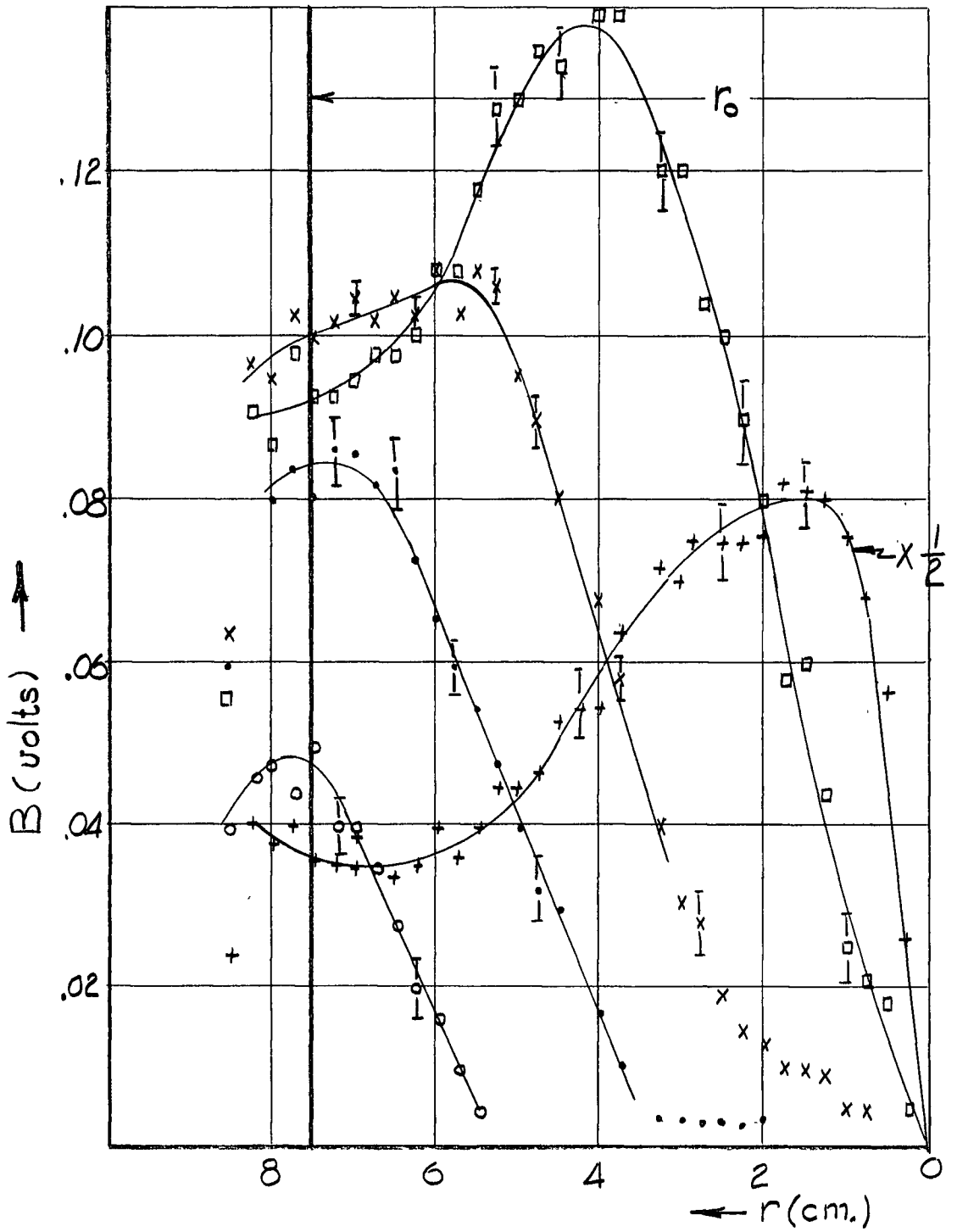

FIGURE 31. MEASURED MAGNETIC FIELD (100 μHg Argon)

o t = 1 μsec
• t = 2 μsec
x t = 3 μsec
□ t = 4 μsec
\+ t = 5 μsec

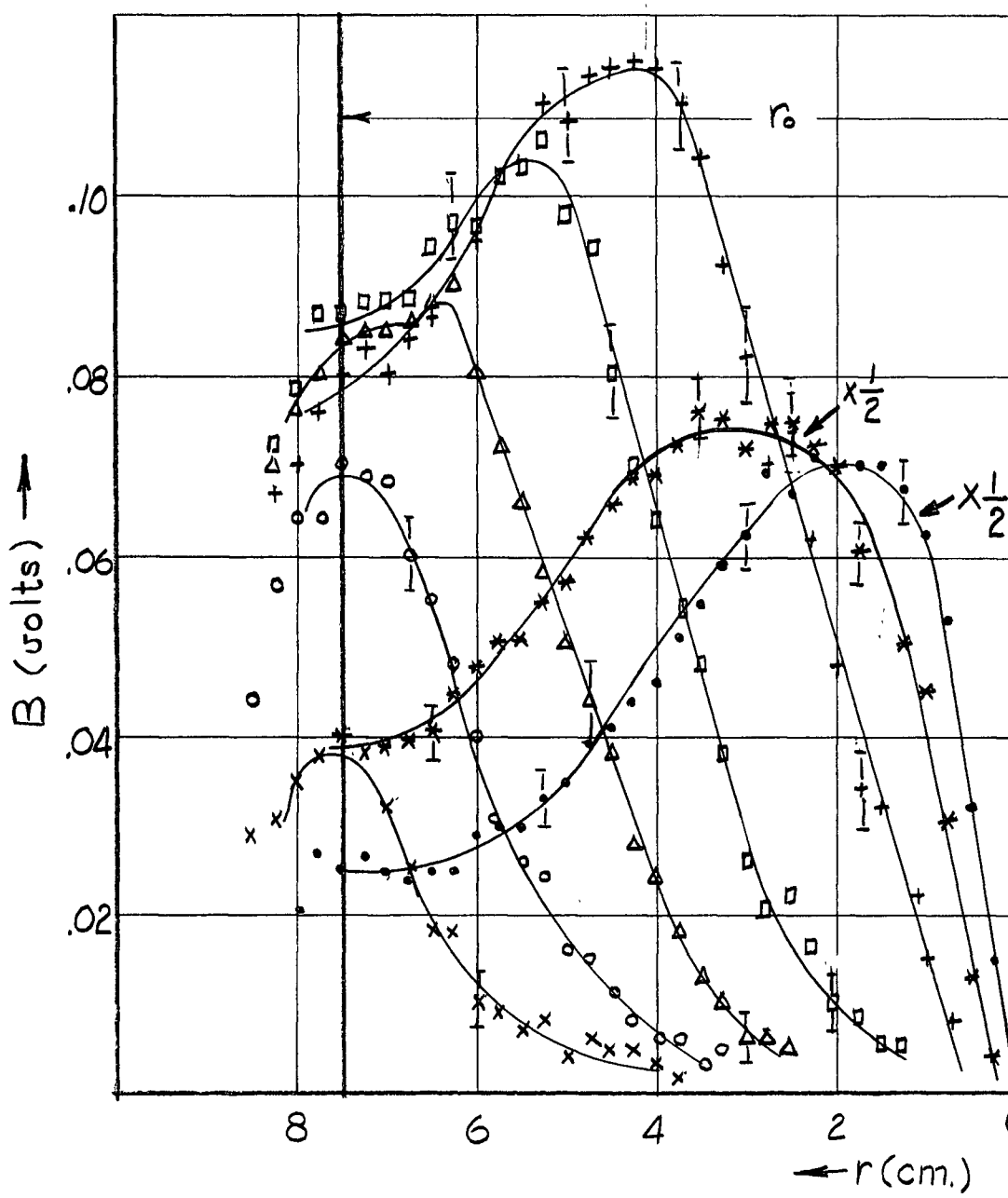

FIGURE 32. MEASURED MAGNETIC FIELD
(250 μHg Argon)

× t = 1 μsec
○ t = 2 μsec
△ t = 3 μsec
□ t = 4 μsec
+ t = 5 μsec
✱ t = 6 μsec
• t = 7 μsec

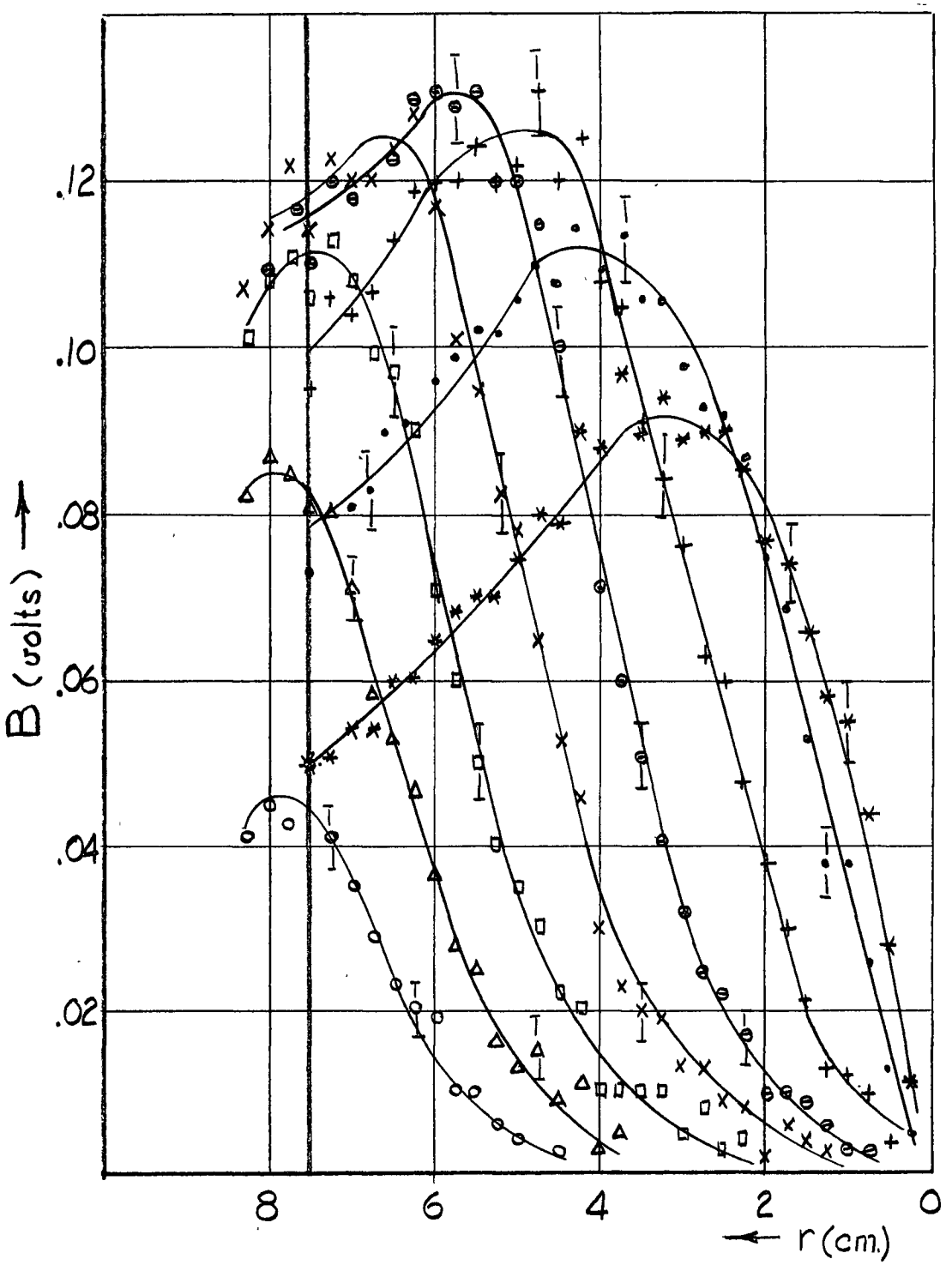

FIGURE 33. MEASURED MAGNETIC FIELD
(500 μHg Argon)

o t = 1 μsec	⊙ t = 5 μsec
Δ t = 2 μsec	+ t = 6 μsec
□ t = 3 μsec	• t = 7 μsec
x t = 4 μsec	* t = 8 μsec

8.1 MAGNETIC PROBE CALIBRATION

The magnetic probe can be calibrated if a well known magnetic field is available. A simple technique is now described which makes use of the experimental apparatus and the results of the analogue experiment of section 3.

It has been shown in section 4.3 that in the plane of the current sheet, i.e. $z = 0$,

$$\Delta B(0) = \frac{1}{2} \mu_o \gamma J_o$$

Now if we consider the magnetic field at a point in the plane of the return conductor of the discharge vessel (where the probe punctures the return conductor), then we expect the measured field to be due to the field error alone as there would be no magnetic field outside the return conductor if there were no probe hole through it.

Thus, $$B(r_o, t_o) = \Delta B(0) = \frac{1}{2} \mu_o \gamma J_o(t_o)$$

where r_o is the radius of the return conductor

t_o is the time of observation

$J_o(t_o) = I(t_o) / 2\pi r_o \gamma$

$I_o(t_o)$ is the current in the return conductor

γ is the thickness of the return conductor.

However, as the magnetic field gradient is large about the point $r = r_o$, and as it is difficult to position the magnetic probe coil accurately, the calibration procedure is improved by

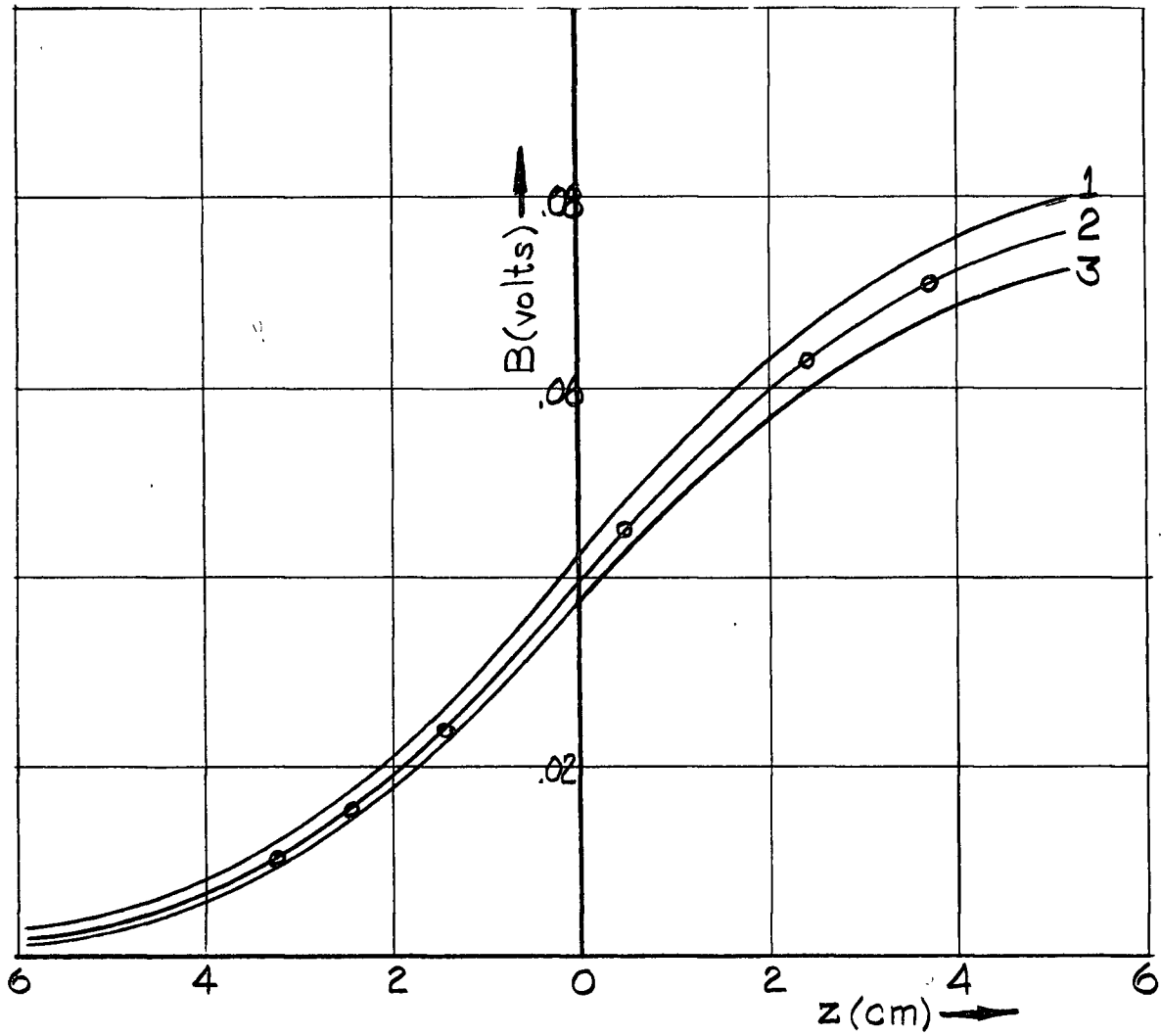

FIGURE 34. DETERMINATION OF B(o)

Analogue correction for ρ_o = .35 cm.

Correction 1	B(o) = .038 volts
Correction 2	B(o) = .040 volts
Correction 3	B(o) = .042 volts

o Experimental points measured near return conductor of discharge circuit.

8.1 MAGNETIC PROBE CALIBRATION (CONT'D.)

measuring the magnetic field as a function of radius, for points both inside and outside the current sheet. These points are then fitted to theoretical curves with varying normalization constants and from the curves of figure 34. it appears that $B(r_o,t_o)$ = .040 volts.

8.1 MAGNETIC PROBE CALIBRATION (CONT'D.)

These theoretical curves are plotted from the analogue results of section 4.3.

The time (t_o) is chosen as the time when $I(t_o)$ = I max. This choice has several advantages. First, the measured signal is largest at $t = t_o$; second, the current magnitude is insensitive to measuring error in t_o at $I(t_o)$ = I max.; and third, the discharge current has moved well away from the wall of the discharge vessel at this time and the field in the vicinity of the return conductor is due to the return current alone. With an initial pressure of 500 μHg of argon, t_o is approximately 4 μsec.

A measurement of the discharge current by the Rogowski coil is required to complete the calculation, since:

$$\Delta B(0) = \frac{\mu_o I_o (t_o)}{4\pi r_o}$$

However, the Rogowski coil has already been calibrated (section 7.1), and from figure 24., the current at $t = 4$ μsec for an initial pressure of 500 μHg argon is known to be 166 kamp. Thus,

$$\Delta B(0) = \frac{\mu_o I_o (t_o)}{4\pi r_o}$$

$$.040 \times \text{CAL.} = 4\pi \times \frac{10^{-7} \times 1.66 \times 10^5}{4\pi \times 8.5 \times 10^{-2}}$$

or,

$$\text{CAL.} = 4.9 \ \frac{\text{wb/m}^2}{\text{volt}}$$

8.2 COMPUTED RESULTS

The corrected current density distributions as functions of time in the z-pinch discharge are obtained by using the computer program developed in section 5.1 with the measured magnetic field distributions of section 8.0. These measured results must, however, be adjusted in two ways. First, the measured field values are converted to M.K.S. units by using the calibration factor obtained in section 8.1. Secondly, the measured field values in the vicinity of the discharge wall (i.e. for large values of r) must be corrected for perturbation of the field caused by the penetration of the probe through the return conductor. As the current density in the return conductor is much greater than the current density in the hypothesized current sheets of the plasma (see figure 16.), the field correction associated with the return conductor is appreciable over a larger range (about 20 mm.) compared to the usual correction (about 10 mm.). The effect is shown in the diagram of figure 35. The correction is easily applied as we know the current in the return conductor from the Rogowski coil measurement of section 7.1 and the form of the correction from section 4.3.

It is interesting to note that this correction must be added to the already considerable correction which is applied to the magnetic field in the vicinity of the wall of the discharge vessel (see figure 35.). In particular, if the thickness of the wall of the vessel is comparable to, or less than, the radius of the hole punctured in the return conductor, then this correction would be very large. If the correction were large and if it were not applied

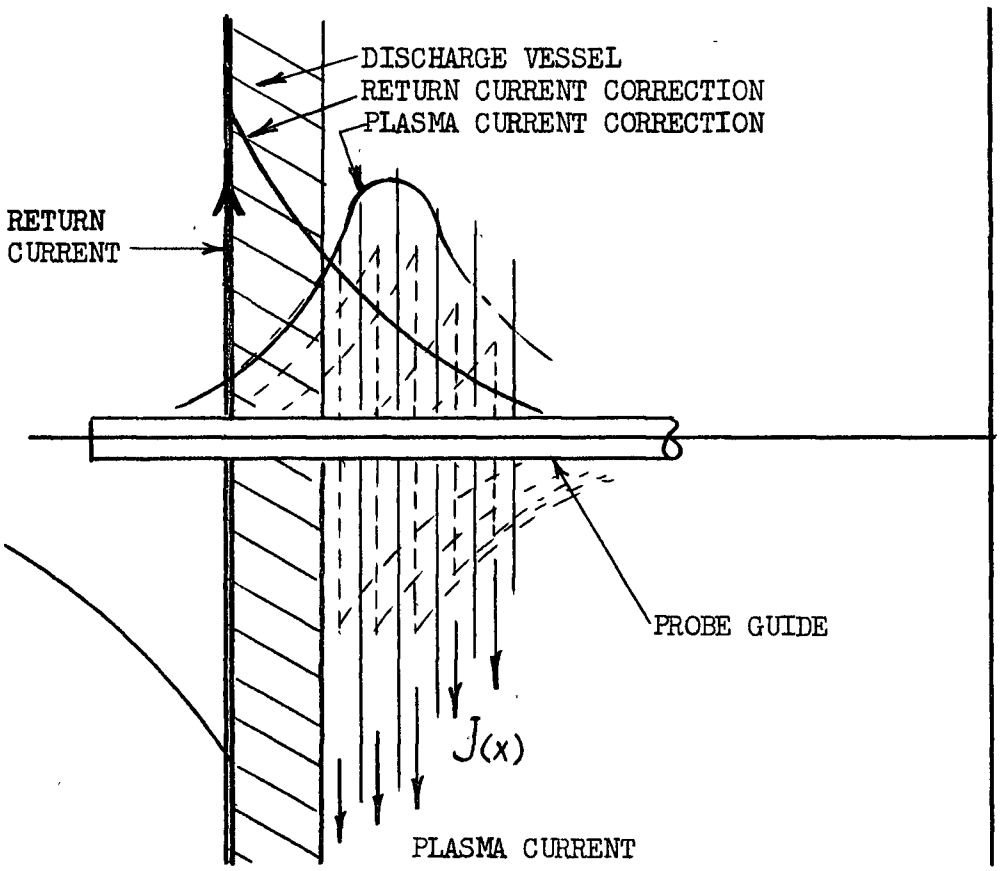

FIGURE 35. MAGNETIC FIELD CORRECTION AT WALL OF VESSEL

8.2 COMPUTED RESULTS (CONT'D.)

to the measured magnetic field, then the calculation would result in an apparent negative current at the wall of the vessel.

In section 5.1 we have developed two methods of solution. In one case we solve first for the current density (Equation 1.) and

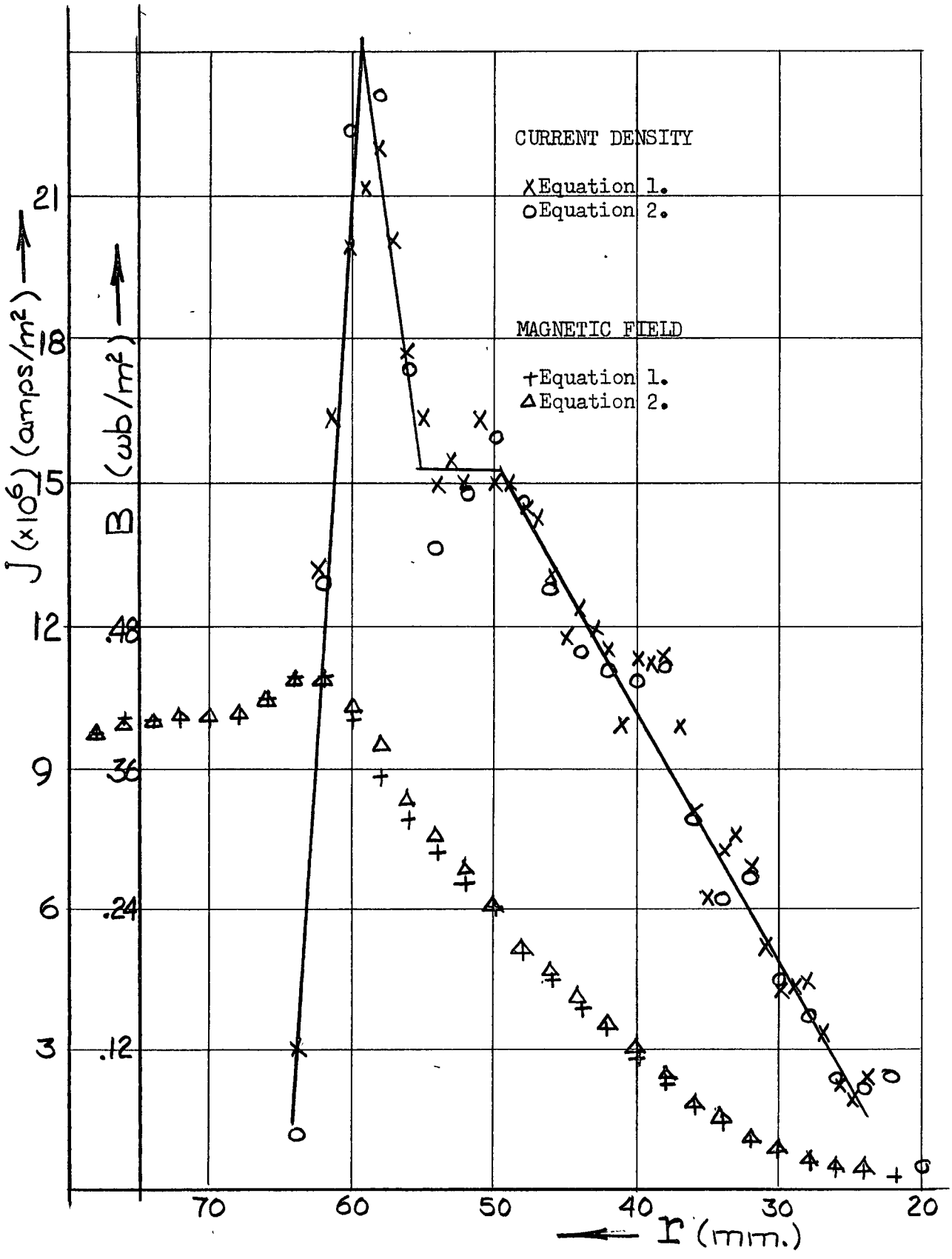

FIGURE 36. RESULTS FROM TWO METHODS OF SOLUTION

Time: 3 μsec
Initial Pressure: 250 μHg Argon

8.2 COMPUTED RESULTS (CONT'D.)

in the other case we solve first for the magnetic field (Equation 2.). In figure 36. we have examined the results from one experimental measurement (250 μHg, 3 μsec) and we have determined both the magnetic field and the current density for these two methods of solution. The comparison shows that the two solutions are equivalent.

Using Equation 1. (section 5.1) we determine the current density distributions corresponding to each of the measured magnetic field distribution of figures 31. - 33. These current density distributions are plotted in figures 37. - 42.

One characteristic feature of these graphs is the presence of a distinct current density spike at the outer edge of the distribution. This corresponds to a relatively thin current sheet which carries a considerable fraction of the discharge current. We have seen in section 5.2 that our numerical program tends to give a lower limit to the actual current density maximum. Thus it is most probable that the actual current density maximum is as much as four times greater than that indicated in the graphs of figures 37. - 42., and that the current sheet is correspondingly thinner. The knowledge of the existence of a thin current sheet is important since all theoretical models for z-pinch dynamics assume the presence of such a sheet although this has never been established experimentally. These theoretical models will be discussed in Part III of the thesis.

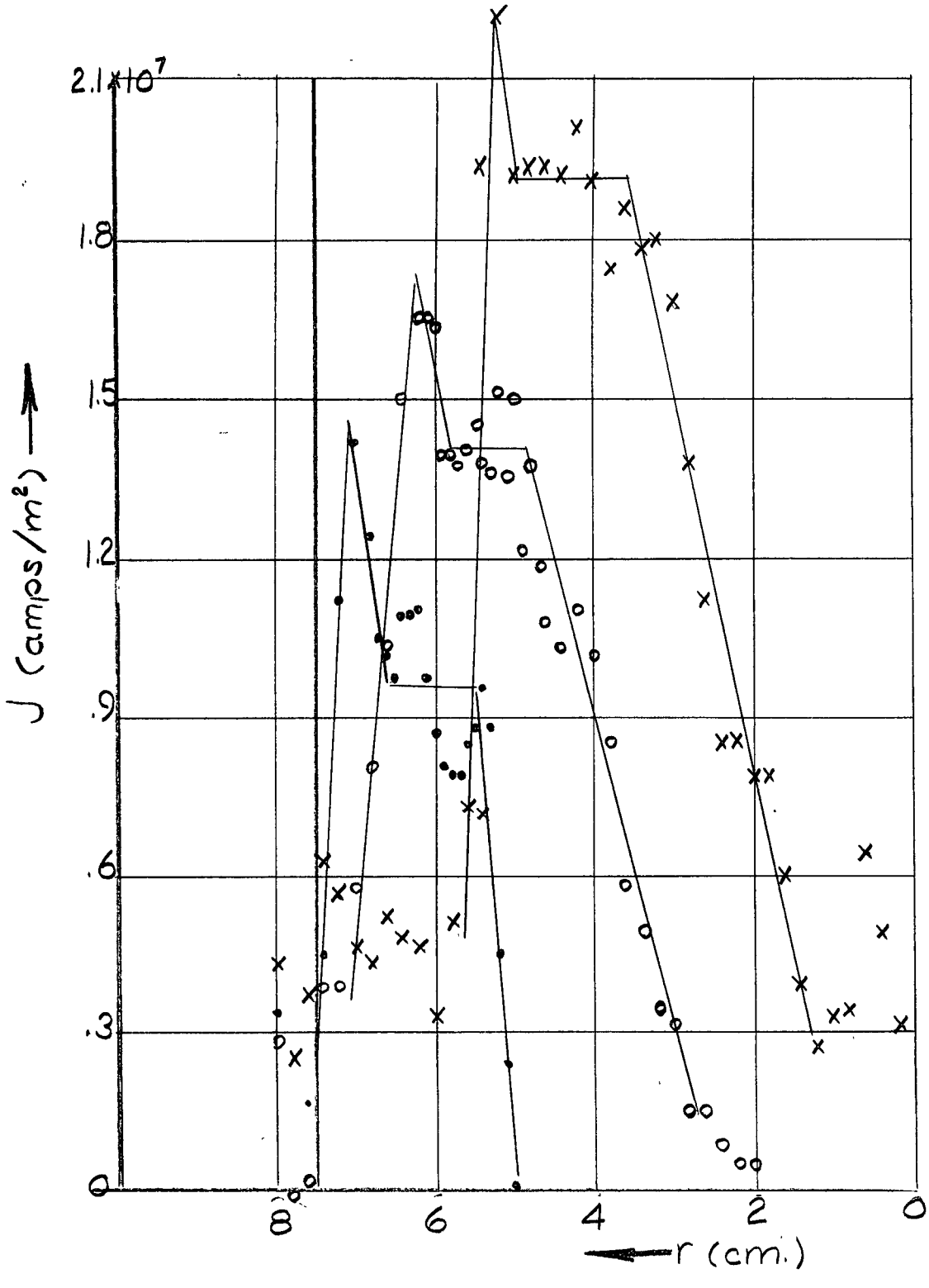

FIGURE 37. COMPUTED CURRENT DENSITY DISTRIBUTION

Initial Pressure: 100 μHg Argon
Time: 1 μsec •
2 μsec o
3 μsec x

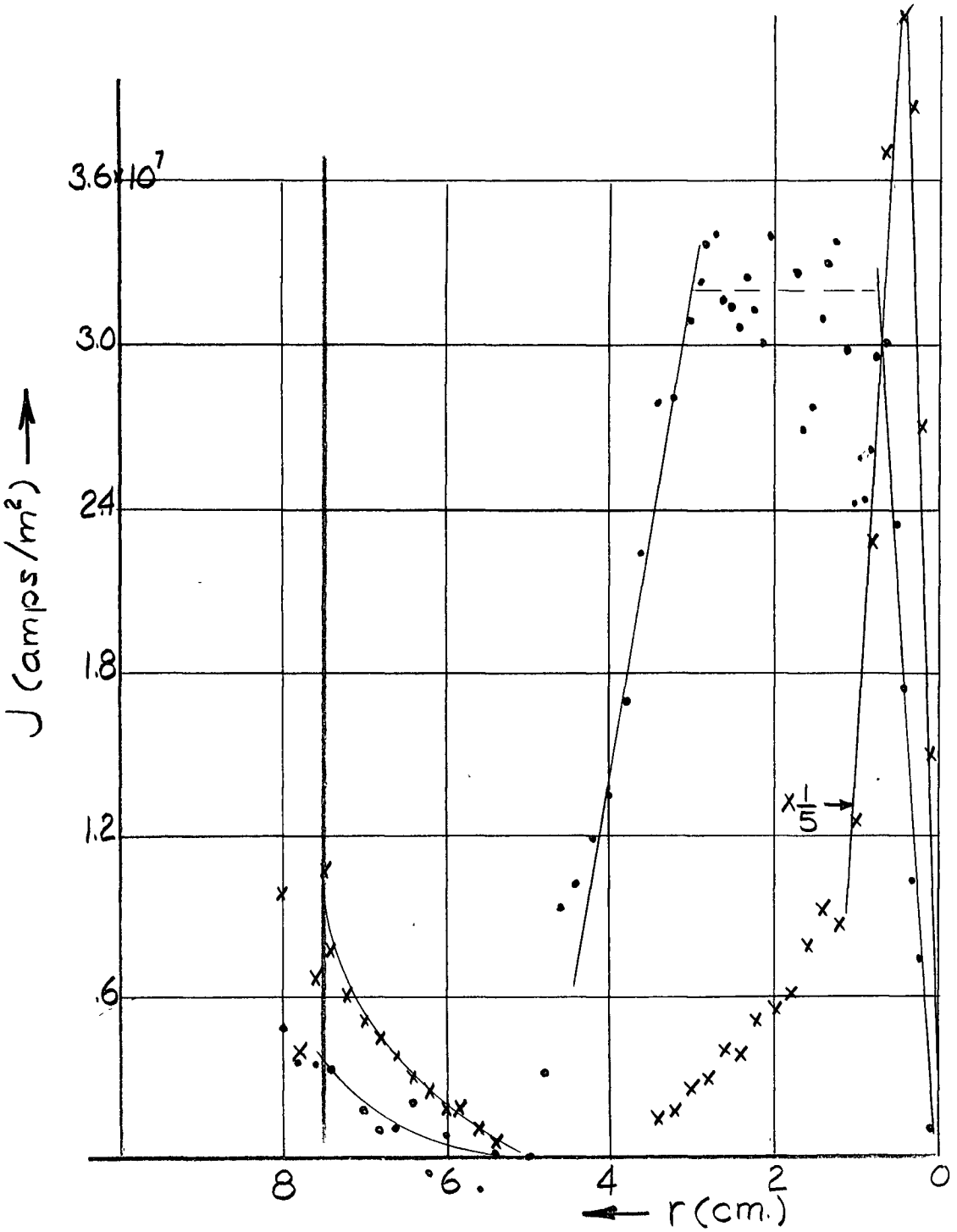

FIGURE 38. COMPUTED CURRENT DENSITY DISTRIBUTION

Initial Pressure: 100 μHg Argon
Time: 4 μsec •
5 μsec x

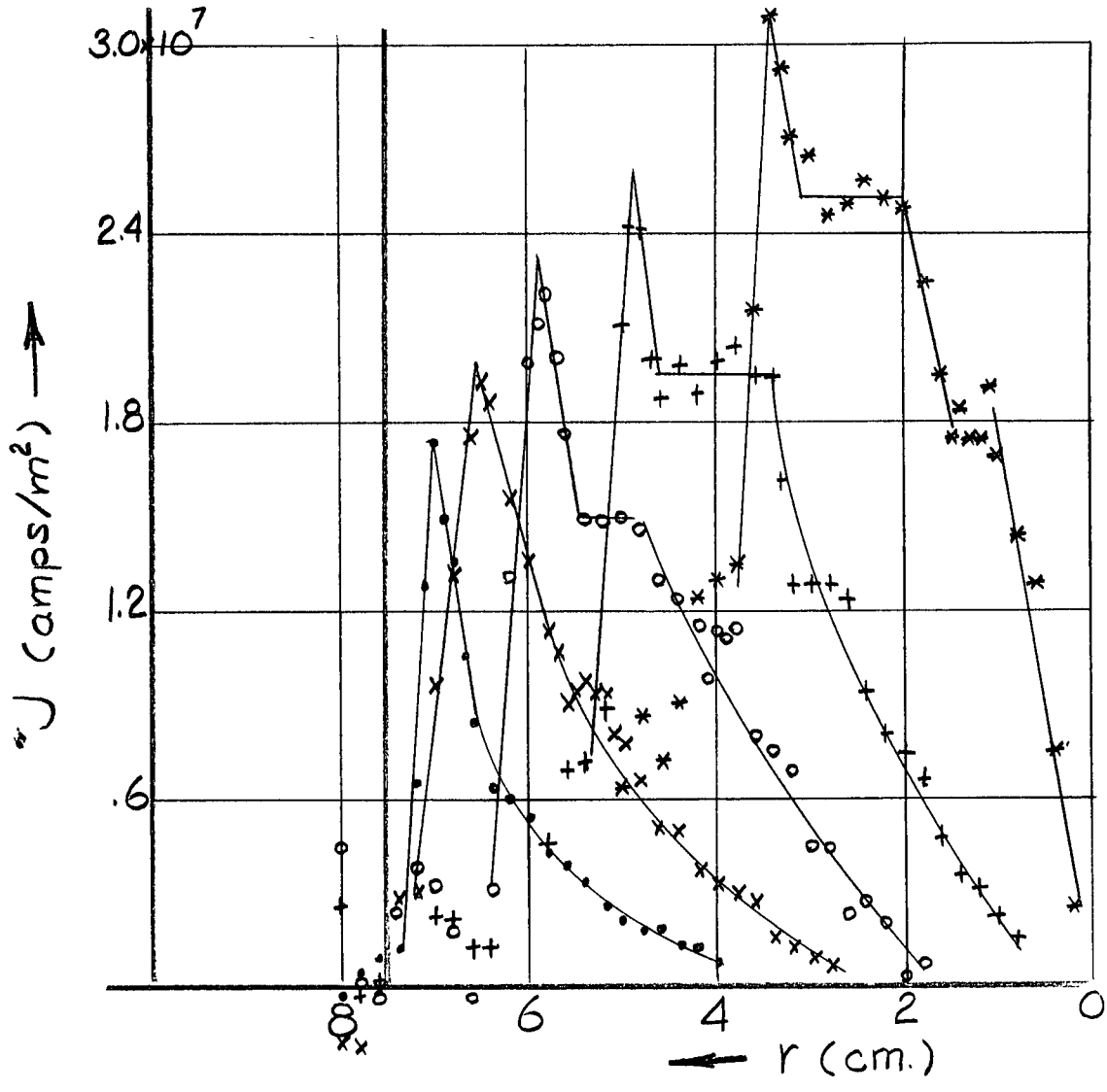

FIGURE 39. COMPUTED CURRENT DENSITY DISTRIBUTION

Initial Pressure: 250 μHg Argon

Time:				
1 μsec	•	4 μsec	+
2 μsec	x	5 μsec	*
3 μsec	o		

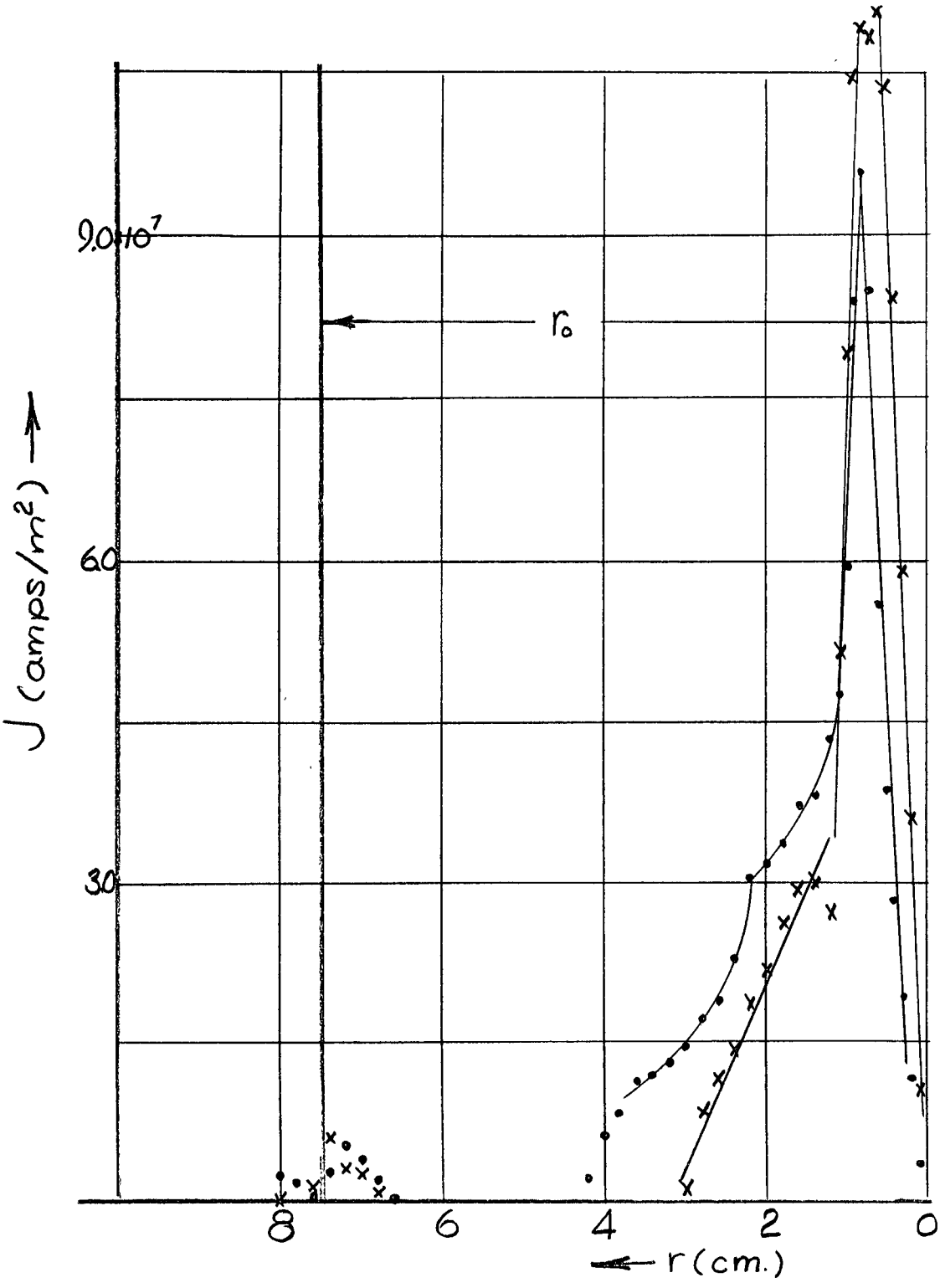

FIGURE 40. COMPUTED CURRENT DENSITY DISTRIBUTION

Initial Pressure: 250 μHg Argon
Time: 6 μsec • 7 μsec x

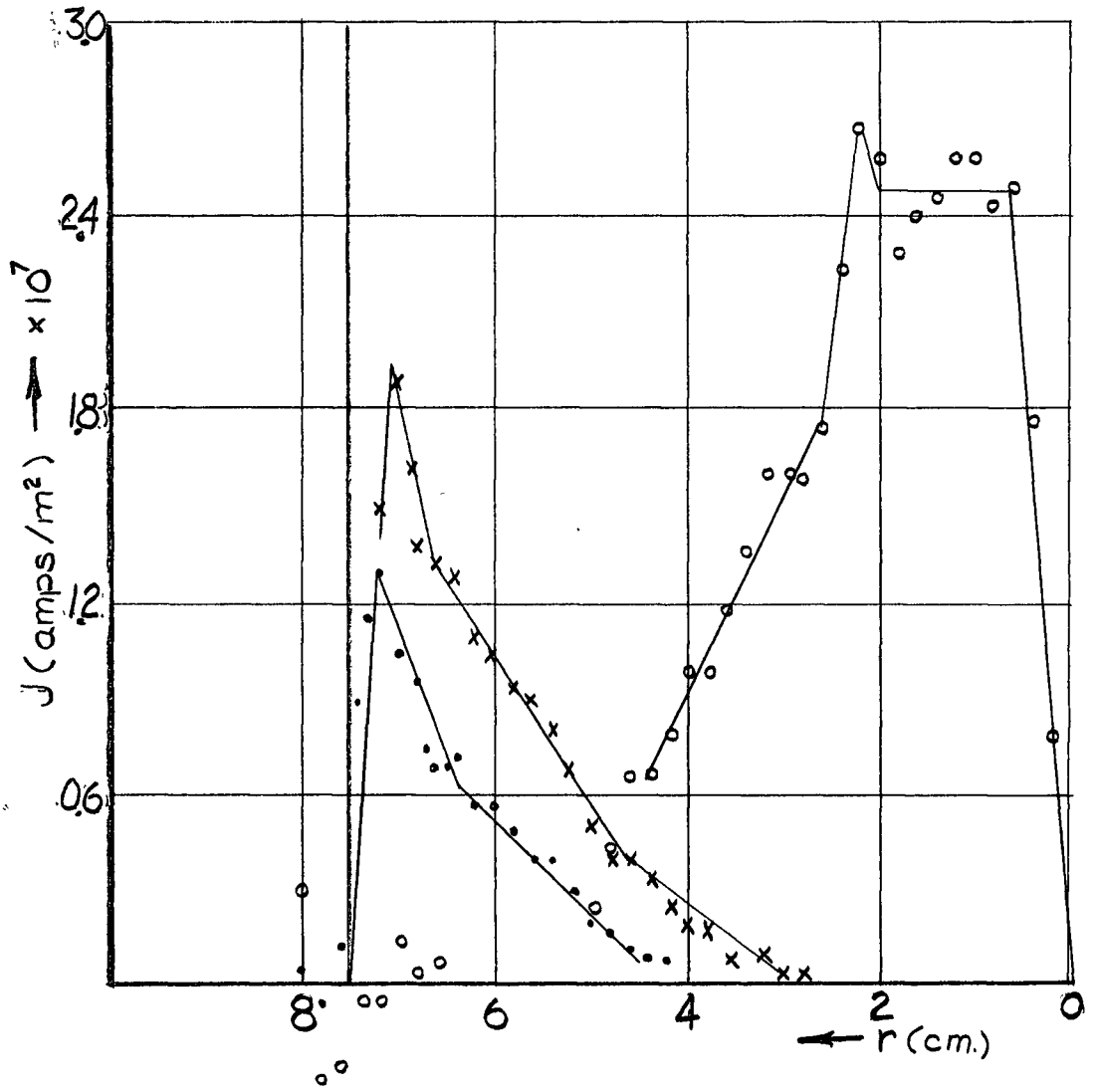

FIGURE 41. COMPUTED CURRENT DENSITY DISTRIBUTION

Initial Pressure: 500 μ Hg Argon
Time: 1 μsec •
2 μsec x
7 μsec o

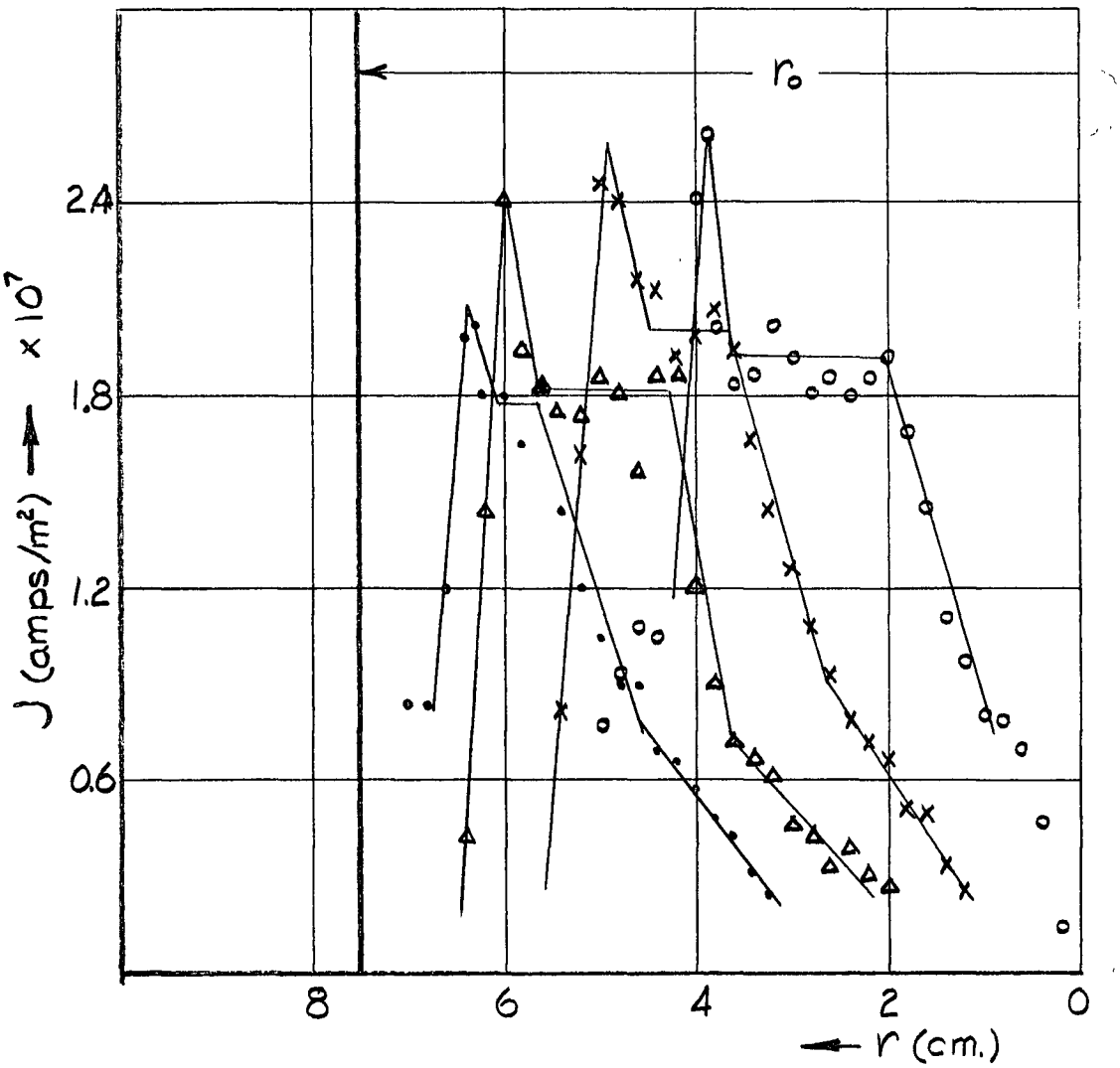

FIGURE 42. COMPUTED CURRENT DENSITY DISTRIBUTION

Initial Pressure: 500 μHg Argon
Time: 3 μsec •
4 μsec Δ
5 μsec ×
6 μsec o

8.2 COMPUTED RESULTS (CONT'D.)

A second interesting feature of the current distribution in the z-pinch discharge is the region of approximately constant current density which lies within the current sheet already mentioned. This region has appeared as only a slight irregularity in the results of previous investigators who have not corrected their results for the effect of the probe, (for example, see results quoted by Folkierski (1963)).

In Table III we summarize some of the data from figures 37. - 42. This information is required at a later stage of the investigation where we wish to know the velocity of the moving current density maximum and also the velocity of the leading edge of the plateau region. These results are plotted in figures 58. and 59., of section 10.0.

TABLE III

RADIAL POSITIONS OF ESSENTIAL CURRENT DENSITY FEATURES

R_o = Inner radius of discharge vessel
Rc = Radial position of current maximum
Rp = Radial position of leading edge of current plateau.

Pressure(μ Hg)	Time(μsec)	Rc(mm.)	Rp(mm.)	$Yc=Rc/Ro$	$Yp=Rp/Ro$
100	2 ± .3	62 ± 2	49 ± 2	.83 ± .03	.65 ± .03
	3	51	33	.68	.44
	4	30		.40	
250	2	65		.87	
	3	58	49	.77	.65
	4	49	36	.65	.48
	5	34	20	.45	.27
500	3	65	56	.87	.75
	4	60	45	.80	.60
	5	49	37	.65	.49
	6	39	21	.52	.28

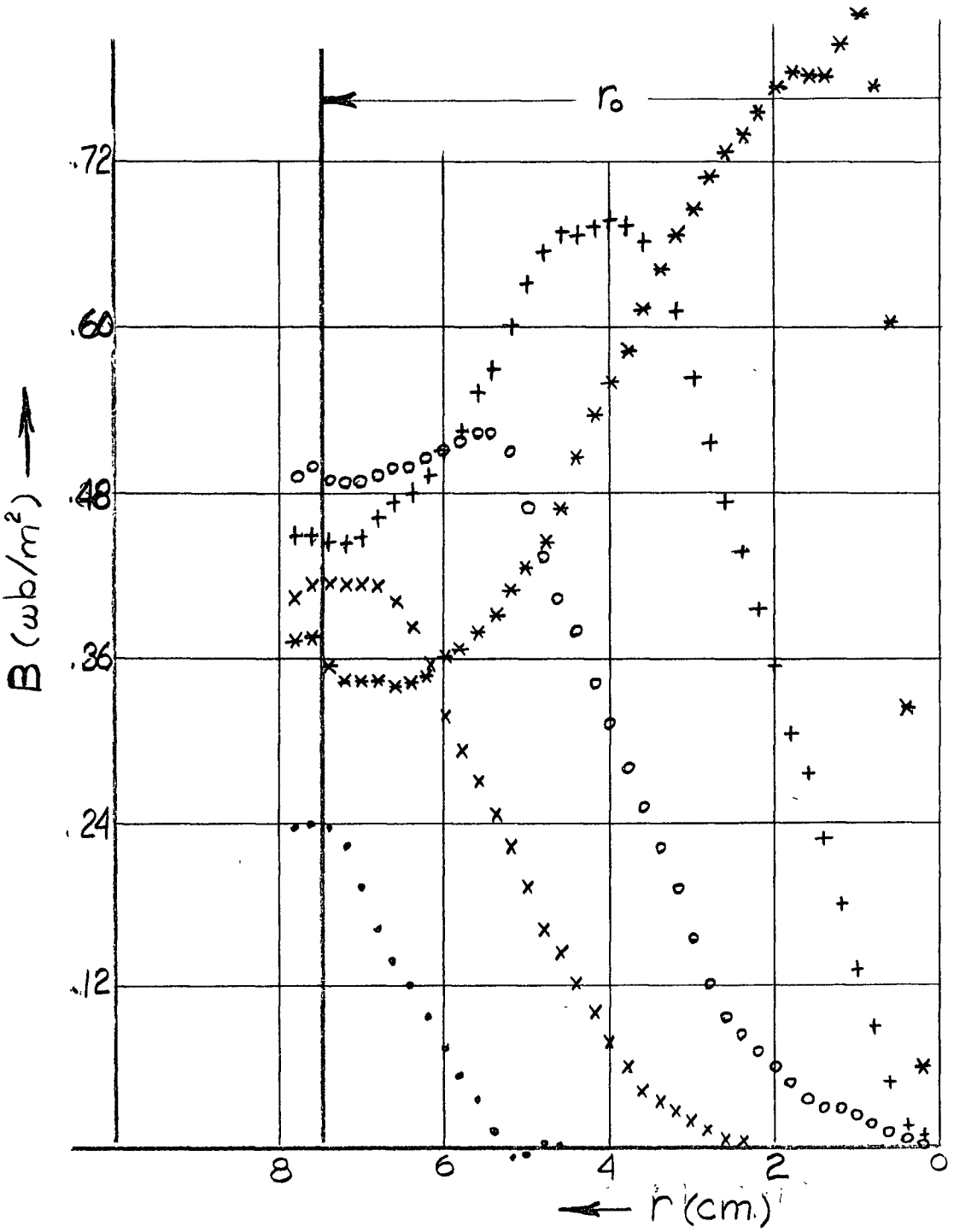

FIGURE 43. TRUE MAGNETIC FIELD DISTRIBUTION

Initial Pressure: 100 μHg Argon

Time:			
	1 μsec	•	4 μsec +
	2 μsec	x	5 μsec *
	3 μsec	o	

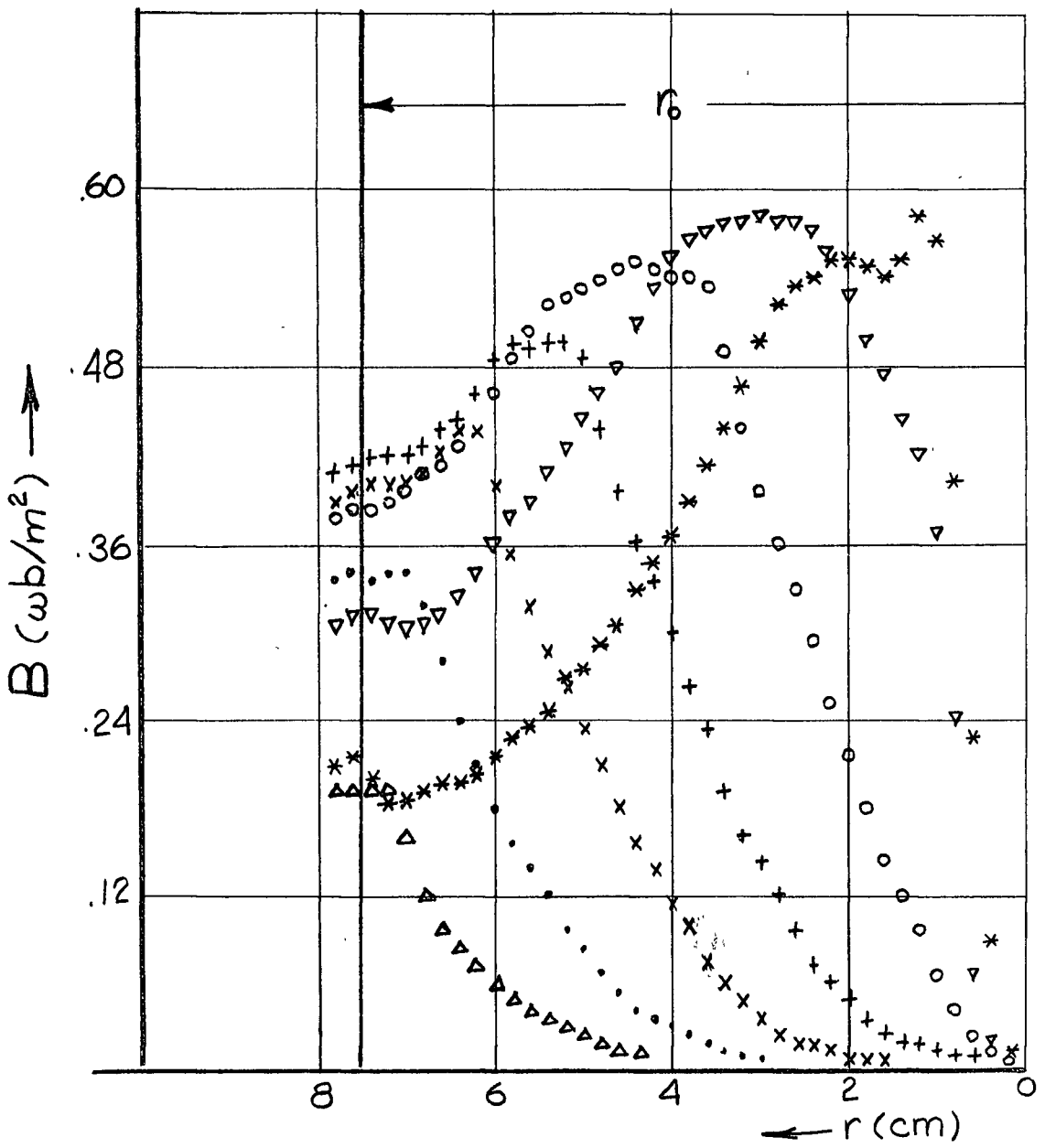

FIGURE 44. TRUE MAGNETIC FIELD DISTRIBUTION

Initial Pressure: 250 μHg Argon

Time:			
1 μsec	Δ	5 μsec	o
2 μsec	•	6 μsec	▽
3 μsec	x	7 μsec	*
4 μsec	+		

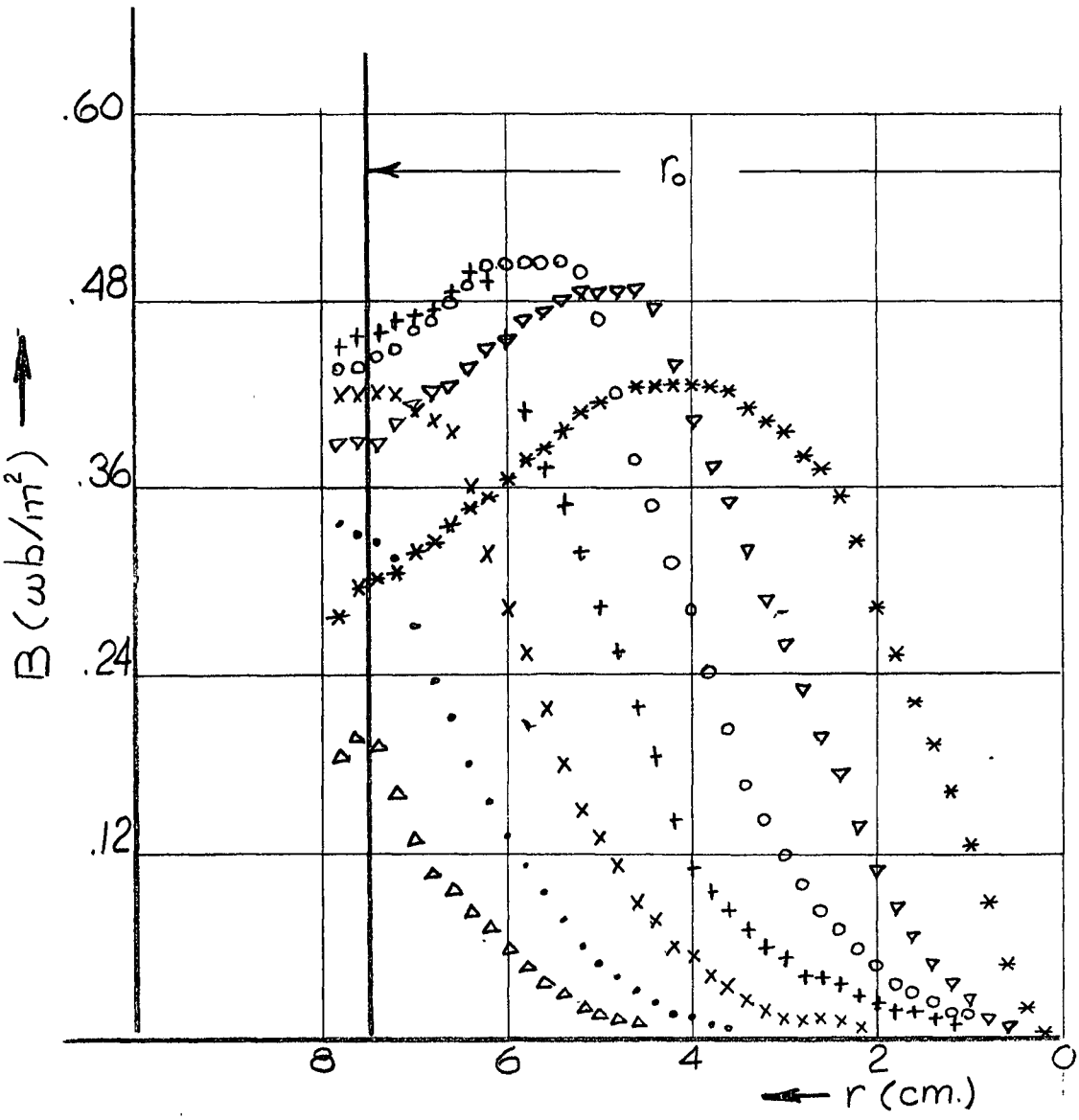

FIGURE 45. TRUE MAGNETIC FIELD DISTRIBUTION

Initial Pressure: 500 μHg

Time:			
1 μsec	Δ	5 μsec	o
2 μsec	•	6 μsec	▽
3 μsec	x	7 μsec	*
4 μsec	+		

8.2 COMPUTED RESULTS (CONT'D.)

Using Equation 2. (section 5.1) we determine the corrected magnetic field distributions corresponding to each of the measured magnetic field distributions of figures 31. - 33. These corrected magnetic field distributions are given in figures 43. - 45.

Finally in figure 46., we compare the measured magnetic field and corresponding current density with the corrected values. It is apparent that our correction procedure modifies the results appreciably. We must, therefore, examine all possible sources of error in order to determine that the calculated phenomena are real (eg. the appearance of a plateau region in the current density distribution). An analysis of error is given in the following section.

8.3 ANALYSIS OF ERROR

There are three, main, possible sources of error in our calculated values of the current density distribution. First, there are assumptions which are implicit when we apply our analogue results to the calculation of the current density and magnetic field in the z-pinch discharge. Secondly, it is possible that we make errors in measuring and in plotting the magnetic field distribution (section 8.0). And thirdly, it is possible that there are errors in our numerical calculations.

Analogue Error:

In using our analogue results for the z-pinch (see section 5.1)

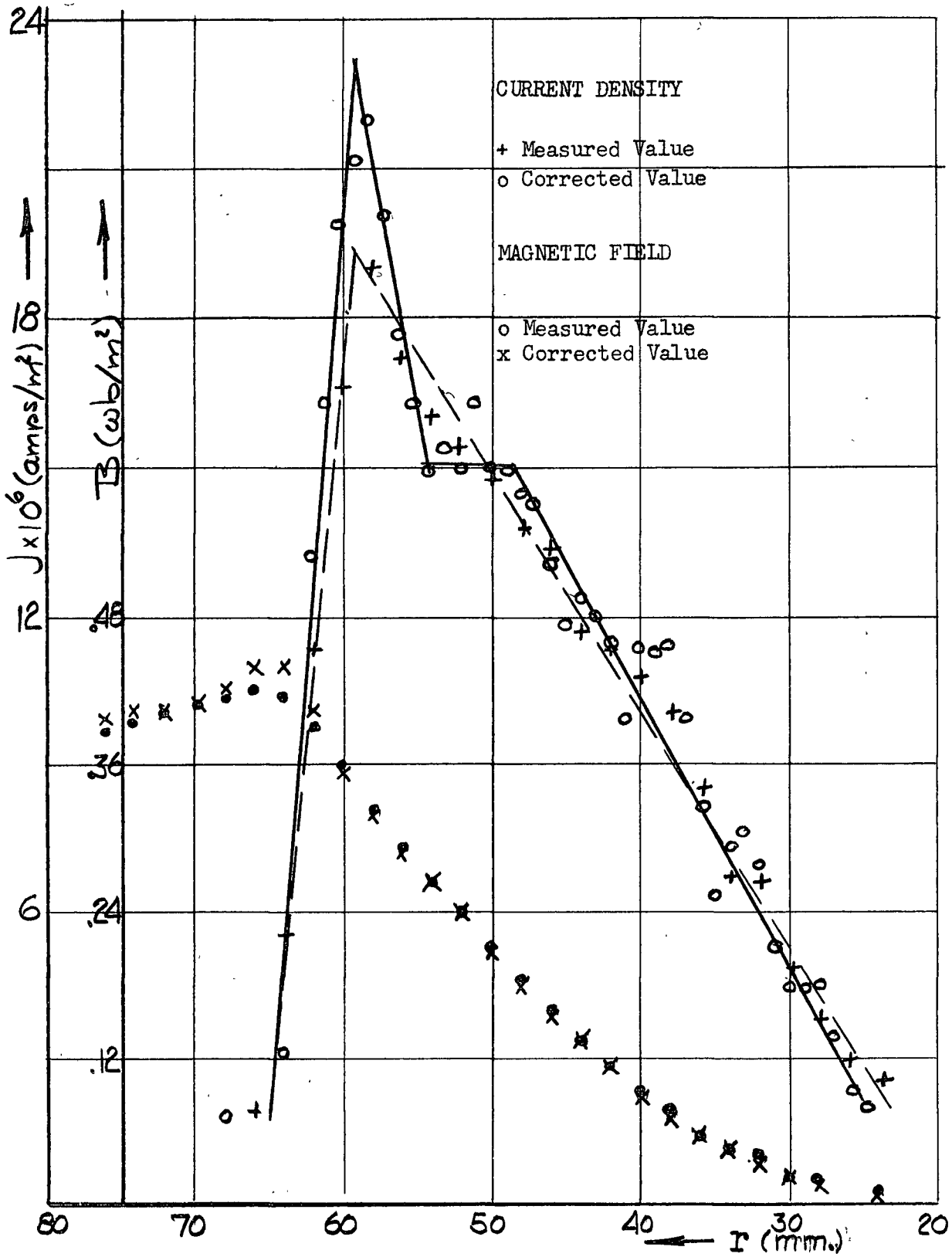

FIGURE 46. MEASURED AND CORRECTED CURRENT DENSITY AND MAGNETIC FIELD DISTRIBUTIONS

Time: 3 μsec
Initial Pressure: 250 μHg Argon

8.3 ANALYSIS OF ERROR (CONT'D.)

Analogue Error: (Cont'd.)

the most obvious assumption is that we can apply the results obtained from a single current sheet to the interpretation of measurement upon, effectively, many current sheets. Actually, we are assuming here that the correction is not affected by the conductivity of the surrounding media. In the analogue experiment a given current sheet is immersed in air of low conductivity, while in the actual experiment a given current sheet is immersed in plasma of high conductivity. However, we do have evidence from one experiment which shows that this assumption is reasonable.

In this experiment we have used the analogue experiment exactly as it has been described in section 4.1. We measure the perturbed magnetic field as a function of radius and then we repeat the experiment with the probe guide tube wrapped with aluminum foil as shown in figure 47. As the analogue experiment is performed with frequencies of the order of 10^6c/s, this aluminum foil simulates a region of high conductivity inside the current sheet and it restricts any magnetic flux which "drips in" through the probe hole in the current sheet to the region of the probe guide tube. The comparison of the measured magnetic fields in the vicinity of the current sheet is given in figure 47. and it is apparent that the conductivity of the surrounding media has a negligible effect.

Another major approximation or assumption which is implied in our using analogue results for plasma measurement is that the

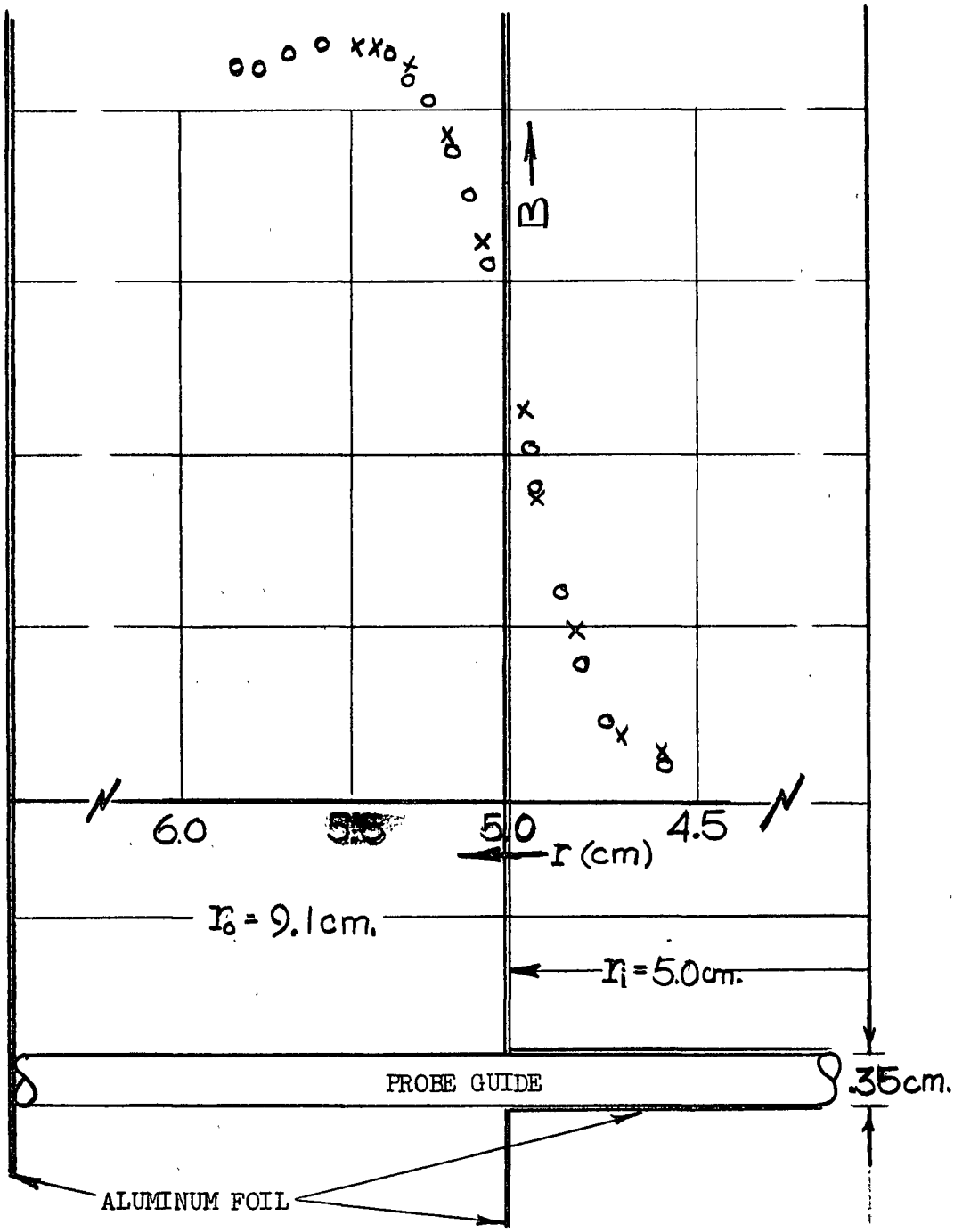

FIGURE 47. SIMULATED REGION OF HIGH CONDUCTIVITY

x Measured with aluminum foil around probe
o Measured without aluminum foil around probe.

8.3 ANALYSIS OF ERROR (CONT'D.)

Analogue Error: (Cont'd.)

redistribution of current in the plasma around the probe remains in the original plane of the sheet. This must occur in the analogue experiment but there is no reason why there might not be a three-dimensional redistribution of current in the plasma. Note that this effect would only be important where there is a discontinuity in the current distribution, as for example, at the position of a current density "spike" (refer to section 5.1). This effect introduces an error which can not be accounted for in our correction. Note, however, that this effect would tend to decrease the height of the measured current density spike, with some of the current appearing to flow in neighbouring current sheets. Hence this consideration reconfirms our knowledge that the height of a current spike observed by our measuring technique is a lower limit of the true height (see section 5.2).

If we do have a "three dimensional" perturbation of the current distribution, then it is very likely that appreciable plasma instabilities will occur. It is known that the collapsing plasma of the z-pinch discharge is unstable and a perturbation will grow if excited (see Hodgson (1964)). Again we can not account, in detail, for this effect in our correction procedure, but we can obtain a rough estimate of the limitations which it imposes on our results.

From a plot of the radial position of the current density spike versus time, we obtain a "collapse curve". A typical collapse curve

8.3 ANALYSIS OF ERROR (CONT'D.)

Analogue Error: (Cont'd.)

is shown in figure 48B. Now suppose the plasma is not axially symmetric but at a time $t = t_o$ we have a perturbation in the current sheet of magnitude Δr_o as shown in figure 48A. What happens to the magnitude of this perturbation as a function of time?

In figure 48B. we define a time Δt which it would take for the current sheet to constrict to the radius already reached by the perturbation. If Δt is fairly small, then we can assume that the radial force acting on the current sheet does not change appreciably in a time Δt. Thus the radius of the current sheet at the perturbation will follow a second trajectory which is identical to the trajectory of the normal collapse curve but displaced in time by an amount Δt. These trajectories are shown in figure 48B. That the perturbation results in an instability is apparent from an examination of $\Delta r(t)$, the distance between the two collapse curves. It is observed that $\Delta r(t)$ increases with time, i.e. the perturbation grows. Note, however, that the perturbation grows very slowly during the earlier stages of the collapse, but the growth is rapid at times approaching the pinch time tp (see figure 48B.).

Thus the most reliable measurements of the current density are made during the early stages of the collapse where any perturbations have not grown appreciably. However, at times close to the pinch

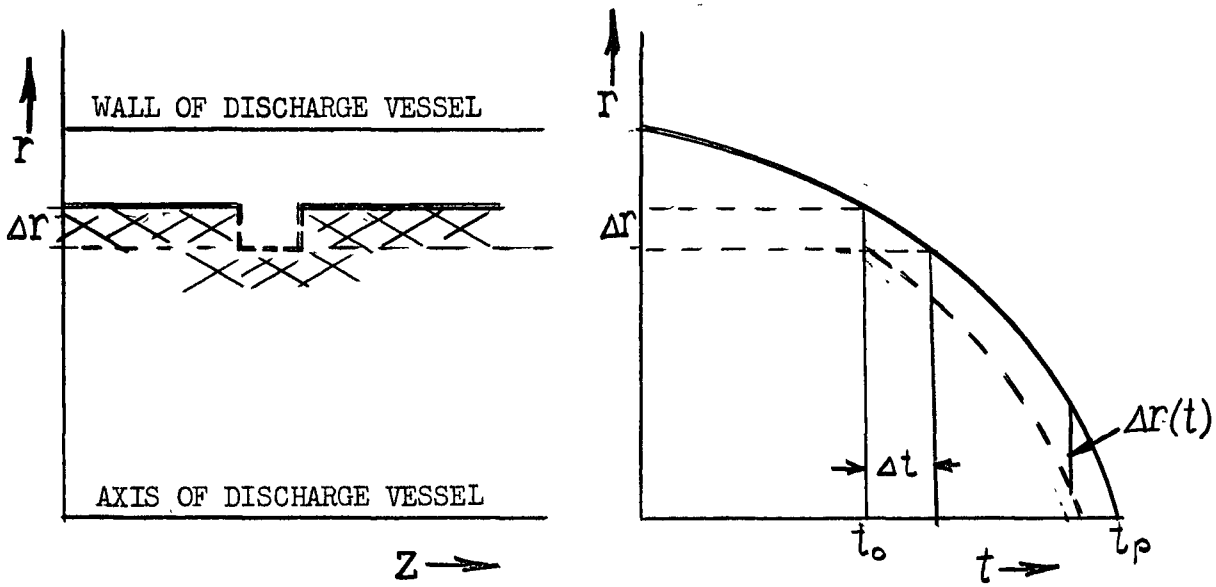

FIGURE 48. PLASMA INSTABILITY

——— Normal plasma boundary
— — Position of perturbation

8.3 ANALYSIS OF ERROR (CONT'D.)

Analogue Error: (Cont'd.)

time these instabilities could affect appreciably the measured current distribution and our information for these times is unreliable.

Measuring Errors:

The second source of error which has been mentioned at the beginning of this section is the error associated with the measurement of the magnetic field. The oscilloscope traces have been recorded on polaroid film (see figure 27.) and then measured with the aid of a grid. The grid, which has a spacing equal to the smallest gradicule spacing, is ruled on perspex and can be placed

8.3 ANALYSIS OF ERROR (CONT'D.)

Measuring Errors: (Cont'd.)

over the polaroid film. The reading error is approximately $\pm$ .2 of the smallest division.

There is also an error in the measurement of the magnetic field from two different discharge shots which is due to the variation of the charging voltage on the capacitors. This causes a 2 - 3% error in the magnetic field. "Error flags" corresponding to these errors are shown on the magnetic field distributions of figures 31. - 33.

What is the effect of this measuring error in the magnetic field upon the computed current density?

Since,

$$\mu_o J(r) = \frac{1}{r} \frac{\partial}{\partial r} rB(r) = \frac{B(r)}{r} + \frac{\partial B(r)}{\partial r}$$

we see that the current density is affected by both error in the magnetic field and error in the gradient of the magnetic field. Actually, the gradient term is usually dominant and the error associated with this term may be very large. For example, near the peak of the magnetic field distribution curves where there are few experimental points to determine the rapidly changing gradient, the error may be as large as 50%.

We conclude this discussion of measuring error with figure 49. which illustrates the correlation of the characteristic features of typical magnetic field and current density distributions. At the peak of the magnetic field distribution we expect large error in the corresponding current density. However, for radial positions inside

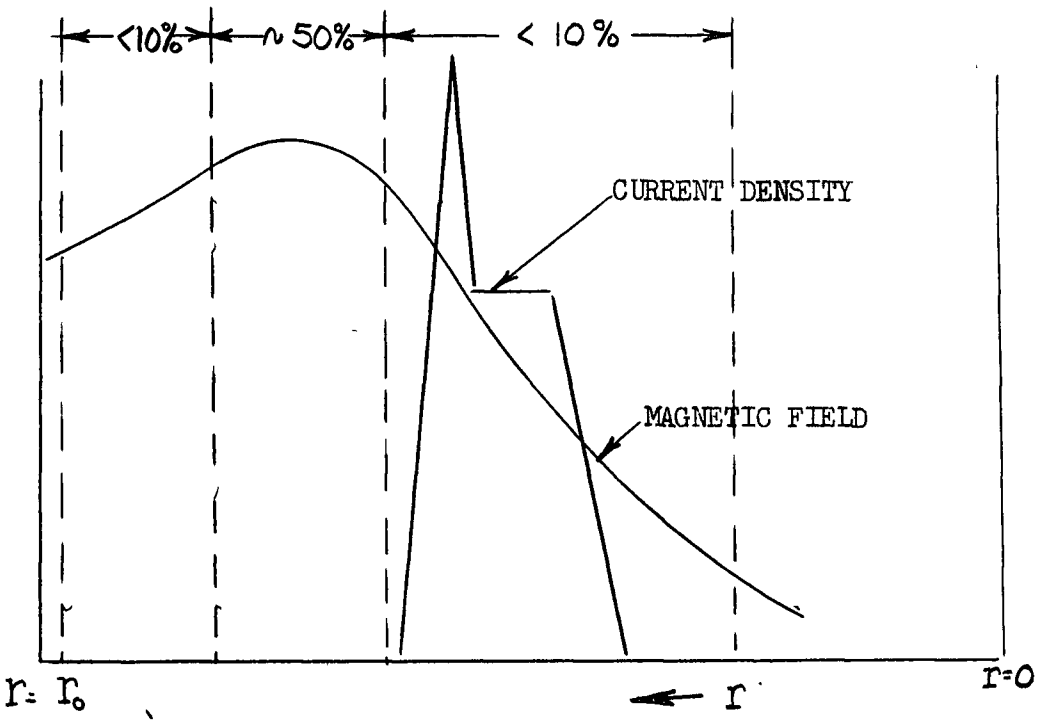

FIGURE 49. ESTIMATED ERROR IN "J" DUE TO ERROR IN "B"

8.3 ANALYSIS OF ERROR (CONT'D.)

Measuring Errors: (Cont'd.)

and outside this peak we have a well established field gradient and the corresponding current densities have errors of less than 10%. Fortunately, the interesting regions of the current density distribution coincide with the regions of greater accuracy. It is apparent from figure 49. that we can not make meaningful measurements of the current density in the region which is just outside the current density peak.

8.3 ANALYSIS OF ERROR (CONT'D.)

TABLE IV

COMPARISON OF COMPUTED CURRENT DENSITY FROM TWO MEASUREMENTS OF MAGNETIC FIELD

(500 μHg argon - 7 μsec)

RADIUS	MAGNETIC FIELD			FIELD GRADIENT			CURRENT DENSITY		
	1	2	%	1	2	%	1	2	%
15	2.80	2.67	4	-	-	-	17.4	16.1	-
	3.00	2.89	4	.20	.20	0	17.2	16.2	0
	3.21	3.08	4	.20	.19	5	16.1	16.4	2
	3.40	3.28	3	.18	.20	10	16.1	15.2	6
	3.58	3.48	3	.17	.20	15	14.6	16.5	12
20	3.74	3.69	1	.17	.21	20	15.0	17.2	14
	3.92	3.90	0	.17	.20	15	14.9	17.6	18
	4.08	4.10	0	.14	.20	30	14.2	17.8	24
	4.21	4.30	2	.14	.17	23	14.1	15.9	12
	4.37	4.45	2	.14	.15	7	13.4	14.9	10
25	4.50	4.60	2	.12	.13	8	13.2	12.1	6
	4.61	4.71	2	.11	.10	9	11.5	11.5	0
	4.72	4.81	2	.11	.09	18	11.3	10.2	10
	4.83	4.90	1	.10	.09	10	11.5	10.6	9
	4.93	4.99	1	.09	.09	0	11.1	11.2	1
30	5.02	5.08	1	-	-	-	10.7	10.4	3

Numerical Error:

In order to check that the numerical results do not include more error than we have already discussed, we perform the following test. We plot two possible curves through the measured values of magnetic field (B) plotted against radius (r) for a given distribution (actually 500 μHg at 7 μsec) and we calculate the corresponding values of the current density (J).

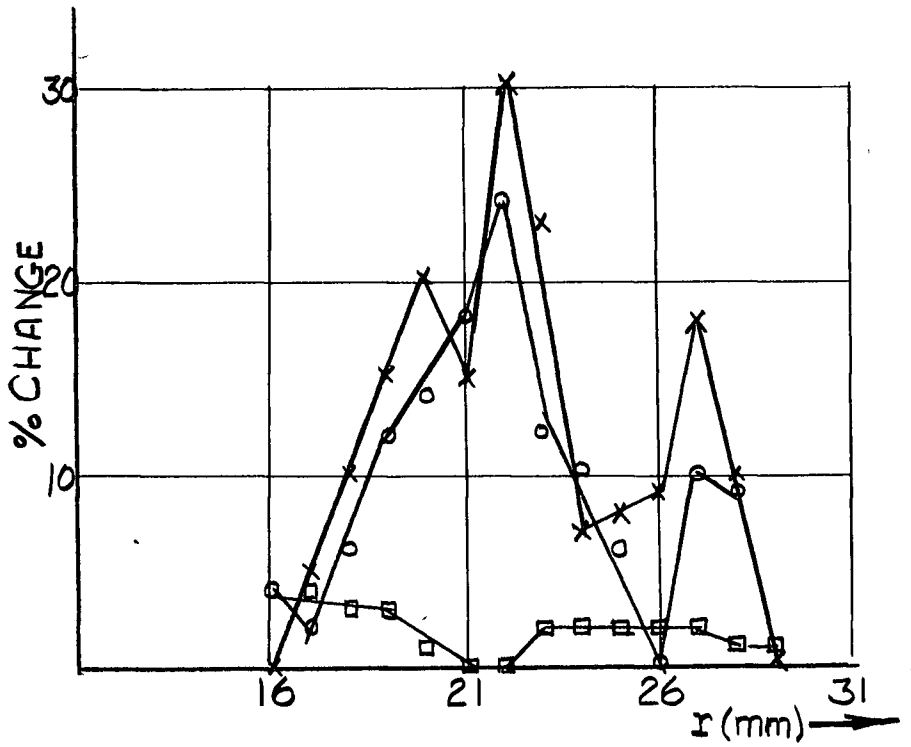

FIGURE 50. DEPENDENCE OF CURRENT DENSITY UPON MAGNETIC FIELD GRADIENT

□ Variation in magnetic field
× Variation in magnetic field gradient
o Variation in computed current density.

8.3 ANALYSIS OF ERROR (CONT'D.)

Numerical Error: (Cont'd.)

The comparison of the two calculations may be observed in Table IV or from the plot of percentage change in the magnetic field, the magnetic field gradient, and the current density versus radial position as given in figure 50. From this figure, it is obvious that the variation in the computed current density is proportional to the variation in the gradient of the magnetic field and not to the variation in the field itself. Since the variation in the current density is of the order of or less than the variation in the field gradient, we can assume that the numerical computation does not introduce any further error. Note, though, that we have

8.3 ANALYSIS OF ERROR (CONT'D.)

Numerical Error: (Cont'd.)

seen in section 5.2 that considerable errors are introduced by the numerical approximation to the measured magnetic field and correction (see figure 17.(pge.45)) curves. This latter error, however, is only appreciable at regions where the current density distribution is discontinuous.

9.0 PHOTOGRAPHIC MEASUREMENT

The reason for introducing photographic measurement in this investigation is two fold. First we wish to examine optically the perturbation of plasma by the magnetic probe. In particular, we wish to obtain an estimate of the "effective" probe radius which has already been discussed in section 3.2. Secondly, we wish to have some independent method of examining the plasma in order to aid in the interpretation of our magnetic probe measurements. Curzon (1962) and Folkierski (1963) have used the same type of high speed framing camera which we have described in section 7.0.

Measurement with a camera obviously does not perturb the plasma as the magnetic probe does, but we still must recognize limitations when we interpret the photographic results. For example, when we plot the collapse curves of section 9.2 with points obtained from the photographs, we are assuming that the luminous region of the discharge coincides with the region of high current density. Curzon (1963) had reason to question this assumption. The radial position of the radiating ions and neutrals does not necessarily

coincide with the radial position of the electron current flow. We will examine this effect.

A second source of error is apparent when determining the radius of the luminous boundary of the films (see figure 53.). The boundary is diffuse and may even be a function of exposure or developing time. A sharp boundary may also appear diffuse because of so called "smearing error". If the plasma velocity is very high, and the exposure time is not correspondingly small then the image on the film will be "blurred" or "smeared" and the boundary will appear diffuse. This reading error is the source of the error which is estimated on the collapse curves of figure 54.

All photographs are obtained on Ilford H.P.3 film. The film is developed in Ilford ID-2 developer for approximately twelve minutes and fixed in Amfix for approximately six minutes.

9.1 MAGNETIC PROBE PERTURBATION

We can use the framing camera to investigate the perturbation of the discharge plasma which is caused by the magnetic probe. Two particular aspects of this phenomenon are examined. First, we line the camera up with the axis of the magnetic probe guide tube and we obtain so called "side-on" photographs (see figure 51.). These photographs are examined for any variation in light intensity from the region surrounding the probe. Such a variation would be explained by the "conductivity error" which has been discussed in

Photograph on the left hand side of following page

FIGURE 51. SIDE-ON PHOTOGRAPH OF DISCHARGE

Film strip corresponding to first 3 μsec of 100 μHg discharge
Probe guide tube appears as light circle in centre square
Time sequence zigzags - .23 μsec between frames
Time increases from bottom to top of page.
Cathode is at right.

Photograph on the right hand side of following page

FIGURE 52. TOP-ON PHOTOGRAPH OF DISCHARGE

Film strip corresponding to first 3 μsec of 100 μHg discharge
Probe guide tube appears as horizontal dark bar
Time sequence zigzags - .23 μsec between frames
Time increases from bottom to top of page
Cathode is at top.

section 3.2 and thus we could obtain an estimate of the effective probe radius.

An examination of figure 51. reveals a strong perturbation of the initial axial current flow. Characteristic "Mach lines" are observed and these reverse when the polarity of the discharge electrodes is reversed. However, once the discharge plasma is fully developed and it begins to constrict, there is no variation in the luminosity about the probe. For this reason, we have used the actual radius of the quartz guide tube in the calculations for magnetic field correction (see section 8.2) where an estimate of the effective probe radius is required.

The second examination of the magnetic probe perturbation is accomplished with "top-on" photography of the discharge. In this case the camera is in line with the axis of the discharge vessel, but it is directed toward a mirror above the discharge which gives an image of the probe (see figure 52.) The purpose of this photograph is to investigate any three dimensional perturbation of the discharge current around the probe. We have discussed this possibility in section 8.3 and we expect that if this perturbation does exist, its growth rate will be small in the early stages of the collapse.

Figures 51. and 52., are both obtained during the initial stages of a discharge formed in an initial gas pressure of 100 μHg argon. Again the Mach lines are obvious, but observe that they

9.1 MAGNETIC PROBE PERTURBATION (CONT'D.)

occur at specific radial points - not all along the length of the probe. The anticipated effects of three dimensional perturbation by the probe (see section 8.3) are also observed in figure 52. The constriction at the probe is particularly obvious in the last frames. The perturbation effect is largest at low pressures because of the higher plasma acceleration. For 100 μHg the effect is appreciable when the plasma column is as large as 4 cm. radius. In general, our probe measurement will not be reliable when the radius of the plasma column is small (say, less than 2 cm.).

9.2 COLLAPSE CURVES

A collapse curve is a plot of the diameter of the luminous plasma as a function of time. In figure 54. we have plotted the collapse curve for each of the three initial pressures of the discharge gas which have been used throughout these investigations.

To obtain these measurements, the film images, which are approximately 8 mm. square, are magnified ten times with the optical system of a Jarrell-Ash microdensitometer. The magnified image is viewed on a ground glass screen and the diameter of the plasma column can be measured with an ordinary rule. A typical image is reproduced in figure 53.

Scaling factors are avoided by taking all measurements relative to the inner diameter (d_o) of the discharge vessel. By measuring the diameter (d) of the luminous plasma, we obtain the dimensionless diameter (or radius) y defined as d/d_o.

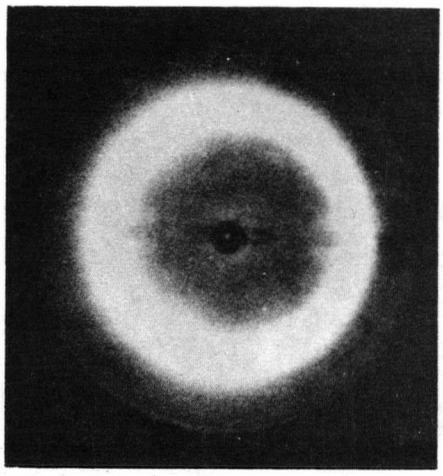

FIGURE 53. END-ON PHOTOGRAPH OF DISCHARGE

Initial pressure 500 μHg argon
Time of photograph is 4 μsec after initiation of discharge current
Probe guide tube is horizontal
Black circle is on brass electrode.

9.3 SHOCK VELOCITY MEASUREMENT

When the plasma current collapses toward the axis, it forms a piston which sweeps up the gas before it. If the piston moves much more rapidly than the speed of sound in the medium then we have the formation of a strong shock front. In our experiment, the piston velocity is approximately 10^4 m/sec, or about 40 times the speed of sound. A strong shock front is characterized by a sharp discontinuity in density and temperature and hence it should be readily observed experimentally.

Graph on page 111.

FIGURE 54A. COLLAPSE CURVES

○ Outer luminous boundary for 100 μHg argon
● Inner luminous boundary for 100 μHg argon
△ Outer luminous boundary for 500 μHg argon
▲ Inner luminous boundary for 500 μHg argon

Graph on page 112.

FIGURE 54B. COLLAPSE CURVE

× Outer luminous boundary for 250 μHg argon
+ Inner luminous boundary for 250 μHg argon.

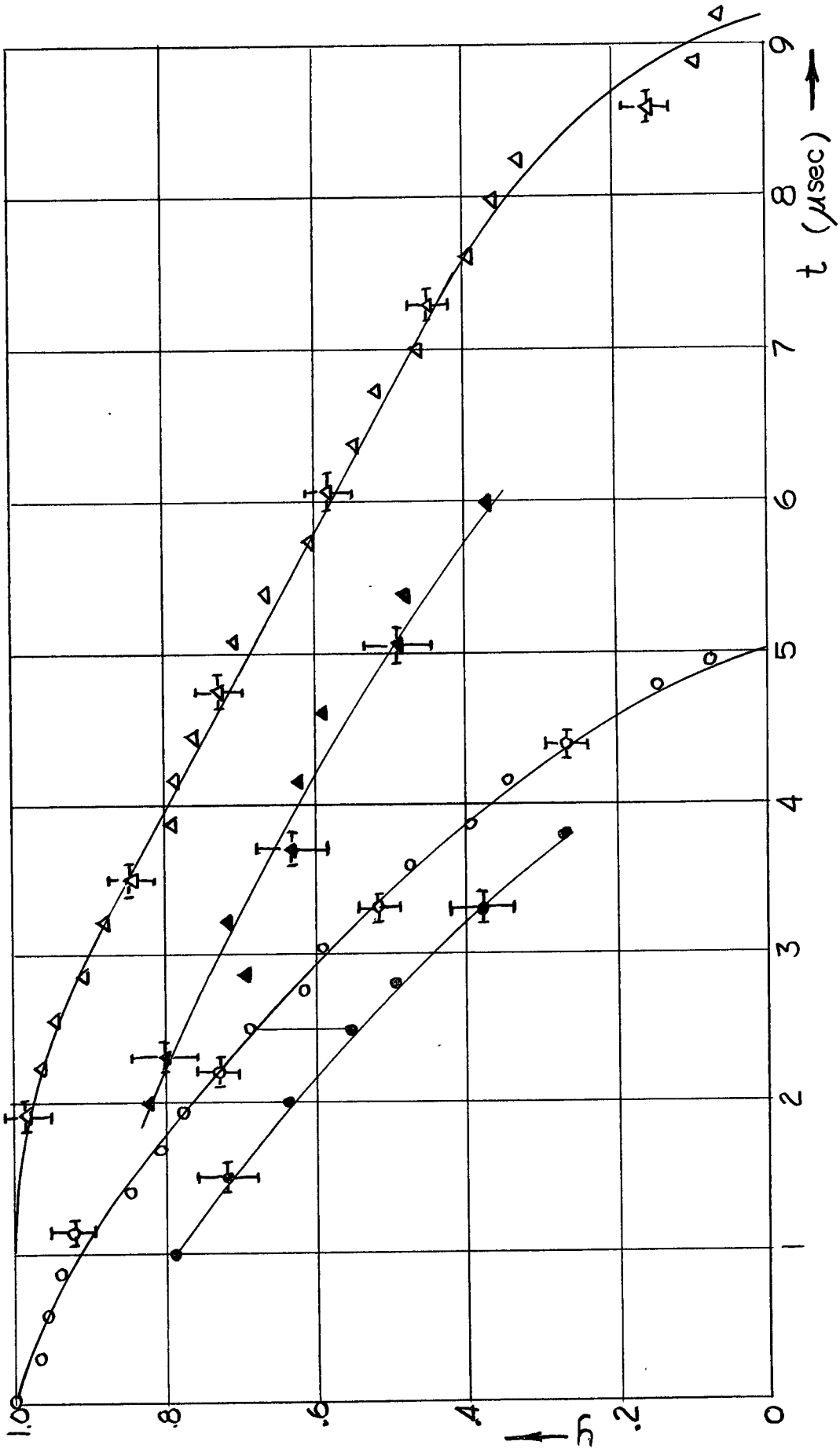
1.0
.8
.6
.4
.2
0
y
1
2
3
4
5
6
7
8
9
t (μsec)

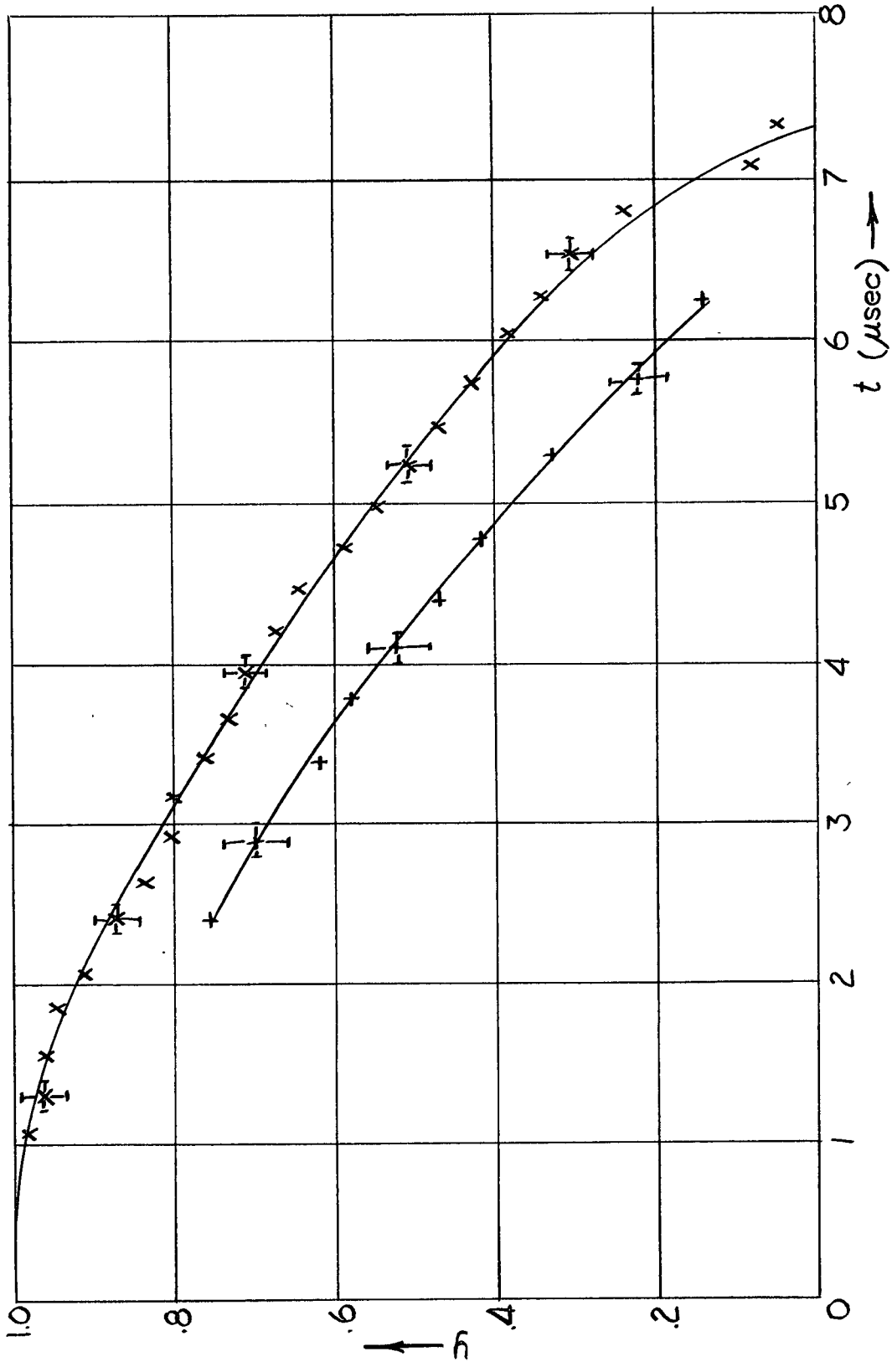
1.0
.8
.6
.4
.2
0
y
0
1
2
3
4
5
6
7
8
t (μsec)

9.3 SHOCK VELOCITY MEASUREMENT (CONT'D.)

A technique for observing shock fronts in the z-pinch discharge and for measuring their velocity of propagation has been reported by Folkierski (1963). It is possible that the plateau region of the current density distributions may represent a shock heated plasma and we wish to find the position of the shock front relative to the plateau region.

Folkierski's technique is based upon the fact that a reflected shock wave is usually luminous due to the increase in enthalpy of the gas at the point of reflection. Cylindrical baffles are placed in the discharge vessel and photographs reveal the times at which the shock front strikes the baffles. A typical example as given in figure 55. shows the frames from the photograph which illustrate the arrival of the shock front. Four cylindrical baffles of approximately 2-3 cm. in length and of diameters 6.0, 7.8, 8.8, and 9.8, are used, in turn, in the discharge. The cylinders are mounted individually on a glass rods which lies along the discharge axis. The glass rod is supported by a fitting in the brass electrode which places the cylinders approximately 15 - 20 cm. from the electrode.

The glass cylinder obviously perturbs the plasma once the current sheet reaches the cylinder and measurements (such as pinch time) are unreliable at times following this interaction. We assume that the flow is undisturbed for the time preceding the interaction, but even this assumption appears doubtful. A careful

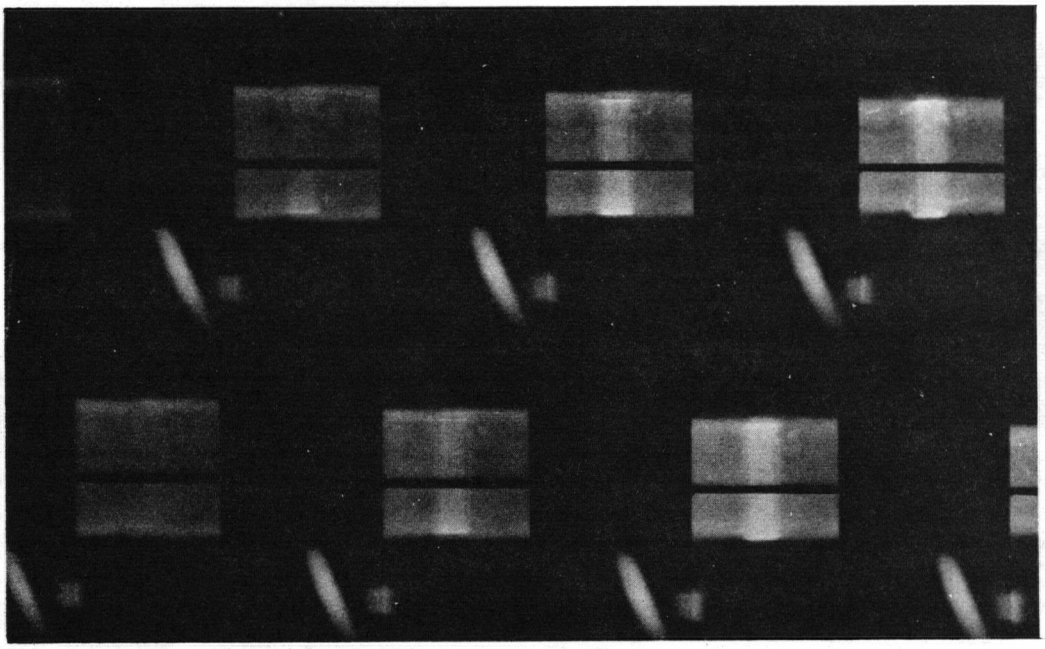

FIGURE 55. RADIAL POSITION OF SHOCK FRONT

Top-on photographs.
Time sequence zigzags. Time increases from left to right.
Initial pressure = 500 μ Hg argon
Baffle diameter = 8.8 cm.
Time between frames = .24 μ sec.
Surface of cylindrical baffle corresponds to brightest region.
Baffle is approximately 2 cm. long, with axis horizontal.

9.3 SHOCK VELOCITY MEASUREMENT (CONT'D.)

examination of figure 55. shows that the current sheet appears to constrict more rapidly in the region of the cylindrical baffle.

A sequence of photographs is taken for each cylinder with each of the three initial pressures. The results are presented in Table V. and plotted later in figure 58.

9.3 SHOCK VELOCITY MEASUREMENT (CONT'D.)

PRESSURE (μHg)	D (cm.)	Y	T_E (μsec)	N ± 1	T (μsec) ± .3
100	9.8	.65	.26	9	2.3
	8.8	.59	.26	9	2.3
	7.8	.52	.275	12	3.3
	6.0	.40	.29	13	3.8
	6.0	.40	.275	14.5	4.0
250	9.8	.65	.295	11	3.2
	8.8	.59	.27	12.5	3.4
	7.8	.52	.27	14.5	3.9
	6.0	.40	.26	20	5.2
	6.0	.40	.25	20	5.0
500	8.8	.59	.26	17.5	4.6
	7.8	.52	.28	17.5	4.9
	6.0	.40	.26	24	6.2

TABLE V.

POSITION OF SHOCK FRONT

D = Diameter of baffle
Y = Dimension less diameter corresponding to D
T_E = Time between frames on photographic film
N = Number of frames between initiation of discharge and illumination of baffle
T = Time for shock front to reach given position Y

10.0 COMPARISON OF MAGNETIC PROBE AND FRAMING CAMERA RESULTS

One of the purposes of the photographic investigation is to correlate the visible features of the discharge with the current density distribution. But to do this, we must first know how times measured on the oscilloscope traces correlate with times measured on the photographic films. We have no reference point which is common to both. If, however, we could show that the initiation of luminosity and the initiation of the discharge

current are simultaneous, then we would have the required reference point. To verify this simultaneity we perform the following experiment.

In this experiment, we must trigger the oscilloscope from the Rogowski coil, i.e. from the break down of the discharge gas, as this is the mode of triggering which has been used for all previous experiments. Also, we must trigger the discharge itself from the photo multiplier of the framing camera if we wish to obtain photographs of the discharge.

With these triggering arrangements we wish to obtain some reference signal on the oscilloscope trace which coincides with a known time on the film. The most obvious reference signal is the pulse from the photo multiplier which immediately precedes the first lens of the framing camera (see figure 23.). However, this pulse is also used to trigger the discharge and as there is a delay between triggering and break down of the discharge (called the formative time delay (t_F)), this signal occurs <u>before</u> the oscilloscope is triggered.

This problem is solved by placing a known time delay (t_D) in the signal lead between the photo multiplier of the framing camera and the oscilloscope. If the time delay (t_D) is greater than the formative time delay (t_F), then the photo multiplier pulse will appear on the oscilloscope trace at a time t_o as shown in figure 56.

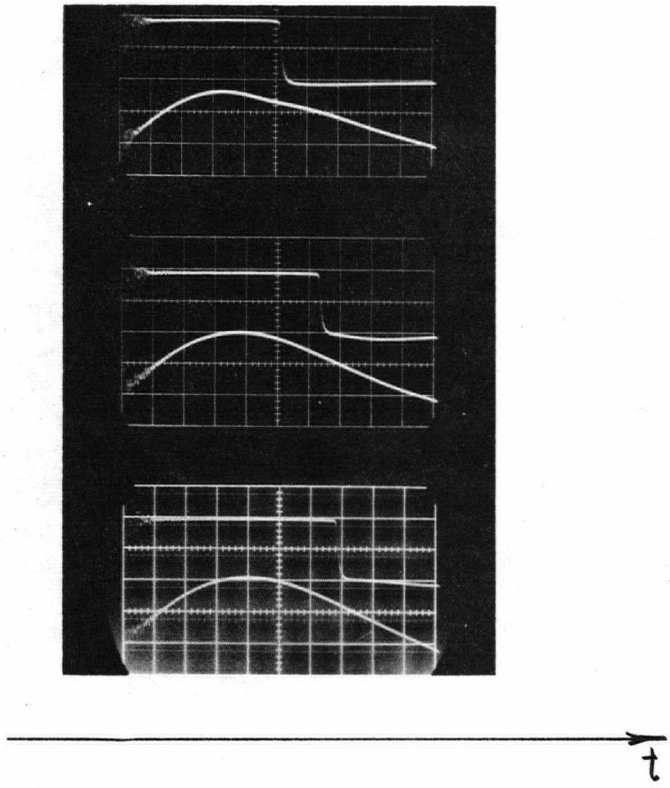

FIGURE 56. MEASUREMENT OF FORMATIVE TIME DELAY

Upper trace: Trigger pulse delayed by 8.9 μsec (20 volts/cm.)
Lower trace: Discharge current (75 kamp/cm.)

Time base: .95 μsec/cm.
Top: 100 μHg argon
Middle: 250 μHg argon
Bottom: 500 μHg argon.

10.0 COMPARISON OF MAGNETIC PROBE AND FRAMING CAMERA RESULTS (CONT'D.)

Furthermore, we measure t_o from the oscilloscope trace and thus determine the formative time delay,

$$t_F = t_D - t_o$$

On the corresponding photographic films we count the number

of frames which have passed between the triggering of the discharge and the initiation of luminosity. Since we know the time between photographic frames from the monitored period of the mirror rotation (see section 7.0), then we have another value for the formative time lag. If these two values are the same, then we know that the initiation of discharge current and luminosity coincide.

In figure 56, we present oscilloscope traces which show the position of the delayed pulse (upper beam) relative to the discharge current (lower beam) for each of the three initial gas pressures. The formative time delay obtained from this photograph is entered in Table VI.

PRESSURE (μHg)	NO. FRAMES	T (μsec)	T_{FL} (μsec)	T_{FC} (μsec)	ΔT_F (μsec)
100	14	.26	3.64	3.48	.16
250	11	.26	2.86	2.64	.22
500	8	.315	2.52	2.20	.32

TABLE VI

COINCIDENCE OF INITIATION OF DISCHARGE CURRENT AND LUMINOSITY

T = Time between film frames
T_{FL} = Formative time delay as measured to initiation of discharge luminosity
T_{FC} = Formative time delay as measured to initiation of discharge current
$\Delta T_F = T_{FL} - T_{FC}$

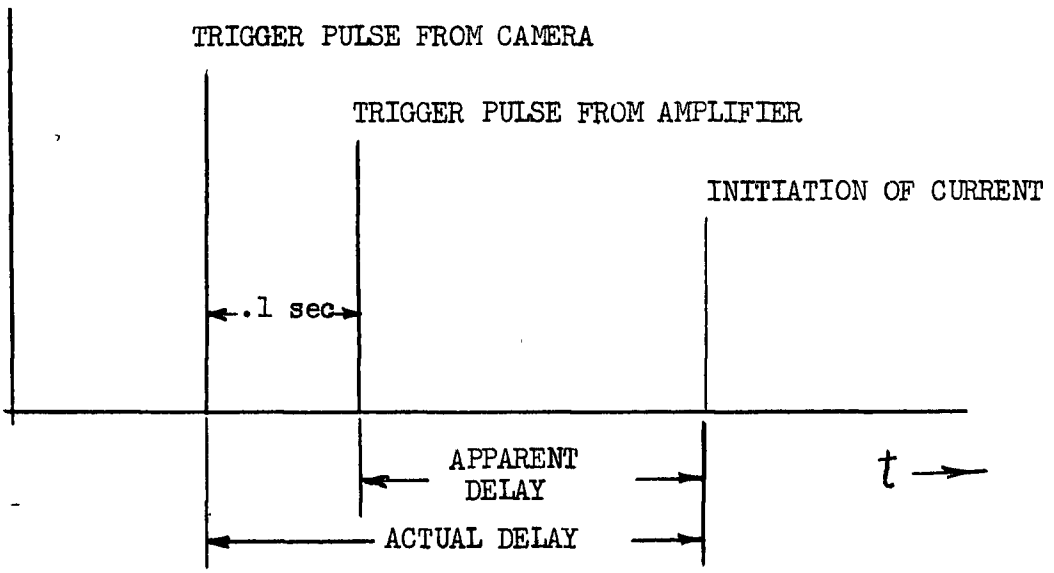

FIGURE 57. EFFECT OF AMPLIFIER DELAY

10.0 COMPARISON OF MAGNETIC PROBE AND FRAMING CAMERA RESULTS (CONT'D.)

Table VI also includes the value obtained from the photographic films. The comparison shows that the initiation of discharge current and luminosity are coincident within our experimental error of $\pm$ .25 μsec.

There is a measuring error in determining the number of frames preceding luminescence. This error is approximately $\pm$ 1 frame which corresponds to approximately $\pm$ .25 μsec. Also, there is a slight delay ($\sim$.1 μsec) in the amplifier which is between the photo multiplier and the trigger pulse. This will give an apparent formative delay from the current measurement which is approximately .1 μsec too short (see figure 57.)

10.1 DETERMINATION OF SHOCK AND FLOW VELOCITIES

Having obtained the desired reference time for the film and oscilloscope trace, we wish to make two comparisons between the features of the luminous plasma and those of the current density distribution. First, we wish to compare the position of the shock front with the position of the inner edge of the current density plateau as functions of time. Second, we wish to compare the position of the outer edge of the luminous plasma with the position of the peak current density - again as functions of time.

In figure 58. we have plotted the position of the shock front as a function of time from the data of Table V (section 9.3). The position of the inner edge of the current density plateau is obtained from Table III (section 8.2). For all three initial gas pressures it is apparent that the position of the shock front and the inner edge of the current density plateau are coincident within our experimental error of $\pm$ .25 cm.

In figure 58. we have also included the position of the inner edge of the luminous plasma as determined from the collapse curves of figure 54. Within our experimental error, this inner edge coincides with the position of the shock front.

In figure 59. we have plotted the positions of the current peak (again obtained from Table III) with the positions of the outer edge of the luminous plasma (as given in figure 54.) as functions of time. Within our experimental error of $\pm$ .25 cm., it is apparent that the outer edge of the luminous plasma does coincide with the position of

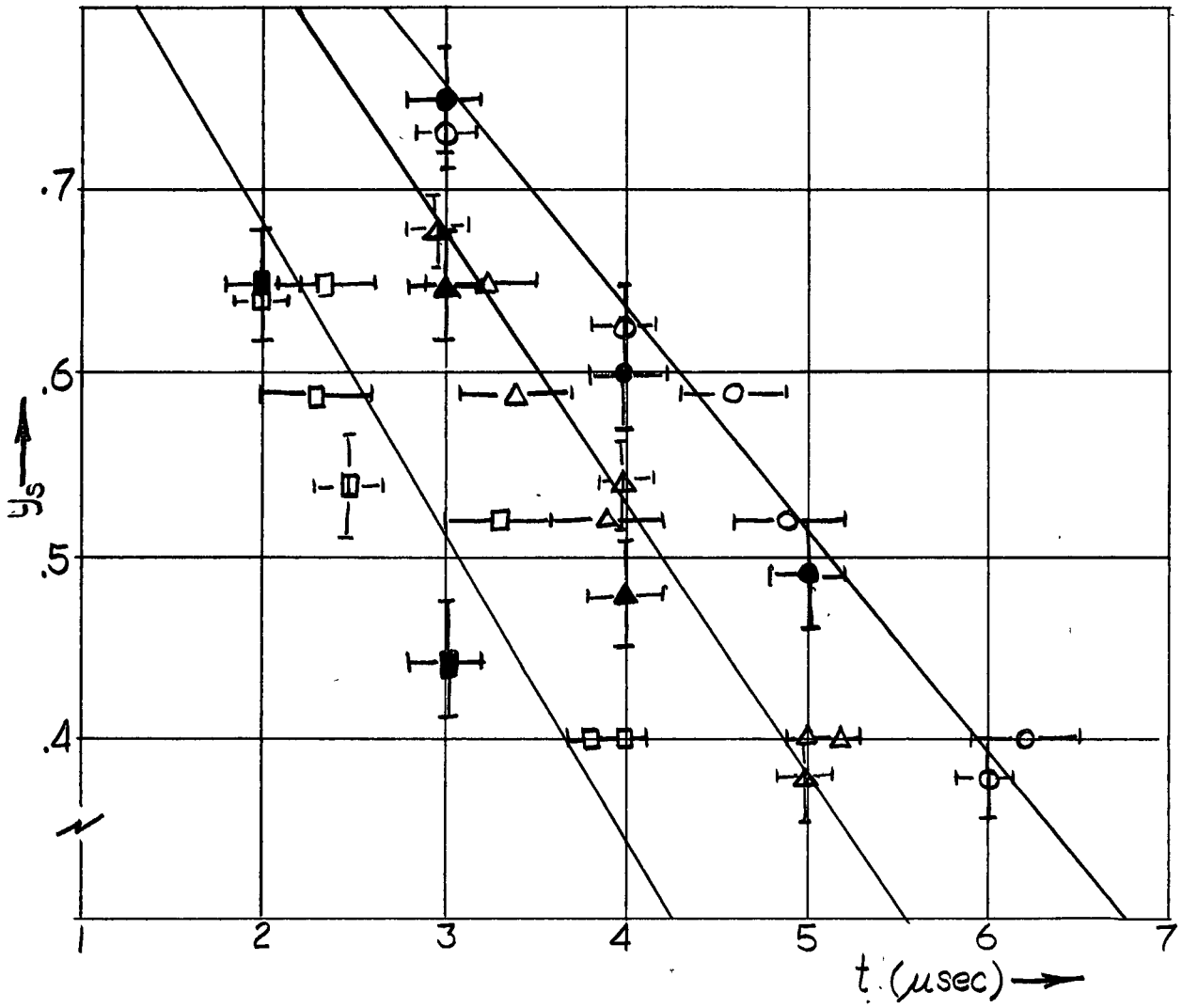

FIGURE 58. SHOCK FRONT (y_s) VS. TIME

Magnetic Probe Results (section 8.2)
- ▯ 100 μHg Argon
- ⧋ 250 μHg Argon
- ⊕ 500 μHg Argon

Photographic Results (section 9.2)
- □ 100 μHg Argon
- △ 250 μHg Argon
- ○ 500 μHg Argon

Photographic Results (section 9.3)
- ■ 100 μHg Argon
- ▲ 250 μHg Argon
- ● 500 μHg Argon

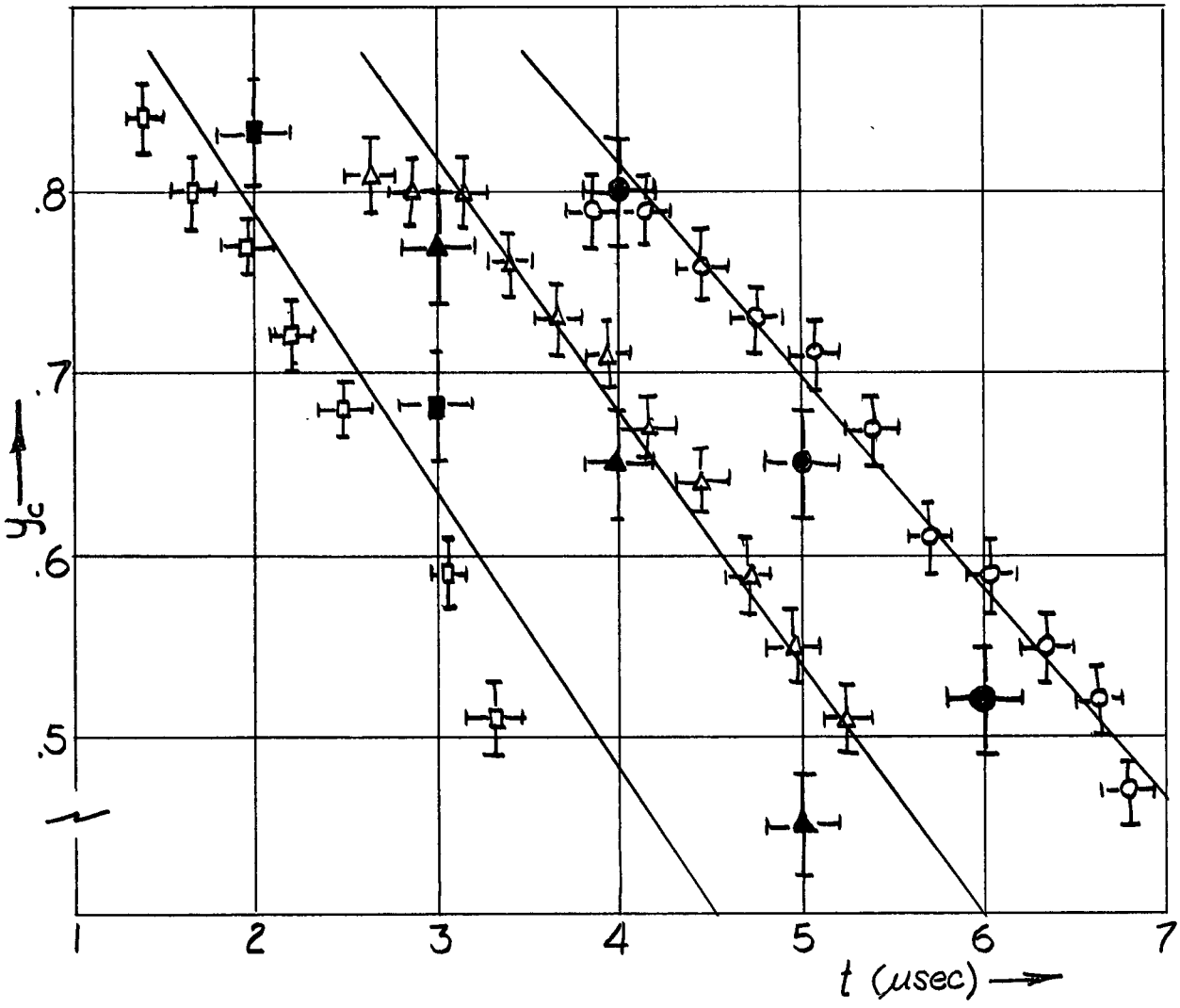

FIGURE 59. CURRENT PEAK (y_c) VS TIME

Photographic Results (figure 54.)
- □ 100 μHg Argon
- △ 250 μHg Argon
- ○ 500 μHg Argon

Magnetic Probe Results (figures 37. - 42.)
- ■ 100 μHg Argon
- ▲ 250 μHg Argon
- ● 500 μHg Argon

10.1 DETERMINATION OF SHOCK AND FLOW VELOCITIES (CONT'D.)

maximum current density. Thus the luminous plasma of the photographs corresponds to the plateau region of the current density distributions.

From figures 58. and 59., we see that the shock velocity and the particle flow velocity behind the shock front are approximately constant at this stage of the collapse. In Table VII we present the shock and flow velocities for the three initial gas pressures as determined from the slopes of these graphs.

PRESSURE (μHg)	TIME (μsec)	V_S (cm./μsec)	V_F (cm./μsec)
100	2.5	1.27	1.15
250	4	1.12	1.04
500	5	.91	.85

TABLE VII

SHOCK AND FLOW VELOCITIES

V_S = Velocity of shock front
V_F = Velocity of particle flow behind shock front.

10.2 DETERMINATION OF ELECTRIC FIELD

From the results of the previous section, we have seen that the region of high luminosity and the plateau region of the current density distributions coincide. From section 8.2 we have seen that the relatively small area of the discharge characterized by the

plateau region contains almost all of the discharge current. The large current and high luminosity indicate that this is a region of high temperature and high conductivity. To determine the conductivity we must know the electric field in the plasma and this may be calculated from the experimental data of sections 8.2 and 10.1.

From Maxwell's equation,

$$\nabla \times \underline{E} = -\frac{\partial B}{\partial t}$$

and, we have for the particular geometry of our experiment,

$$\frac{\partial E_z}{\partial r} = \frac{\partial B_\theta}{\partial t}$$

where we have used cylindrical coordinates with the z-axis coinciding with the axis of the discharge vessel (see figure 1.). Integration of this expression yields:

$$E_z(r) = \int_0^r \frac{\partial B_\theta}{\partial t}\, dr + E_z(o)$$

The second term on the right hand side of the expression represents an electric field the curl of which is equal to zero. This field could be a space charge electric field in the plasma. However, we assume that we may neglect this term compared to the electric field induced by the change of the magnetic field.

The electric field (E_z') seen by the plasma is modified by the plasma motion. Hence,

$$E_z'(r) = \int_0^r \frac{\partial B_\theta(r)}{\partial t}\, dr - v_r B_\theta(r)$$

10.2 DETERMINATION OF ELECTRIC FIELD (CONT'D.)

where v_r is the radial flow velocity of the plasma as determined in section 10.1.

The integral of the rate of change of magnetic field is proportional to the area between the magnetic field curves of figures 43. - 45. The procedure for evaluating this integral is as follows. Suppose we wish to determine the integral for the case of 500 μHg initial pressure, 5 μsec from initiation of the discharge, and at a radial position of 37 mm. The area (A) between the magnetic field curves corresponding to 4 μsec and 6 μsec is measured from the axis of the discharge out to a radius of 37 mm. This measurement is performed with a planimeter and the area is evaluated in wb/m. The integral is finally determined as:

$$\int_0^r \frac{\partial B\theta}{\partial t}\, dr = \frac{A}{2 \times 10^{-6}} \text{ v/m.}$$

The electric field (E') of the plasma is calculated as a function of radius through the plateau region of the current density for the various initial gas pressures at 1 μ sec intervals. These results are presented in Table VIII.

10.2 DETERMINATION OF ELECTRIC FIELD (CONT'D.)

PRESSURE AND TIME	RADIUS (mm)	AREA	E (kv/m.)	B (wb/m^2)	vB (kv/m.)	E-vB (kv/m.)
	48	5.19	3.20	.17	1.95	1.25
	51	6.09	3.75	.21	2.40	1.35
100 μHg	54	7.37	4.55	.25	2.90	1.65
Argon	57	8.40	5.18	.29	3.35	1.83
	60	9.67	5.95	.327	3.75	2.20
2 μsec	62	10.39	6.40	.354	4.05	2.35
	75	13.87	8.54			
	32	6.81	4.20	.189	2.18	2.02
	35	8.28	5.10	.234	2.69	2.41
100 μHg	38	9.74	6.00	.282	3.24	2.76
Argon	41	11.28	6.95	.327	3.76	3.19
	44	12.70	7.80	.375	4.32	3.48
3 μsec	47	13.91	8.55	.423	4.87	3.74
	51	15.48	9.55	.490	5.65	3.90
	75	18.54	11.40			
	49	8.81	2.72	.220	2.20	.52
250 μHg	52	11.61	3.58	.263	2.63	.95
Argon	55	13.31	4.10	.308	3.08	1.02
	57	14.47	4.46	.345	3.45	1.01
3 μsec	59	15.58	4.80	.384	3.84	.96
	75	19.75	6.08			
	37	12.19	3.70	.240	2.40	1.30
	39	13.55	4.13	.282	2.82	1.31
250 μHg	41	15.12	4.60	.318	3.18	1.42
Argon	43	16.42	5.00	.354	3.54	1.46
	45	17.73	5.40	.390	3.90	1.50
	47	18.81	5.74	.423	4.23	1.51
4 μsec	49	19.94	6.08	.463	4.63	1.45
	75	23.54	7.17			
	54	6.05	1.86	.18	1.53	.33
500 μHg	57	7.66	2.36	.23	1.95	.41
Argon	60	9.15	2.82	.285	2.34	.48
	63	10.82	3.33	.348	2.96	.37
3 μsec	67	11.48	3.54	.384	3.26	.28
	75	14.87	4.58			

TABLE VIII

DETERMINATION OF ELECTRIC FIELD

10.2 DETERMINATION OF ELECTRIC FIELD (CONT'D.)

PRESSURE AND TIME	RADIUS (mm)	AREA	E (kv/m.)	B (wb/m^2)	$\sqrt{}$B (kv/m.)	E-$\sqrt{}$B (kv/m.)
	46	6.87	2.12	.213	1.81	.31
500 μHg	50	8.72	2.69	.282	2.40	.29
Argon	54	10.92	3.36	.348	2.96	.40
	57	12.67	3.90	.400	3.40	.50
4 μsec	60	13.56	4.17	.468	3.98	.19
	75	15.58	4.80			
	37	7.28	2.22	.228	1.94	.28
500 μHg	39	8.31	2.52	.264	2.24	.28
Argon	41	9.39	2.85	.300	2.55	.30
	43	10.51	3.20	.336	2.86	.34
	45	11.58	3.53	.372	3.16	.37
5 μsec	47	12.34	3.75	.408	3.47	.28
	49	13.18	4.00	.444	3.77	.23
	75	13.92	4.24			
	21	4.04	1.24	.156	1.32	-.08
500 μHg	25	5.85	1.77	.216	1.83	-.06
Argon	29	7.77	2.39	.274	2.33	.06
	34	9.83	3.03	.348	2.96	.07
6 μsec	39	11.50	3.54	.423	3.60	-.06
	75	7.07	2.18			

TABLE VIII (CONT'D.)

DETERMINATION OF ELECTRIC FIELD

PART III

COMPARISON OF THEORETICAL MODELS WITH EXPERIMENTAL RESULTS

11.0 INTRODUCTION

In Part III of the thesis we wish to compare our experimental results with various theoretical models of the z-pinch discharge. There are presently three basic models - the "snowplow" model, the "shock wave" model and the "independent particle" model - and we describe the physical significance of each model in the following section. The models apply to different ranges of experimental conditions, but often the range of validity allows more than one theory to be applied to a given experiment. It will be shown in section 12.0 that both the snowplow model and the shock wave model provide useful concepts for the present experiment. However, all three models are discussed in section 12.0 for the purpose of comparison.

Section 13 deals with the snowplow approximation. The dynamic equation is developed and then solved using an approximation technique. The problem has been solved previously by numerical techniques (see Curzon (1963)), but it is felt that an analytic solution is advantageous because of the explicit appearance of the discharge parameters in the final solution. The validity of the analytic approximation must be tested by a comparison of theoretical and experimental results. This comparison is given in section 13.2.

In section 14, the Rankine Hugoniot relations are developed from the shock wave model. A system of six equations results and these are solved by a graphical technique. Again the theoretical results are compared with experimental results (see section 14.2).

11.0 INTRODUCTION (CONT'D.)

In section 14 we find that the shock wave model is inadequate for understanding of the experimental results. In section 15 we discuss a proposed model which is an extension of the shock wave model. This model does describe the experimental results.

12.0 THEORETICAL MODELS

The physical concepts associated with the three theoretical models - the "snowplow", "shock wave", and "independent particle" models - will now be discussed. In all three models it is assumed that the plasma conductivity is infinite. As the "skin depth" (characteristic thickness of current distribution) in the plasma is inversely proportional to the square root of the conductivity, we see that this assumption implies that the plasma current is restricted to a very thin sheet on the surface of the discharge plasma. The assumption of infinite conductivity also implies that the magnetic field does not penetrate the current sheet and it will be shown that a magnetic pressure is formed outside the current sheet which forces the sheet to constrict. Finally, the assumption implies that we have neglected the energy dissipation due to Joule heating. Of course, energy is still transmitted to the plasma through the motion of the current sheet.

The independent particle model is discussed by Gartenhaus (1964). It is assumed that the plasma particles are reflected by the collapsing current sheet and they return to the confined plasma with a velocity equal to twice the velocity of the current sheet.

In this model the confined plasma is approximately homogeneous, it is bounded by a very thin current sheet, and there is a vacuum between the current sheet and the discharge wall. The dynamic equation is derived from the rate of change of momentum of the individual plasma particles due to the increasing magnetic pressure.

If, however, the current sheet is strongly accelerated such that the reflected particles are swept up by the constricting sheet, then we have the "snowplow" model of the linear pinch. The model was first described by Rosenbluth (1954). In this case the central region of the discharge is left undisturbed until it is encountered by the collapsing sheet itself and the particles which are then swept up are assumed to form a very thin mass layer. Thus we have a cold gas which is enclosed by a thin mass sheet and a thin current sheet and the remainder of the discharge vessel will have been evacuated by the "snowplow". The dynamic equation in this case is derived from the rate of change of momentum of the mass layer due to the increasing magnetic pressure. The derivation of the dynamic equation for both the independent particle model and the snowplow model does not take into account the internal pressure due to the confined plasma or gas and thus these analyses are invalid for small radii of the current sheet.

In the third model, it is again assumed that we have a thin current sheet moving under the influence of the magnetic pressure, but it is now assumed that the reflected particles experience

collisions and a shock front is produced which precedes the collapsing current sheet. Thus we have a basic difference from the independent particle model where a collisionless plasma is considered. The equations governing the motion of the shock front are the standard Rankine-Hugoniot relations since we have assumed that the magnetic field is completly external to the current sheet. Several authors have discussed these equations. Allen (1957) has investigated the equations for plane geometry while Kuwabara (1963) has done the same for cylindrical geometry.

13.0 DYNAMIC EQUATION FROM SNOWPLOW APPROXIMATION

In this section we set up the mathematical equation which results from the snowplow model of the z-pinch discharge. It is observed that the magnetic pressure which causes the plasma to constrict is a function of the discharge current, but the current is affected by the constricting plasma through the change of inductance of the discharge. The result of this interdependence is that the problem requires the solution of two simultaneous, second order equations one of which is non-linear.

The first equation is derived from the snowplow model. It is assumed that the discharge forms a thin current sheet and this sheet sweeps up all the gas as the current sheet constricts. Internal pressure is neglected and the external magnetic pressure is determined by the discharge current.

13.0 DYNAMIC EQUATION FROM SNOWPLOW APPROXIMATION (CONT'D.)

The equation is, therefore, determined from Newton's law:

$$\frac{d}{dt}\left(\pi\rho_0(r_0^2 - r^2)\frac{dr}{dt}\right) = -2\pi r \cdot \frac{B^2}{2\mu_0} \qquad 13.1$$

where r is the radius of the current sheet
r_0 is the radius of the discharge vessel.
ρ_0 is the initial mass density of the gas
$B^2/2\mu_0$ is the magnetic pressure.

To simplify the following algebra, we let $y = r/r_0$ and we use the relationship:

$$B = \frac{\mu_0 I}{2\pi r} \qquad 13.2$$

where I is the discharge current in the sheet.

Equation 13.1 becomes:

$$\frac{d}{dt}(1 - y^2)\frac{dy}{dt} = -\frac{\mu_0 I^2}{4\pi^2 \rho_0 r_0^4 y} \qquad 13.3$$

A second equation is obtained for the current in the discharge circuit. The discharge circuit is shown in figure 1. (page 2.) and the circuit equation is:

$$\frac{d^2}{dt^2}(Le + Ld)\, I + \frac{I}{C} = 0 \qquad 13.4$$

where Le is the external circuit inductance
Ld is the inductance of the discharge
C is the total capacitance.

However, the discharge inductance is a function of y.

$$Ld = -\frac{\mu_o \ell}{2\pi} \ln \frac{r}{R} \qquad 13.5$$

$$= -\frac{\mu_o \ell}{2\pi} (\ln y + \ln \frac{r_o}{R})$$

where ℓ is the length of the discharge
R is the radius of the return conductor.

The total inductance of the discharge circuit is:

$$Le + Ld = Le\ (H - G \ln y) \qquad 13.6$$

where

$$G = \frac{\mu_o \ell}{2\pi Le} \qquad 13.7$$

and,

$$H = 1 - G \ln (r_o/R) \qquad 13.8$$

If we let,

$$I' = (Le + Ld)\ I \qquad 13.9$$

and,

$$W_o^2 = (LeC)^{-1} \qquad 13.10$$

equation 13.4 becomes,

$$\frac{d^2 I'}{dt^2} + \frac{W_o^2}{H - G \ln y} I' = 0 \qquad 13.11$$

with the initial conditions:

$$I'(0) = 0$$
$$\frac{dI'}{dt}(0) = V \qquad 13.12$$

13.0 DYNAMIC EQUATION FROM SNOWPLOW APPROXIMATION (CONT'D.)

Similarly equation 13.3 becomes,

$$\frac{d}{dt}(1-\eta^2)\frac{d\eta}{dt} = -\frac{F^2 I'^2}{\eta(H - G\ln\eta)^2} \qquad 13.13$$

where

$$F^2 = \frac{\mu_o}{4\pi^2 \rho_o r_o^4 L_e^2} \qquad 13.14$$

and the initial conditions are:

$$\eta(0) = 1$$
$$\frac{d\eta}{dt}(0) = 0 \qquad 13.15$$

13.1 ANALYTIC SOLUTION OF EQUATIONS

Equations 13.11 and 13.13 must be solved for I' and as functions of time. Equation 13.13 is a non-linear equation and there is no standard method of solution. This equation has been solved numerically (Curzon (1963b)), but if we could obtain even an approximate analytic solution, we could determine the dependence of I and η upon the variables we have defined above (i.e. r_o, R, l, ρ_o, Le, C, and V).

In order to find an approximate analytic solution we assume I' to be of the form:

$$I' = I'_o \sin\alpha_1(t) \qquad 13.16$$

Then

$$\dot{I}' \equiv \frac{dI'}{dt} = I'_o \dot{\alpha}_1 \cos\alpha_1$$

and,

$$\ddot{I}' \equiv \frac{d^2I'}{dt^2} = -I'_o\dot{\alpha}_1^2 \sin\alpha_1 + I'_o\ddot{\alpha}_1 \cos\alpha_1$$

13.1 ANALYTIC SOLUTION OF EQUATIONS (CONT'D.)

The initial conditions give $\alpha_1(0) = 0$, $I_o' = V/\dot{\alpha}_1(0)$

Similarly, we assume

$$y = y_o \cos\alpha_2(t) \qquad 13.17$$

Then, $\dot{y} = -y_o\dot{\alpha}_2 \sin\alpha_2$

and $\ddot{y} = -y_o\dot{\alpha}_2^2 \cos\alpha_2 - y_o\ddot{\alpha}_2 \sin\alpha_2$

The initial conditions give $\alpha_2(0) = 0$, $y_o = 1$

Substituting these expressions in the current equation (13.11), we find,

$$\ddot{\alpha}_1 \cos\alpha_1 - \dot{\alpha}_1^2 \sin\alpha_1 + \frac{W_o^2 \sin\alpha_1}{H - G\ln\cos\alpha_2} = 0$$

or, $$\ddot{\alpha}_1 (H - G\ln\cos\alpha_2) = \tan\alpha_1 (\dot{\alpha}_1^2(H - G\ln\cos\alpha_2) - W_o^2) \qquad 13.18$$

Similarly, the snowplow equation (13.13) yields,

$$(H - G\ln\cos\alpha_2)^2(\cos\alpha_2 \sin^3\alpha_2 \ddot{\alpha}_2 + 3\sin^2\alpha_2\cos^2\alpha_2\dot{\alpha}_2^2) = F^2 I_o'^2 \sin^2\alpha_1$$

or,

$$(H - G\ln\cos\alpha_2)^2(\cos\alpha_2 \sin^3\alpha_2 \ddot{\alpha}_2 + \tfrac{3}{4}\sin^2 2\alpha_2\dot{\alpha}_2^2) = F^2 I_o'^2 \sin^2\alpha_1 \qquad 13.19$$

Equations 13.18 and 13.19 must be solved simultaneously. To do this expand α_1 and α_2 in terms of t. We use the facts that $\alpha_1(0)$ and $\alpha_2(0)$ are zero and that α_1 and α_2 are, in general functions, of odd powers of t only.

That is,

$$\alpha_1 = W_1 t + at^3 + \cdots \qquad 13.20$$

$$\alpha_2 = W_2 t + bt^3 + \cdots \qquad 13.21$$

We also make use of the following expansions:

$$\tan\alpha_1 = \alpha_1 + \frac{\alpha_1^3}{3} + \cdots \qquad (\text{valid for } \alpha_1 < \pi/2)$$

$$\sin\alpha_2 = \alpha_2 - \frac{\alpha_2^3}{6} + \cdots \qquad (\text{valid for all } \alpha_2)$$

$$\cos\alpha_2 = 1 - \frac{\alpha_2^2}{2} + \cdots \qquad (\text{valid for all } \alpha_2)$$

$$\ln\cos\alpha_2 = -\frac{\alpha_2^2}{2} - \frac{\alpha_2^4}{12} - \ldots \qquad (\text{valid for } \alpha_2 < \pi/2)$$

Using these expansions, equation 13.18 now becomes, to order t^3,

$$6at\left(H + G\frac{w_2^2 t^2}{2}\right)$$

$$= \left(w_1 t + \left(a + \frac{w_1^3}{3}\right)t^3\right)\left((w_1 + 3at^2)^2\left(H + \frac{Gw_2^2 t^2}{2}\right) - w_o^2\right) \qquad 13.22$$

Similarly equation 13.19 becomes, to order t^4,

$$\left(H + \frac{G w_2^2 t^2}{2}\right)^2\left((w_2 t)^3\, 6bt + \frac{3}{4}\left(2w_2 t + \left(2b - \frac{8}{6}w_2^3\right)t^3\right)^2\left(w_2 + 3bt^2\right)^2\right)$$

$$= F^2 I_o'^2 \left(w_1 t + \left(a - \frac{w_1^3}{6}\right)t^3\right)^2 \qquad 13.23$$

For these series expansions to be true for arbitrary time, the coefficients of t^n must each vanish. Thus from equation 13.22, the coefficient of t gives,

$$6aH = w_1 (Hw_1^2 - w_o^2) \qquad 13.24$$

and the coefficient of t^3 gives,

$$3aGw_2^2 = 6aw_1^2H + \frac{G}{2} w_1^3 w_2^2 + (Hw_1^2 - w_o^2)(a + \frac{w_1^3}{3}) \qquad 13.25$$

Similarly, from equation 13.23, the coefficient of t^2 gives,

$$3H^2w_2^4 = F^2I_o'^2 w_1^2 \qquad 13.26$$

and the coefficient of t^4 gives,

$$6bH^2w_2^3 + 18w_2^3bH^2 + 6bH^2w_2^3 - 4H^2w_2^6 + 3HGw_2^6 = F^2I_o'^2 2w_1 (a - \frac{w_1^3}{6})$$

or,

$$(\frac{3G}{H} - 4) w_2^6 + 30bw_2^3 = \frac{F^2I_o'^2 2w_1}{H^2} (a - \frac{w_1^3}{6}) \qquad 13.27$$

The four parameters a, b, w_1, and w_2, may now be determined. Equation 13.24 gives,

$$a = \frac{w_1}{6H} (Hw_1^2 - w_o^2) \qquad 13.28$$

Equation 13.26 gives,

$$w_2 = \left(\frac{FI_o'w_1}{\sqrt{3}H} \right)^{\frac{1}{2}} \qquad 13.29$$

or by substituting 13.12 and 13.16 in equation 13.29,

$$w_2 = \left(\frac{FV}{\sqrt{3H}}\right)^{\frac{1}{2}} \qquad 13.30$$

Combining 13.25 and 13.26, we obtain

$$\frac{F^2 I_o^2}{H^2} 2w_1 \left(a - \frac{w_1^3}{6}\right) = \frac{w_o^2 w_2^4}{H} \qquad 13.31$$

and thus equation 13.27 becomes,

$$b = \frac{(4H - 3G)}{30H} w_2^3 - \frac{w_o^2 w_2}{30H} \qquad 13.32$$

The fourth parameter, w_1, is obtained from a combination of equations 13.24 and 13.25.

$$(9Hw_1^2 - w_o^2)(Hw_1^2 - w_o^2) = -3Gw_2^2 w_o^2 = -\sqrt{3}\,\frac{FGV}{H} w_o^2 \qquad 13.33$$

In order to solve equation 13.33 for w_1, we write $x^2 = Hw_1^2/w_o^2$ and write equation 13.33 as,

$$(9x^2 - 1)(x^2 - 1) = -k \qquad 13.34$$

where

$$k = \sqrt{3}\,\frac{FGV}{w_o^2 H} \qquad 13.35$$

If we assume that $x = 1 - \varepsilon$ where $\varepsilon \ll 1$, then,

$$\varepsilon(1 - 2\varepsilon) = \frac{k}{18} \qquad 13.36$$

Therefore,

$$4\varepsilon = 1 \pm \left(1 - \frac{4}{9}k\right)^{\frac{1}{2}} \qquad 13.37$$

and finally,

$$w_1 = \frac{w_0}{\sqrt{H}}\left(\frac{3}{4} + \frac{1}{4}\left(1 - \frac{4k}{9}\right)^{\frac{1}{2}}\right) \qquad 13.38$$

Considering the case of $\rho_0 \to \infty$ (i.e. when the plasma can not constrict) we find that the positive square root must be taken. In this case, $F(\rho_0) \to 0$ (see equation 13.14) and $k(\rho_0) \to 0$ (see equation 13.35) and thus $w_1 \to w_0/\sqrt{H}$.

The following argument shows that this is correct. We know

$$\frac{w_1}{w_0} = \left(\frac{Le}{Ld + Le}\right)^{\frac{1}{2}} \qquad 13.39$$

and also, when the plasma can not constrict,

$$\begin{aligned} Ld + Le &= Le\,(H - \ln \eta_0) \\ &= Le\,(H - \ln 1) \\ &= LeH \end{aligned} \qquad 13.40$$

Thus for the case of $\rho_0 \to \infty$, equations 13.39 and 13.40 show that $w_1 \to w_0/\sqrt{H}$ which is the desired result.

Equation 13.34 can also be solved graphically as shown in figure 60. We plot $f(x) = (9x^2 - 1)(x^2 - 1)$ against x and the solution is obtained at the intersection of this function with the constant $k(\rho_0)$. For our experimental configuration $k(\rho_0) = .13 \times 10^{-6} F(\rho_0)$.

13.1 ANALYTIC SOLUTION OF EQUATION (CONT'D.)

Values of $k(\rho_0)$ corresponding to initial pressures of 100, 250, and 500 μHg of argon are given in Table IX.

PRESSURE (μHg)	$F(\rho_0)$	$k(\rho_0)$
100	18.2×10^6	2.37
250	11.5×10^6	1.50
500	8.15×10^6	1.06

TABLE IX

DETERMINATION OF $k(\rho_0)$

$F(\rho_0)$ given by equation 13.14
$k(\rho_0)$ given by equation 13.35

Figure 60. shows that real roots are obtained for w_1 only when the initial argon pressure is greater than 200μHg. The significance of this result can be seen in the following discussion.

The equation for the discharge current is (13.9):

$$I = \frac{I'}{L}$$

$$= \frac{V}{w_1 L} \sin (w_1 t + at^3)$$

$$= \frac{V}{Z(w_1)}$$

where $Z(w_1)$ is an apparent impedance. Thus for initial pressures less than 200μHg (where we have a complex solution for w_1), we have a circuit which is represented by a complex impedance. Our circuit shows resistive effects which are due to the rapid rate of change of

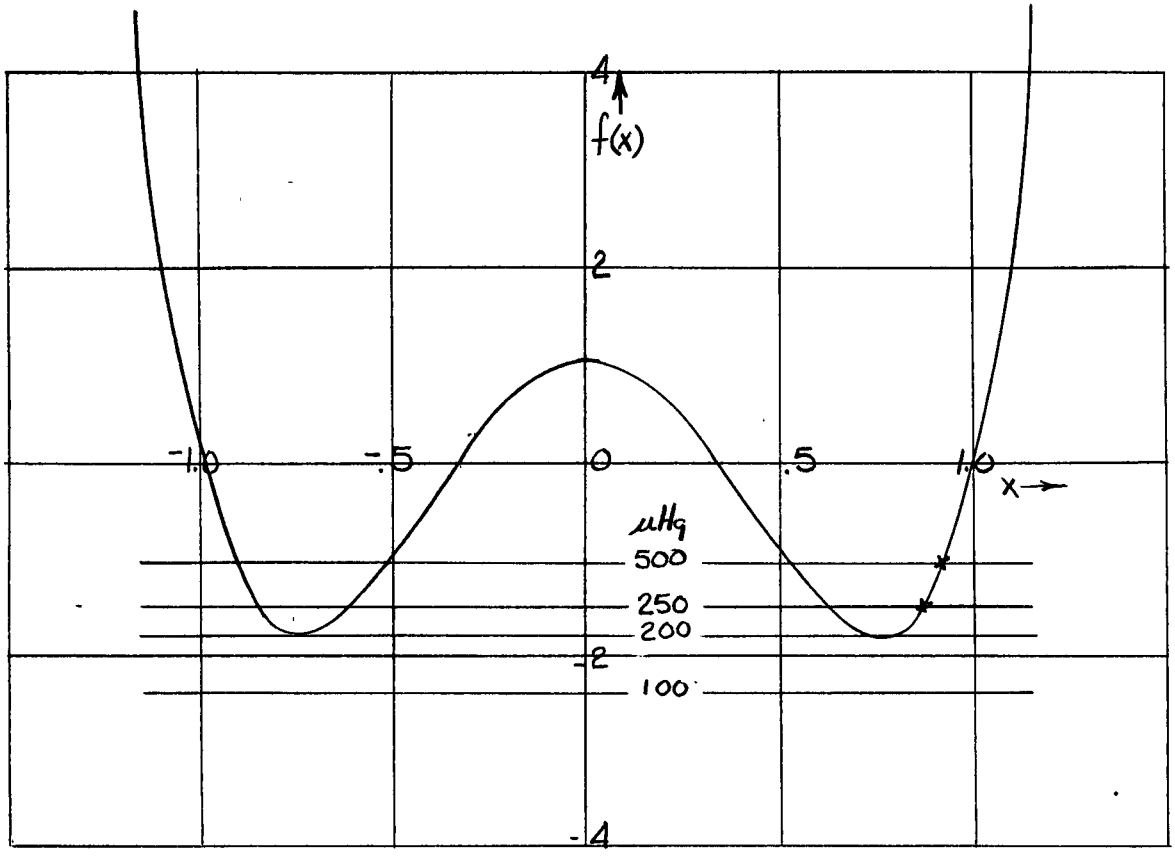

FIGURE 60. GRAPHICAL SOLUTION FOR w:

13.1 ANALYTIC SOLUTION OF EQUATION (CONT'D.)

the inductance of the discharge.

$$\frac{d}{dt}(LI) = L\frac{dI}{dt} + I\frac{dL}{dt} \qquad 13.41$$

The second term represents the resistive term. As the collapse is more rapid in low pressure gases, we find that this term becomes appreciable at argon pressures less than 200 μHg.

To summarize this section, we have obtained an analytic approximation for the radius of the collapsing plasma discharge.

$$y = \cos(w_2 t + bt^3) \qquad 13.42$$

where

$$w_2 = \left(\frac{FV}{\sqrt{3H}}\right)^{\frac{1}{2}}$$

$$b = \frac{(4H - 3G)}{30H} w_2^3 - \frac{w_o^3 w_2^2}{30H}$$

and,

$$F^2 = \frac{\mu_o}{4\pi^2 \rho_o r_o^4 L_e^2}$$

$$G = \frac{\mu_o l}{2\pi L_e}$$

$$H = 1 - G \ln(r_o/R)$$

$$w_o^2 = 1/LeC$$

where
- l is the length of the discharge vessel
- r_o is the inner radius of the discharge vessel
- R is the radius of the return conductor
- ρ_o is the initial gas density
- Le is the external circuit inductance
- C is the external capacitance

and,
- V is the initial voltage on the capacitor.

We have also obtained an analytic approximation for the discharge current.

$$I = \frac{V}{w_1 Le(H - G \ln y)} \sin(w_1 t + at^3) \qquad 13.43$$

where

$$w_1 = \frac{w_o}{\sqrt{H}}\left(\frac{3}{4} + \frac{1}{4}(1 - \frac{4k}{9})^{\frac{1}{2}}\right)$$

$$k = \frac{\sqrt{3}\, FGV}{w_o^2 H}$$

13.1 ANALYTIC SOLUTION OF EQUATION (CONT'D.)

$$a = \frac{w_1}{6H}\left(Hw_1^2 - w_o^2\right)$$

and the remaining variables are as defined for equation 13.42.

13.2 COMPARISON OF THEORETICAL AND EXPERIEMENTAL RESULTS

In this section we calculate the discharge radius (y) and current (I) using equations 13.42 and 13.43 with the discharge parameters of the experimental apparatus as given in Table I (section 7.0). We then compare these results with the observed values.

From Table I we obtain the following.

Discharge Circuit:
$C = 53\ \mu F$
$Le = .12\ \mu H$
$V = 10$ kV

Discharge Vessel:
$l = .75$ m
$r_o = .075$ m
$R = .085$ m

$$\rho_o = 2.13 \times 10^{-6} \times (\text{Pressure in } \mu\text{Hg})\ \text{kg/m}^3$$

In the following three examples, M.K.S.Q. units are used.

Example 1. 500 μHg Argon:

The following variables are defined in terms of the discharge parameters by equations 13.42 and 13.43.

$F = 8.15 \times 10^6$
$G = 1.3$
$H = 1.14$

$w_o = .396 \times 10^6\ \text{sec}^{-1}$
$w_1 = .339 \times 10^6\ \text{sec}^{-1}$
$w_2 = .204 \times 10^6\ \text{sec}^{-1}$

13.1 COMPARISON OF THEORETICAL AND EXPERIMENTAL RESULTS (CONT'D.)

Example 1. 500 μHg Argon: (Cont'd.)

$k = 1.06$ $\qquad a = -.00104 \times 10^{18}\ sec^{-3}$, $\quad b = .00074 \times 10^{18}\ sec^{-3}$

$$y = \cos(w_2 t + bt^3)$$

t (μsec)	$w_2 t$	bt^3	α_2	y	$\ln y$
0	0	0	0	1.00	0
1	.204	.001	.203	.98	-.022
2	.408	.006	.402	.92	.083
3	.612	.020	.592	.83	.186
4	.816	.047	.769	.72	.348
5	1.020	.093	.927	.60	.510
6	1.224	.160	1.064	.485	.724
7	1.428	.254	1.174	.385	.955
8	1.632	.379	1.253	.31	1.17
9	1.836	.540	1.296	.26	1.345
10	2.040	.740	1.300	.27	1.77
11	2.244	.984	1.260	.305	1.19

$$I = \frac{V \sin(w_1 t + at^3)}{w_1 L_e (H - G \ln y)}$$

t (μsec)	$w_1 t$	at^3	α_1	$\sin\alpha$	$-G \ln y$	I(kA)
0				0		0
1	.339	-.001	.338	.33	.029	69
2	.678	-.008	.670	.62	.108	122
3	1.017	-.028	.989	.84	.242	150
4	1.356	-.067	1.289	.96	.454	149
5	1.695	-.130	1.565	1.00	.664	137
6	2.034	-.225	1.809	.95	.942	112
7	2.373	-.360	2.013	.91	1.24	94
8	2.712	-.533	2.179	.82	1.52	76
9	3.051	-.758	2.293	.75	1.75	64
10	3.39	-1.040	2.35	.71	2.30	51
11						

13.1 COMPARISON OF THEORETICAL AND EXPERIMENTAL RESULTS (CONT'D.)

Example 2. 250 μHg Argon:

$F = 11.5 \times 10^6$ $\quad w_o = .396 \times 10^6$ sec^{-1}
$G = 1.3$ $\quad w_1 = .325 \times 10^6$ sec^{-1}
$H = 1.14$ $\quad w_2 = .243 \times 10^6$ sec^{-1}

$k = 1.5$ $\quad a = -.00124 \times 10^{18}$ sec^{-3}
$b = .00081 \times 10^{18}$ sec^{-3}

$$y = \cos(w_2 t + bt^3)$$

t (μsec)	$w_2 t$	bt^3	α_2	y	$\ln y$
0	0	0	0	1	0
1	.243	.001	.242	.97	-.035
2	.486	.006	.480	.89	.117
3	.729	.022	.707	.76	.274
4	.972	.052	.920	.60	.510
5	1.215	.101	1.114	.44	.820
6	1.458	.175	1.283	.28	1.27
7	1.701	.278	1.423	.15	1.90
8	1.944	.415	1.529	.04	3.22
9	2.187	.590	1.597	-.02	

$$I = \frac{V \; si \; (w_1 t + at^3)}{w_1 Le(H - G \ln y)}$$

t (μsec)	$w_1 t$	at^3	α_1	$\sin\alpha_1$	$-G \ln y$	I (kamp)
0						0
1	.325	-.001	.324	.32	.046	70
2	.650	-.009	.641	.60	.152	120
3	.975	-.033	.942	.81	.357	149
4	1.300	-.050	1.250	.95	.664	136
5	1.625	-.155	1.470	.99	1.066	115
6	1.950	-.268	1.682	.99	1.65	91
7	2.275	-.425	1.850	.96	2.47	68
8	2.600	-.635	1.965	.92	4.19	44
9	2.925	-.905	2.020	.90		

13.1 COMPARISON OF THEORETICAL AND EXPERIMENTAL RESULTS (CONT'D.)

Example 3. 100 μHg Argon:

$F = 18.2 \times 10^6$ $\quad w_o = .396 \times 10^6 \text{ sec}^{-1}$
$G = 1.3$ $\quad w_2 = .305 \times 10^6 \text{ sec}^{-1}$
$H = 1.14$ $\quad b = -.00109 \times 10^{18} \text{ sec}^{-3}$
$k = 2.37$

$w_1 = (.271 + .021i) \times 10^6 \text{ sec}^{-1}$
$a = -(.0043 - .0003i) \times 10^{18} \text{ sec}^{-1}$

$$\eta = \cos (w_2 t + bt^3)$$

t (μsec)	$w_2 t$	bt^3	α_2	η	$\ln \eta$
0	0	0	0	1	0
1	.305	.001	.304	.95	-.051
2	.610	.009	.601	.82	.198
3	.915	.029	.886	.63	.462
4	1.220	.070	1.150	.41	.891
5	1.525	.136	1.389	.18	1.71
6	1.830	.235	1.595	-.02	

$$I = \frac{V \sin (w_1 t + at^3)}{w_1 Le(H - G \ln \eta)}$$

t (μsec)	$w_1 t$	at^3	$\sin (w_1 t + at^3)$
1	.271 + .021i	- .004	.27 + .019i
2	.542 + .042i	-.034 + .002i	.49 + .038i
3	.813 + .063i	-.116 + .008i	.64 + .054i
4	1.084 + .084i	-.275 + .019i	.72 + .069i
5	1.355 + .105i	- .538 + .037i	.73 + .095i

(continued)

t (μsec)	$-G \ln \eta$	$\frac{V}{w_1 Le(H-G\ln\eta)}$ x 10^3	I x 10^3	I (kamp)
1	.066	257 + 20i	69.2 + 10i	70
2	.258	222 + 17i	109 + 16i	110
3	.600	178 + 14i	113 + 21i	115
4	1.16	134 + 10i	96 + 16i	98
5	2.22	92 + 7i	67 + 13i	68

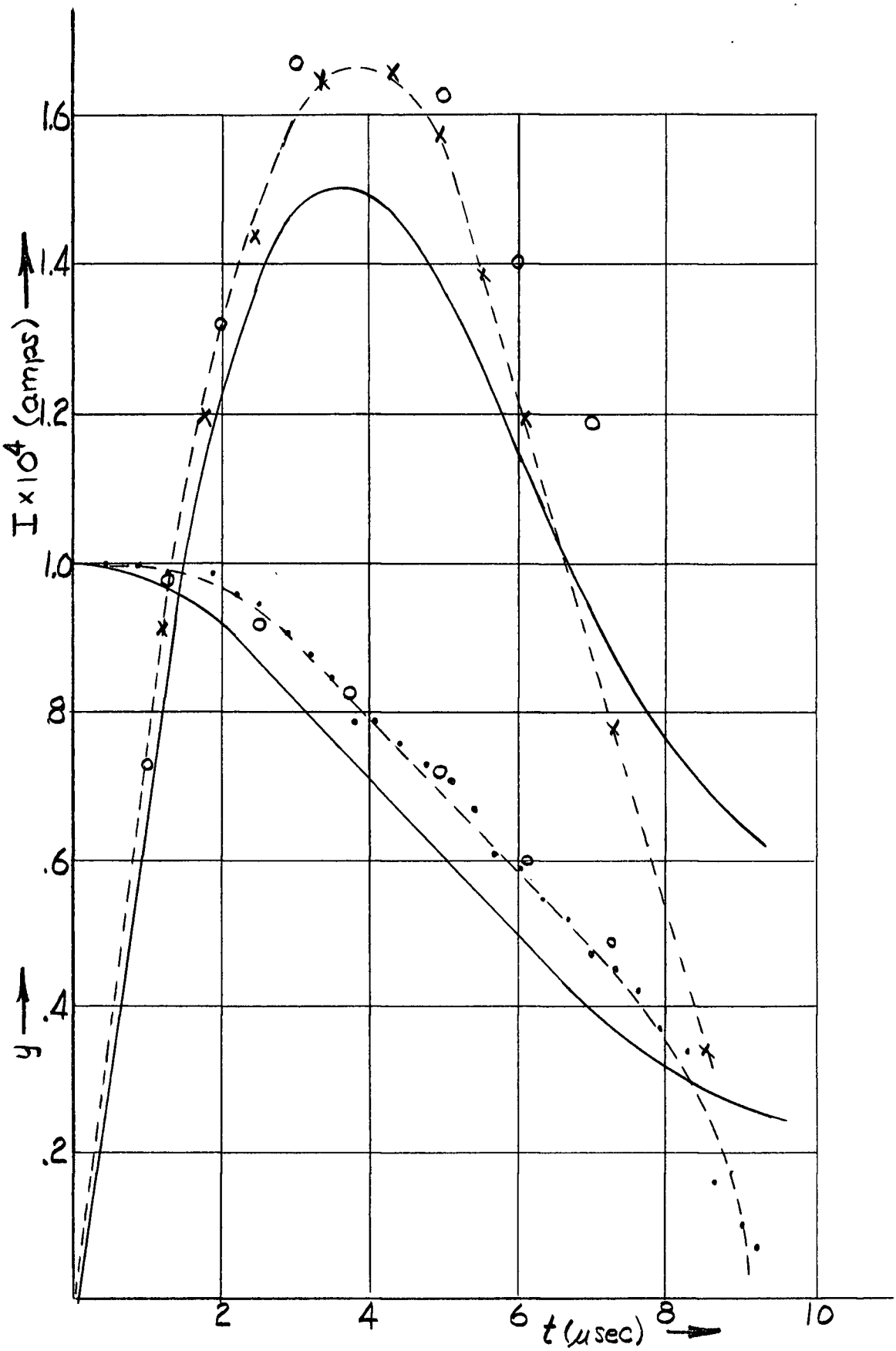

FIGURE 61. SNOWPLOW MODEL AND EXPERIMENTAL RESULTS (500 μHg Argon)

—x—Experimental Current — Current from Snowplow Model
—•—Experimental Collapse — Collapse from Snowplow Model
o Corrected Snowplow Model

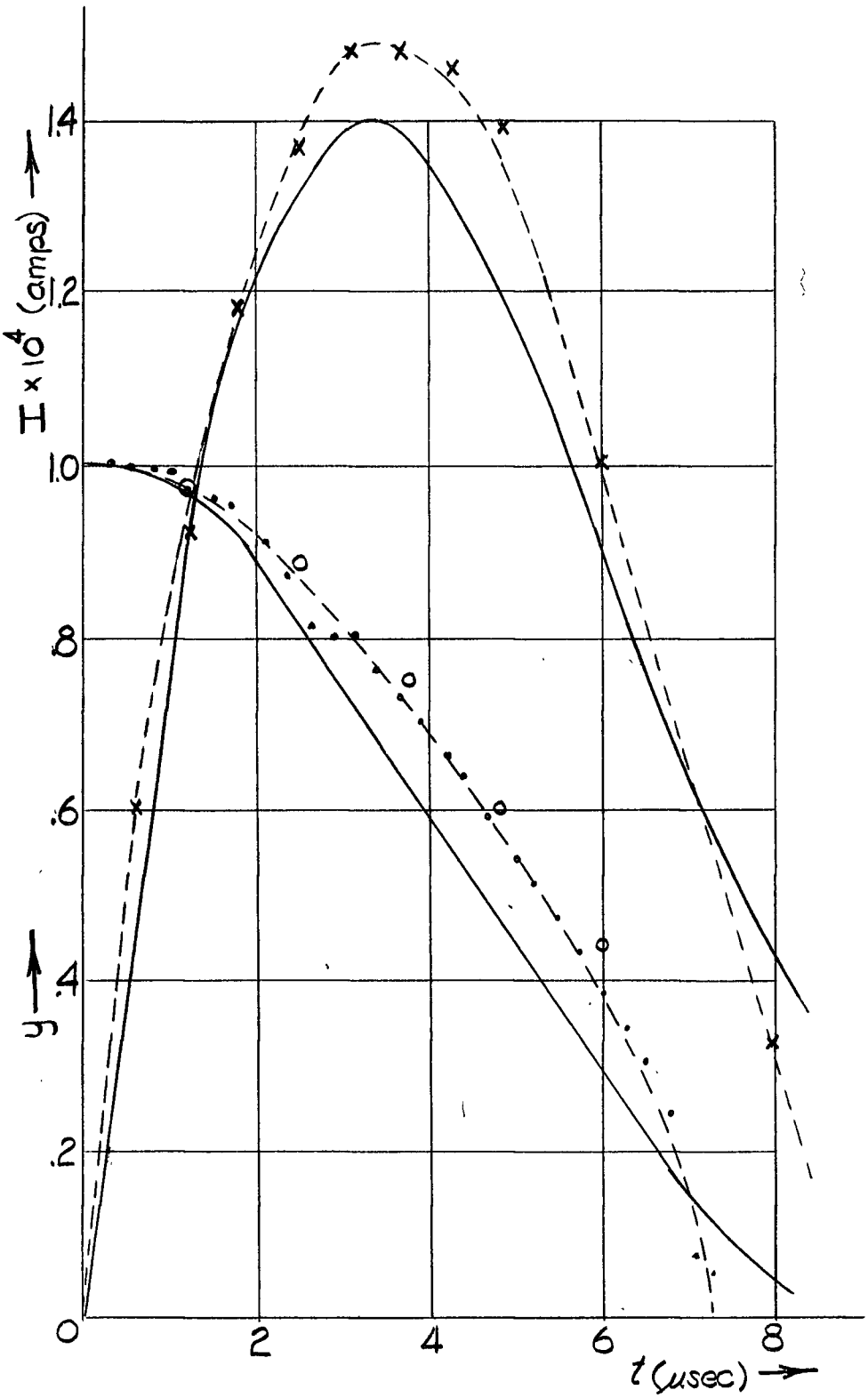

FIGURE 62. SNOWPLOW MODEL AND EXPERIMENTAL RESULTS (250 μHg Argon)

-x-Experimental Current — Current from Snowplow Model
-·-Experimental Collapse — Collapse from Snowplow Model
o Corrected Snowplow Collapse

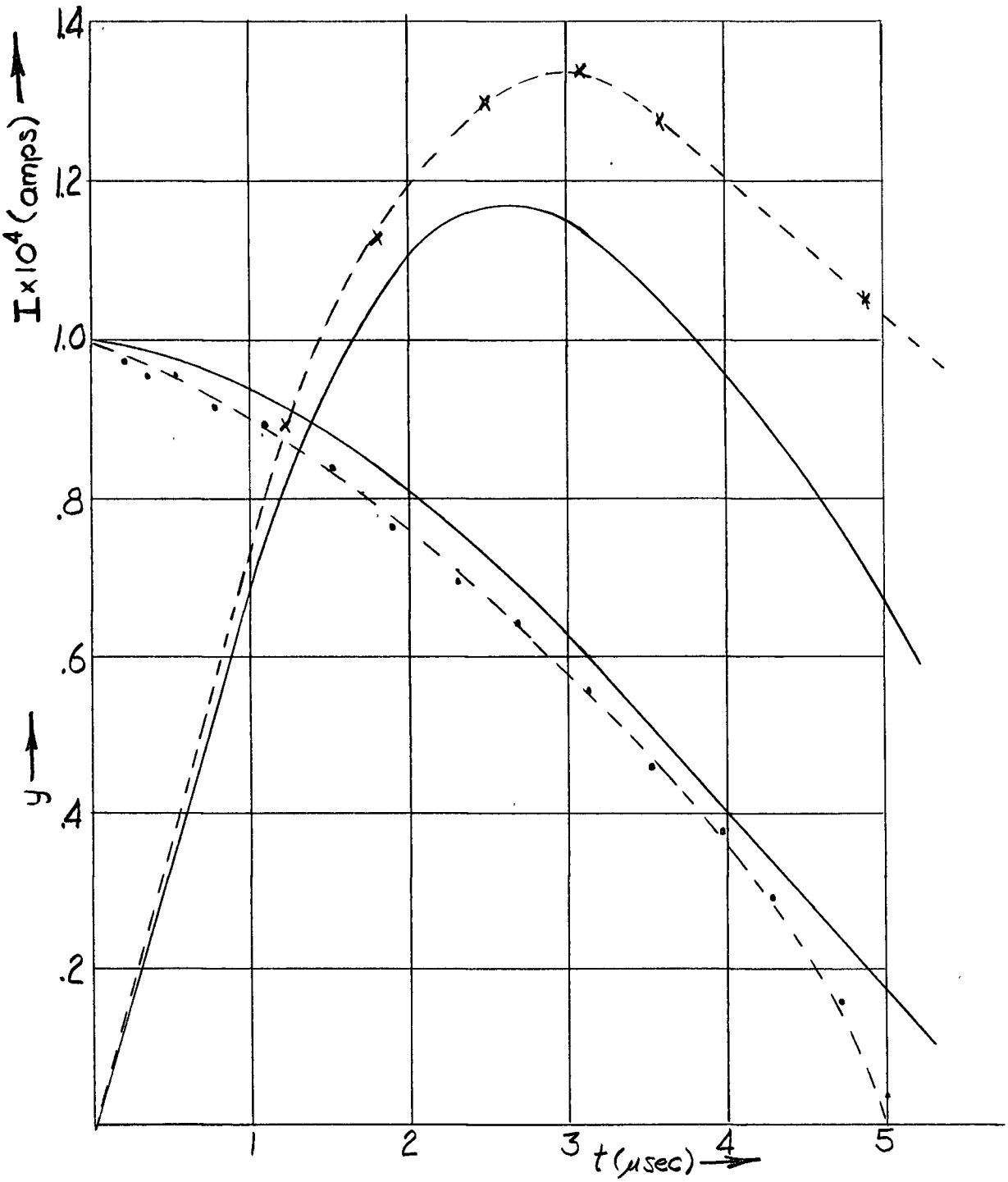

FIGURE 63. SNOWPLOW MODEL AND EXPERIMENTAL RESULTS (100 μHg Argon)

—x—Experimental Current — Current from Snowplow Model
—••—Experimental Collapse — Collapse from Snowplow Model

13.1 COMPARISON OF THEORETICAL AND EXPERIMENTAL RESULTS (CONT'D.)

In figures 61 - 63 we have plotted experimental and theoretical curves of both I and y for each of the three initial argon pressures used in the present experiment. The experimental value of the current and plasma radius are obtained from figure 29 (section 7.1) and figure 54 (section 9.2), respectively.

The experimental curves of figures 61 - 63 show the trend of the theoretically predicted curves, but the theoretical current is less than the observed current. Even with a current which is too small, the theoretical calculation predicts a collapse which is too fast. This is a surprising result and it implies that not all the discharge current is used to accelerate the plasma toward the axis of the discharge vessel. Indeed the equivalent circuit of figure 64 is probably a more realistic approximation of the discharge circuit, than the circuit assumed in section 13.1.

What is the physical significance of the inductance L_o? In the current density distributions obtained in section 8.2, we have observed that there is a considerable current which lies inside the "knee" of the current density curve. We have also observed that the shock front, i.e. the concentration of mass, coincides with the position of the "knee" of the current density curve. Therefore, the current lying inside this "knee" does not accelerate the mass of gas. It is the current which we assume flows through the inductance L_o.

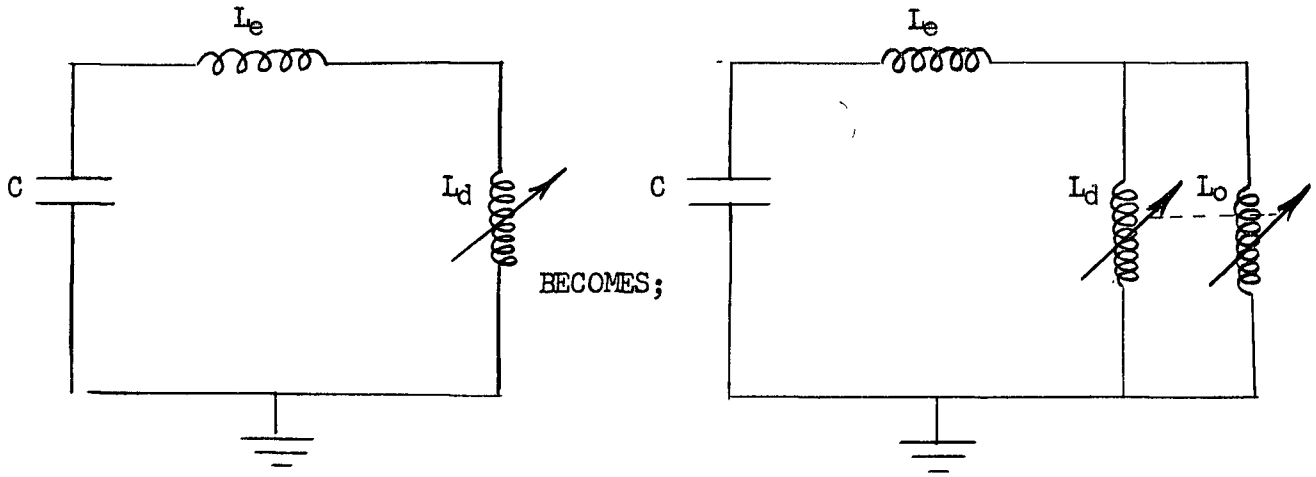

FIGURE 64. MODIFIED DISCHARGE CIRCUIT

13.1 COMPARISON OF THEORETICAL AND EXPERIMENTAL RESULTS (CONT'D.)

For simplicity we assume that Lo is proportional to L_d.

$$Lo = \frac{Ld}{\lambda} \qquad 13.44$$

Thus the total inductance of the circuit is now,

$$L = Le + (1 + \lambda)^{-1} Ld \qquad 13.45$$

and the circuit equation becomes,

$$\frac{d^2I'}{dt^2} + \frac{w_o^2}{H' - G' \ln 4} I' = 0 \qquad 13.46$$

where $I' = IL$ and I is the total discharge current.

$$G' = (1 + \lambda)^{-1} G \qquad 13.47$$

$$H' = 1 - G' \ln(r_o/R) \qquad 13.48$$

The snowplow equation is,

$$\frac{d}{dt}(1-\eta^2)\frac{d\eta}{dt} = -\frac{F'^2 I'^2}{\eta(H' - G'\ln\eta)} \qquad 13.49$$

where $F' = (1+\lambda)F$.

The advantage of an analytic solution to the problem now becomes obvious. The new total current I' can be determined from the calculated values of I above as:

$$I' = \frac{H - G\ln\eta}{H' - G'\ln\eta} \times I \qquad 13.50$$

and to a good approximation,

$$\eta' \sim \cos\left(w_2\sqrt{1+\lambda t} + b^3\sqrt{1+\lambda t^3}\right) \qquad 13.51$$

i.e. the new η' is determined from the previous η by a simple expansion of the time scale,

$$t' = 1+\lambda t \qquad 13.52$$

We now require an estimate for λ. λ has been determined experimentally and it is most easily obtained from the data of Table VIII. Since I(r), the current within a radius r is proportional to $r \cdot B(r)$, then $r_k \cdot B(r_k)$ is proportional to the current within r_k where r_k is the radial position of the knee of the current density distribution. This value is thus a measure of I_{Lo}. Similarly $r_p \cdot B(r_p)$ is proportional to the current within the radial position of the current density peak. Thus $r_p \cdot B(r_p) - r_k \cdot B(r_k)$ is a measure of I_{Ld}.

13.1 COMPARISON OF THEORETICAL AND EXPERIMENTAL RESULTS (CONT'D.)

Now,
$$\frac{I_{Lo}}{I_{Ld}} = \frac{Ld}{Lo} = \lambda$$

The results are given in Table X.

PRESSURE	TIME	$k(I_{Ld} + I_{Lo})$	kI_{Lo}	kI_{Ld}	λ
100	2	220	80	140	.6
	3	250	60	190	.3
250	3	227	108	120	.9
	4	227	89	140	.6
500	3	257	97	160	.6
	4	281	98	180	.6
	5	218	84	135	.6
	6	165	83	130	.3

TABLE X

DETERMINATION OF λ

As an example of this procedure we correct the results of Example 1. for the effects of the inductance Lo. From equation 13.52 we see that the collapse curve is corrected through a 25% expansion of the time base. The corrected discharge current must be calculated from equation 13.50. This calculation is given in Table XI.

The corrected results compare very favourably with the measured collapse curve and discharge current for the case of 500 μHg argon.

13.1 COMPARISON OF THEORETICAL AND EXPERIMENTAL RESULTS (CONT'D.)

TIME (μsec)	H - G$\ln\eta$	H' - G'$\ln\eta$	I' (kamp)
1	1.17	1.11	73
2	1.25	1.16	132
3	1.38	1.24	167
4	1.59	1.37	173
5	1.80	1.51	163
6	2.08	1.67	140
7	2.37	1.87	119
8	2.66	2.04	99
9	2.89	2.19	85
10	3.44	2.53	69

TABLE XI

MODIFICATION OF SNOWPLOW CALCULATION

H = 1.14 H' = 1.09
G = 1.3 G' = .81

I' determined from equation 13.50

The rather large error on the measured current is due to the 7% uncertainty in calibrating the Rogowski coil. In figure 62. we have also plotted the corrected collapse curve although the assumption of constant λ is questionable for the case of 250 μHg argon.

It should be observed that the collapse curve for 100 μHg argon is in poor agreement with theory. The current discrepancy is corrected by the inductance effect discussed above, but the discrepancy of the collapse curve is accentuated by this correction. It is probable that the collapsing plasma does not sweep up all of the initial gas and this would account for the more rapid collapse than has been predicted by theory.

13.1 COMPARISON OF THEORETICAL AND EXPERIMENTAL RESULTS (CONT'D.)

The very good agreement for the cases of 250 and 500 μHg indicates an efficient sweeping up of the gas. This observation is important for the discussion of the shock wave model in the next section.

14.0 DYNAMIC EQUATION FROM SHOCK WAVE MODEL

The snowplow model predicts the position of the constricting plasma in the z-pinch as a function of time, but it yields no information on the plasma temperature, the ionization ratio, the plasma pressure and the mass density of the plasma. To investigate these macroscopic parameters we make use of the "shock wave" model.

As our magnetic probe measurements are restricted to regions of large y (see section 8.3) due to possible errors in the regions of small y, we can obtain estimates for the above parameters only at early times in the discharge process, i.e. 2-4 μsec after initiation. It can be seen from the collapse curves of figure 54. that the radial velocity of the collapsing plasma is approximately constant in this region and this allows an accurate measurement of the velocity of the shock front. Also, for large y (0.4 - 0.6), we can use the plane shock wave model because effects of curvature of the cylindrical plasma sheet are small. We include the effect of ionization in the Rankine - Hugoniot relations (see, for example, Resler (1952)).

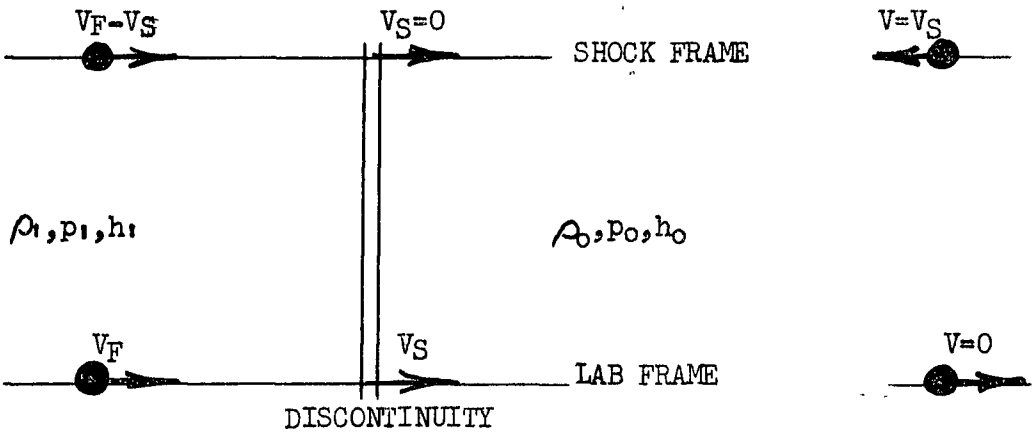

FIGURE 65. SHOCK WAVE PARAMETERS

Parameters defined in Table XII

α	First ionization ratio = n_i/n
β	Second ionization ratio = n_{ii}/n
h	Enthalpy/unit mass
m	Atomic mass of argon = 6.68×10^{-26}kg
n	Initial density of poles/m^3
n_o	Final density of neutrals/m^3
n_i	Final density of singly ionized atoms/m^3
n_{ii}	Final density of doubly ionized atoms/m^3
p	Pressure (nt/m^2)
Q_i	First ionization potential = 2.51×10^{-18}j
Q_{ii}	Second ionization potential = 4.39×10^{-18}j
q_i	First ion potential/unit mass = $.376 \times 10^8$j/kg
q_{ii}	Second ion potential/unit mass = $.656 \times 10^8$j/kg
ρ	Mass density (kg/m^3)
R_o	Gas constant/unit mass = 208 j/kg
T	Temperature (^oK)
V_F	Flow velocity of fluid behind shock front
V_S	Velocity of shock wave.

TABLE XII

SHOCK WAVE PARAMETERS

14.0 DYNAMIC EQUATION FROM SHOCK WAVE MODEL (CONT'D.)

The variables in the Rankine - Hugoniot relations are defined in Table XII and illustrated in figure 65. The variables subscripted "0" correspond to the initial conditions and the variables subscripted "1" correspond to the shock heated conditions.

From the conservation of mass across the shock discontinuity, we obtain,

$$\rho_0 V_S = \rho_1 (V_S - V_F)$$

i.e.

$$\frac{\rho_1}{\rho_0} = \frac{V_S}{V_S - V_F} \qquad 14.1$$

From the conservation of momentum across the shock front, we obtain:

$$p_0 + \rho_0 V_S^2 = p_1 + \rho_1 (V_S - V_F)^2 \qquad 14.2$$

In writing this equation we have assumed that we can neglect the discontinuity of the magnetic pressure at the shock front - a term which has been introduced into the Rankine - Hugoniot relations by de Hoffman (1950). From our theoretical model this is justified as we have assumed no magnetic field in the shock heated region. Also, the measured magnetic field (see section 8.2) shows no discontinuity, although there is a magnetic field within the main current sheet.

We further simplify the above relationship by neglecting the pressure ahead of the shock wave compared with the pressure behind the shock wave.

14.0 DYNAMIC EQUATION FROM SHOCK WAVE MODEL (CONT'D.)

Then, upon substitution of ρ_1 from equation 14.1, we obtain:

$$V_F = \frac{p_1}{\rho_o V_S} \tag{14.3}$$

with the assumptions: $B_1 \sim B_o$, $p_1 >> p_o$ (14.4)

From the conservation of energy across the shock discontinuity, we obtain:

$$h_o + \frac{1}{2} V_S^2 = h_1 + \frac{1}{2} (V_S - V_F)^2 \tag{14.5}$$

where $$h = \frac{5}{2} (1+\alpha+2\beta) R_o T + \alpha q_i + \beta (q_i + q_{ii})$$

Assuming that $h_o \ll h_1$ and upon substitution of equation 14.3, we have,

$$T_1 = \frac{2}{5(1+\alpha+2\beta)R_o} \left(\frac{p_1}{2\rho_o^2 V_S^2} \left(2\rho_o V_S^2 - p_1 \right) - \alpha q_i - \beta (q_i + q_{ii}) \right) \tag{14.6}$$

Assuming that we have an ideal gas, we can write the equation of state as;

$$\frac{p_1}{\rho_1} = (1+\alpha+2\beta) R_o T_1 \tag{14.7}$$

and upon substitution of equation 14.1 and equation 14.3,

$$T_1 = \frac{p_1}{\rho_o^2 V_S^2} \frac{(\rho_o V_S^2 - p_1)}{(1+\alpha+2\beta)R_o} \tag{14.8}$$

14.0 DYNAMIC EQUATION FROM SHOCK WAVE MODEL (CONT'D.)

Finally we obtain from Saha's equation, two equations for the ionization ratios α and β. Saha's equation actually gives the ratio of the number densities of the various constituents of the plasma as a function of temperature. They are of the form;

$$\frac{n_i n_e}{n_o} = f_i(T_1) \tag{14.9}$$

$$\frac{n_{ii} n_e}{n_i} = f_{ii}(T_1) \tag{14.10}$$

where $$f_i(T_1) = \frac{g_i g_e}{g_o}\left(\frac{m_e k T_1}{2\pi\hbar^2}\right)^{3/2} e^{-\frac{Q_i}{kT_1}}\left(1 + \frac{e^3}{\pi\varepsilon_o}3/2\left(\frac{n_e}{2}\right)^{\frac{1}{2}}\frac{1}{(kT_1)}3/2\right) \tag{14.11}$$

$$f_{ii}(T_1) = \frac{g_{ii} g_e}{g_i}\left(\frac{m_e k T_1}{2\pi\hbar^2}\right)^{3/2} e^{-\frac{Q_{ii}}{kT_1}}\left(1 + \frac{e^3}{\pi\varepsilon_o}3/2\left(\frac{n_e}{2}\right)^{\frac{1}{2}}\frac{1}{(kT_1)}3/2\right) \tag{14.12}$$

where g is the statistical weight defined as,

$$g = \sum_i (2J_i+1)\, e^{-\frac{\varepsilon_i}{kT_1}} \tag{14.13}$$

The values of J_i and ε_i - the angular momentum quantum number and the corresponding energy relative to the ground state respectively - can be found in spectroscopic tables (see Moore (1949)). The statistical weights are presented in Table XIII for a temperature T_1 of 1.5 ev. or approximately 1.8×10^{4}°k.

g_e	2
g_o	1
g_i	6.0
g_{ii}	10.4

TABLE XIII

VALUES OF STATISTICAL WEIGHTS

The last term in the final bracket of equations 14.11 and 14.12 is a correction term which arises from the Stark effect in the plasma, i.e. there is a distortion of the atomic energy levels and a resulting change in the ionization potential due to the free electric charges in the plasma. In the calculations we will assume the correction term is small, but we must cheque this assumption with the resulting value of n_e. A basic assumption implied by the use of Saha's equation is that of thermal equilibrium in the region behind the shock front. We do not have sufficient information to check this assumption and thus the accuracy of this solution can not be determined without additional information about ionization relaxation times in argon.

In terms of α and β, the Saha equations (14.9 and 14.10) may be written,

$$\frac{\alpha^2 n}{(1-\alpha)} = f_i(T_1) \qquad 14.14$$

$$\beta\left(\frac{\alpha+2\beta}{\alpha}\right)n = f_{ii}(T_1) \qquad 14.15$$

14.0 DYNAMIC EQUATION FROM SHOCK WAVE MODEL (CONT'D.)

Since,

$$n = \frac{p_1}{(1+\alpha+2\beta)\, kT_1} \qquad 14.16$$

we have,

$$\frac{\alpha^2}{(1-\alpha)\,(1+\alpha)} = \frac{kT_1}{p_1}\, f_{i\chi}(T_1) \qquad 14.17$$

and,

$$\frac{\beta(\alpha+2\beta)}{\alpha(1+\alpha+2\beta)} = \frac{kT_1}{p_1}\, f_{ii}(T_1) \qquad 14.18$$

Thus we have determined six equations - 14.1, 14.3, 14.6, 14.8, 14.17, and 14.18 - for the six unknown variables - ρ_1, V_F, p_1, α, β, T_1.

14.1 GRAPHICAL SOLUTION OF SHOCK WAVE EQUATIONS

In the previous section we have arrived at a system of six equations for six unknowns. In general, a solution of these equations is difficult, but in the present case a technique is possible which simplifies the solution. The technique depends upon an initial estimate of p_1 suggested from the experimental fact that the illuminated layer of the plasma does not change appreciably in thickness as the layer collapses, i.e. $V_S \gtrsim V_F$. Equation 14.3 becomes,

$$p_1 \lesssim \rho_o V_S^2 \qquad 14.19$$

With this value, graphical techniques are used to solve equations 14.6, 14.17, and 14.18, for α, β, and T. A more accurate value of p_1 is then obtained from equation 14.8 and finally V_F and

ρ_1/ρ_0 are determined from equations 14.3 and 14.1, respectively.

In this section we consider three examples for the measured values of initial pressure and shock velocity. The first example is calculated in detail and the results of all three examples are given in tabular form.

At the conclusion of this section we examine the approximations considered in section 14.0.

Example 1. 100 μHg Argon:

The discharge vessel has an initial pressure of 100 μHg argon and the shock velocity at 2.5 μsec after initiation of the discharge is 1.27×10^4 m/sec.

$$\rho_0 = 2.13 \times 10^{-4} \text{ kg/m}^3$$
$$V_S = 1.27 \times 10^{-4} \text{ m/sec}$$

We obtain an estimate of p_1 from equation 14.19,

$$p_1 \lesssim 3.44 \times 10^4 \text{ nt/m}^2$$

We let $p_1 = 3.2 \times 10^4$ nt/m^2 as our first estimate.

We assume that there are no neutral atoms in the plasma. That is,

$$\alpha + \beta = 1 \qquad 14.20$$

14.1 GRAPHICAL SOLUTION OF SHOCK WAVE EQUATIONS (CONT'D.)

Substituting equation 14.20 in equation 14.18 we eliminate β. Equations 14.18 and 14.6 are solved graphically for α and T_1 (see figure 67.). Equation 14.18 is, itself, a complicated equation which can be solved graphically in the following manner,

Equation 14.18 gives,

$$\frac{\beta}{\alpha}\left(1 + \frac{1}{\alpha+2\beta}\right)^{-1} = \frac{kT_1}{p_1}^{5/2}\left(\frac{g_{ii}g_e}{g_i}\right)\left(\frac{mek}{2\pi\hbar^2}\right)^{3/2} e^{-\frac{Q_{ii}}{kT_1}}$$

$$\text{or,}\quad e^{\frac{Q_{ii}}{kT_1}} = \frac{\alpha}{1-\alpha}\left(1 + \frac{1}{2-\alpha}\right)\frac{k}{p_1}\left(\frac{g_{ii}g_e}{g_i}\right)\left(\frac{mek}{2\pi\hbar^2}\right)^{3/2} T_1^{5/2}$$

Upon substitution of numerical values, we have,

$$e^{\frac{31.8 \times 10^4}{T_1}} = \frac{\alpha}{1-\alpha}\left(1 + \frac{1}{(2-\alpha)}\right) 0.132\, \frac{T_1}{p_1}^{5/2} \qquad 14.21$$

The R.H.S. and the L.H.S. of equation 14.21 are plotted as functions of T_1 for given values of α and p_1 in the graph of figure 66. The intersection of these curves gives α vs. T_1 for a given value of p_1. These points are transferred to figure 67., and the intersection of this curve with the curve of equation 14.6 determines the solution for α and T_1. With the value $p_1 = 3.2 \times 10^4$ nt/m^2 and the use of equation 14.20, 14.6 becomes,

$$T_1 \sim \frac{10^8}{(3-\alpha)\ 520}\left(.8 - (1.03 - .66\alpha)\right) \qquad 14.22$$

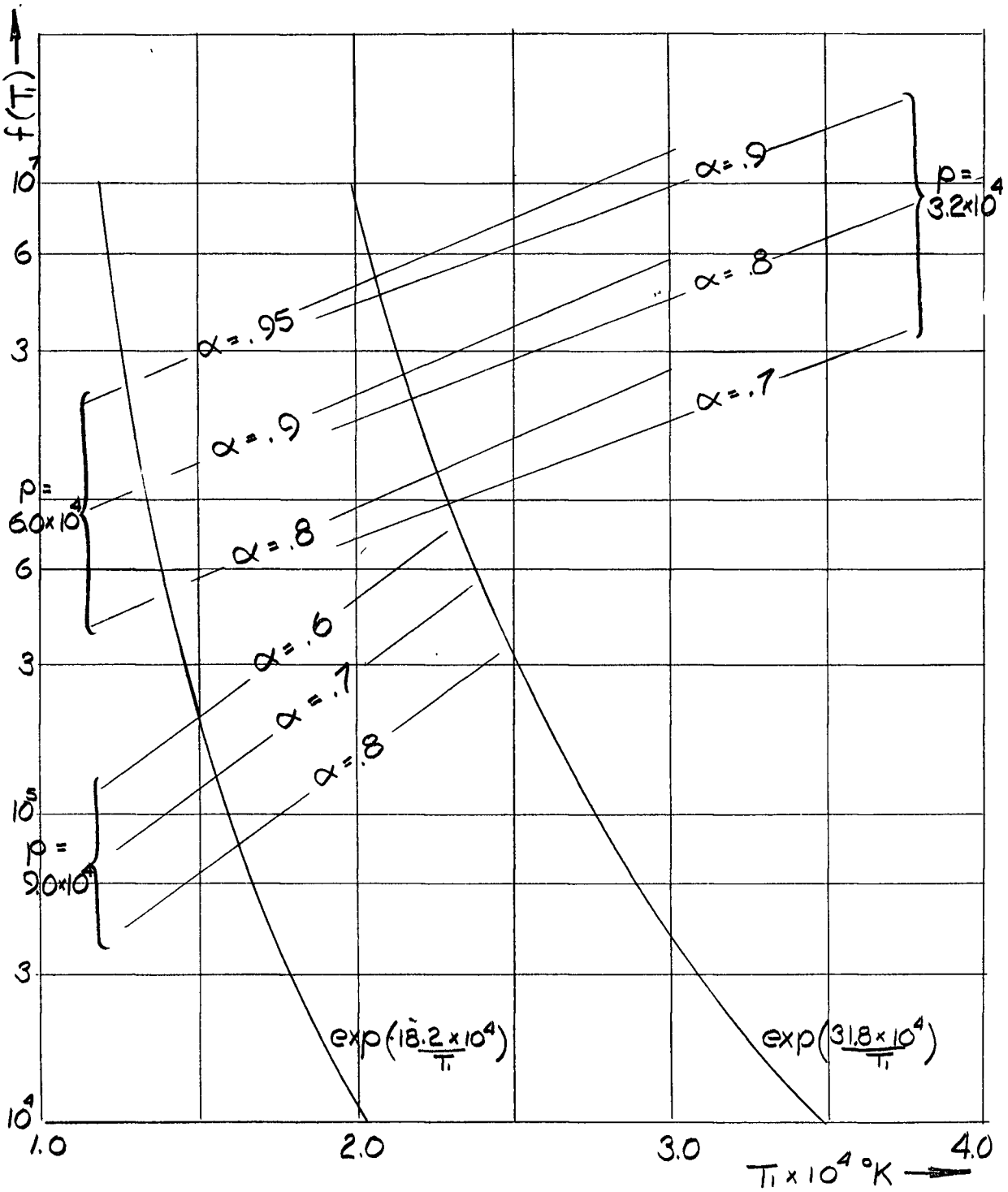

FIGURE 66. GRAPHICAL SOLUTION OF SAHA EQUATION

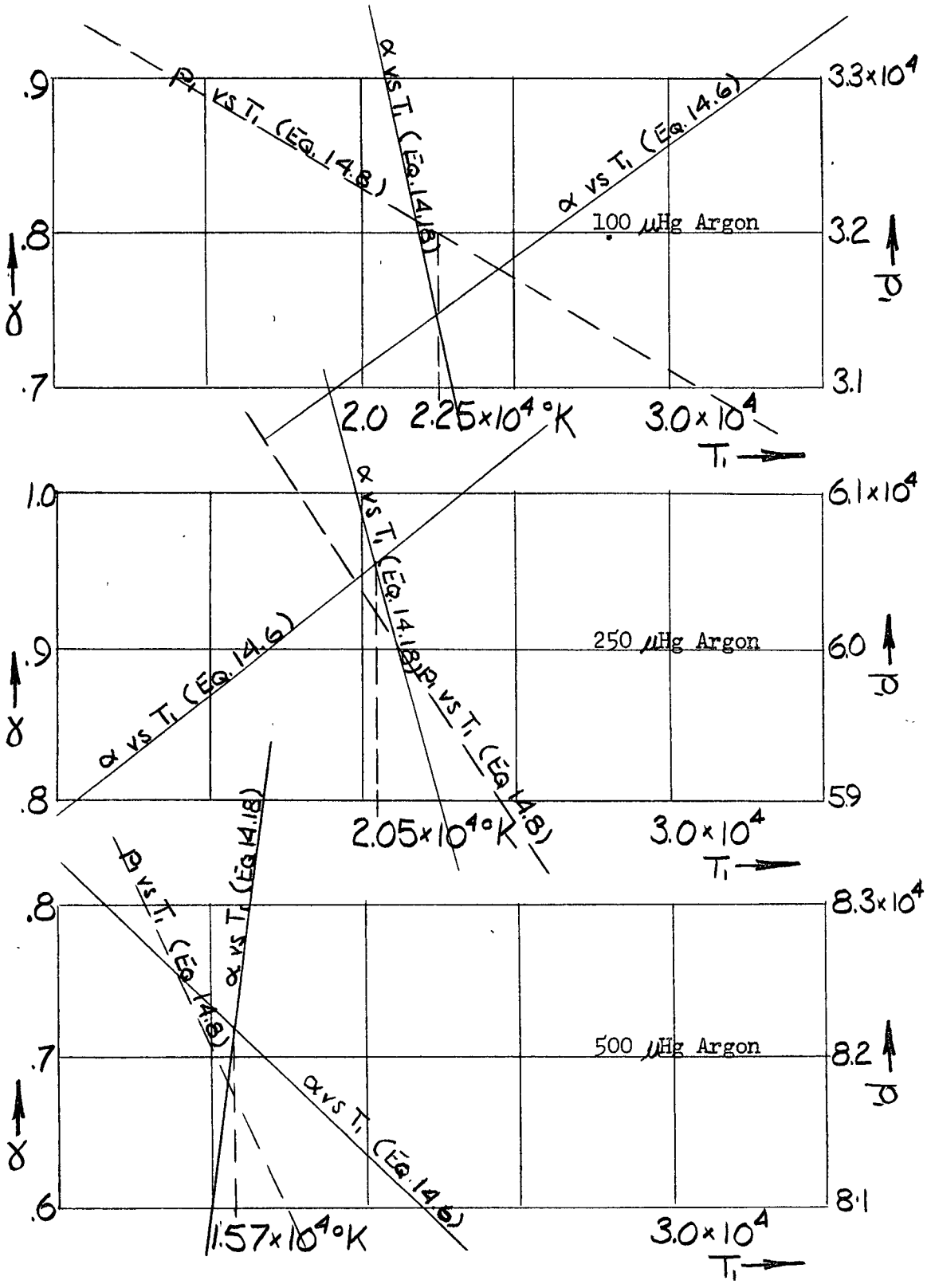

FIGURE 67. GRAPHICAL SOLUTIONS OF RANKINE-HUGONIOT EQUATIONS

14.1 GRAPHICAL SOLUTION OF SHOCK WAVE EQUATIONS (CONT'D.)

The solution is $T_1 = 2.25 \times 10^4$ °k and $\alpha = .75$. Equation 14.8 is plotted in figure 67., and the result is $p_1 = 3.20 \times 10^4$ nt/m^2 which confirms our initial estimate. From equation 14.3 we obtain $V_F = 1.18 \times 10^4$ m/sec and from equation 14.1 we obtain $\rho_1/\rho_0 = 14$. These results are presented below.

Example 1. 100 μHg Argon (2.5 μsec)

Given: ρ_0 = Initial mass density = 2.13×10^{-4} kg/m^3
V_S = Shock velocity = 1.27×10^4 m/sec

Assume: p_1 = Pressure behind shock = 3.2×10^4 nt/m^2
$\alpha + \beta = 1$

Solution: α = Fraction of singly ionized/atoms = .75
β = Fraction of doubly ionized/atoms = .25
T_1 = Plasma temperature = 2.25×10^4 °k
V_F = Pcle.velocity in flow behind shock = 1.18×10^4m/sec
ρ_1/ρ_0 = Density ratio across shock = 14
p_1 = Pressure behind shock = 3.20×10^4 nt/m^2

Example 2. 250 μHg Argon (4.0 μsec)

Given: ρ_0 = Initial mass density = 5.2×10^{-4} kg/m^3
V_S = Shock velocity = 1.12×10^4m/sec

Assume: p_1 = Pressure behind shock = 6.0×10^4 nt/m^2
$\alpha + \beta = 1$

Solution: α = Fraction of single ionized atoms = .96
β = Fraction of doubly ionized atoms = .04
T_1 = Plasma temperature = 2.05×10^4°k
V_F = Pcle.velocity in flow behind shock = 1.04×10^4m/sec
ρ_1/ρ_0 = Density ratio across shock = 14
p_1 = Pressure behind shock = 6.02×10^4 nt/m^2

14.1 GRAPHICAL SOLUTION OF SHOCK WAVE EQUATIONS (CONT'D.)

Example 3. 500 μHg Argon (5.0 μsec)

Given: ρ_0 = Initial mass density = 10.65×10^{-4} kg/m^3
V_S = Shock velocity = $.91 \times 10^4$ m/sec

Assume: p_1 = Pressure behind shock = 8.2×10^4 nt/m^2
β = 0

Solution: α = Fraction of singly ionized atoms = .72
$1-\alpha$ = Fraction of neutral atoms = .28
T_1 = Plasma temperature = 1.57×10^{4}°k
V_F = Pcle. velocity in flow behind shock = $.845 \times 10^4$ m/sec
ρ_1/ρ_0 = Density ratio across shock = 14
p_1 = Pressure behind shock = 8.18×10^4 nt/m^2

14.2 COMPARISON OF THEORETICAL AND EXPERIMENTAL RESULTS

An examination of the predicted flow velocity of particles behind the shock front shows very good agreement with the measured values obtained in section 10.1. The flow velocities are presented in Table XIV and the agreement indicates that the shock model is a reasonable approximation of our plasma.

PRESSURE (μHg)	THEORY (m/sec)	EXPERIMENT (m/sec)
100	1.18×10^4	1.15×10^4
250	1.04×10^4	1.04×10^4
500	$.85 \times 10^4$	$.85 \times 10^4$

TABLE XIV

FLOW VELOCITY BEHIND SHOCK

14.2 COMPARISON OF THEORETICAL AND EXPERIMENTAL RESULTS (CONT'D.)

From the density ratio which has been calculated from the shock wave model, together with the assumption that all the initial gas is swept up by the collapsing plasma (see section 13.2), we can calculate the thickness of the shock heated layer of plasma. This value may then be compared with the observed plasma thickness.

PRESSURE (μHg)	TIME (μsec)	r_s (mm)	THEORY (mm)	EXPERIMENT (mm)
100	2	48	2.5	14
100	3	32	5.0	19
250	3	49	2.4	10
250	4	46	2.7	14
500	3	54	1.8	13
500	4	46	2.7	14
500	5	37	4.0	12
500	6	21	8.0	18

TABLE XV

THICKNESS OF SHOCK HEATED REGION

r_s is the radius of the shock front
Theoretical thickness if obtained from density ratio,

$$\text{THEORY} = \frac{\rho_0}{\rho_1} \times \frac{(r_o^2 - r_s^2)}{2\ r_s}$$

Experimental thickness is obtained from figures 37. - 42., as thickness of plateau region.

The large discrepancy shows that the plateau region (also the luminous region) is not shock heated. The shock heated region is very small and we find that we have a thin sheet of high mass density as was assumed in the snowplow model. However, we must explain the presence of the thick luminous layer which we have also shown to contain the majority of the discharge current. In the following section we propose a new model for the collapse stage of the z-pinch discharge.

ASSUMPTIONS

In this section we have made two assumptions which we now wish to justify. First, we assumed that the variation of the magnetic field is negligible at the shock front (equation 14.3). The thickness of the shock heated plasma is approximately 4 mm. as may be seen from Table XV. Over this distance the magnetic field varies by approximately .05 wb/m^2 and this corresponds to a pressure of about 10^3 nt/m^2. This pressure is negligible compared to the particle pressure of 5×10^4 nt/m^2.

The second assumption involves the neglect of the stark effect in Saha's equations i.e. we assume,

$$\frac{e^3}{\pi\epsilon_0}^{3/2} \left(\frac{n_e}{2}\right)^{\frac{1}{2}} \left(\frac{1}{(kT_i)}\right)^{3/2} < 1$$

Using the calculated values of the n_e and T_i, this term is approximately .08 for all examples considered here. That is, we have an error of approximately 8% in our theoretical values. This is also the range of accuracy of our experimental observations.

15.0 PROPOSED MODEL OF THE Z-PINCH DISCHARGE

In the previous section we have considered the simple shock theory with the inclusion of ionization effects. Experimentally we have observed the presence of the shock front, (see figure 55.). The simple shock theory does predict the flow velocity successfully (see Table XIV). In this section we propose an extension of the shock wave model.

The key to this model is an observation by Folkierski (1963). He reports the presence of an unexplained discontinuity between the shock front and the outer edge of the plasma column. We now suggest that the first region (between the shock front and the discontinuity) is a region of shock heated gas. This region has a high density (approximately 1½x the initial density) and a relatively low temperature (approximately 2 ev.). We suggest that the second region (the remainder of the luminous plasma layer) is a region of low density (approximately equal to the initial density) and high temperature (approximately 6 ev.). These suggestions are in agreement with the luminosities observed by Folkierski; the first region is weakly luminous while the second region is strongly luminous (see figure 68.).

Later in this section we will pursue the implications of this model and we will show that it explains the observed effects in a consistent manner. However, we would first like to give a plausible explanation for the origin of this double layered plasma column. We suggest that in the early stage of the discharge, the discharge current occurs in a region near the walls of the discharge

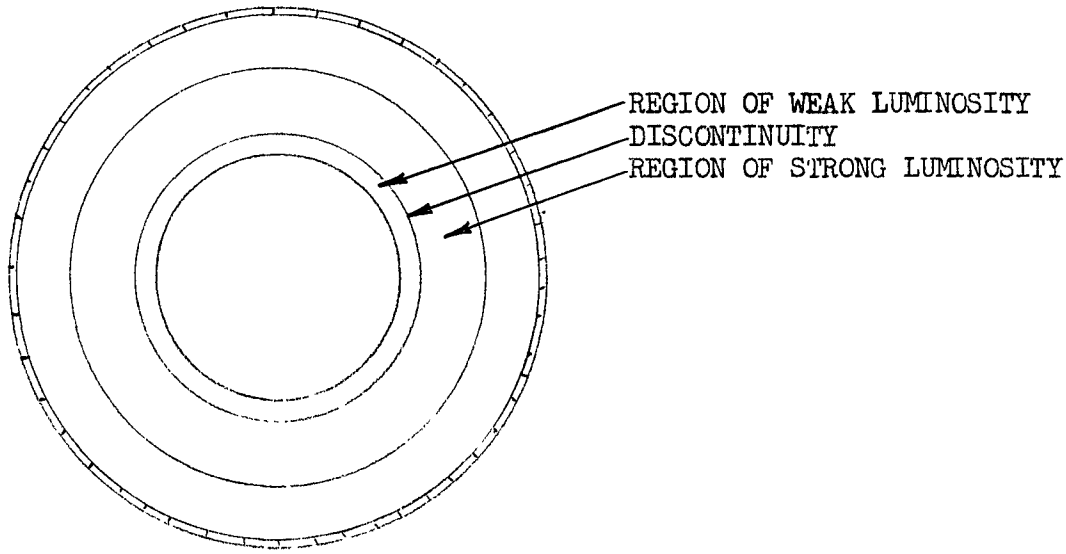

FIGURE 68. DISCONTINUITY IN PLASMA COLUMN

15.0 PROPOSED MODEL OF THE Z-PINCH DISCHARGE (CONT'D.)

vessel. As the conductivity of the plasma is low at this time, there is considerable Joule heating of the gas. This hot region at the wall expands, forming a shock heated region in front of it, and then both the Joule heated and shock heated regions are forced to constrict toward the axis of the discharge vessel under the influence of the magnetic pressure. Thus, in terms of the snowplow model, we have inserted a buffer region of low density, high temperature plasma between the mass layer and the magnetic pressure. If the thickness of the buffer region is small compared to the radius of the discharge vessel, then there will be negligible effect upon the predicted snowplow results. If the thickness of the buffer region is appreciable, then for a given position of the current density maximum, the collapsing plasma is more heavily mass loaded than the theory predicts. Hence it collapses more slowly than predicted.

15.0 PROPOSED MODEL OF THE Z-PINCH DISCHARGE (CONT'D.)

In the remainder of this section we wish to examine the experimental results in terms of this particular model. We assume that the shock theory of section 14 is applicable to the shock heated region of our model, and the results computed there are assumed correct for the first region of our double layered plasma. We wish to examine the Joule heated region in this section, and we begin with a discussion of the measured electric field in the Joule region. This electric field has been calculated from our magnetic probe results (see Table VIII), and we repeat the essential results in Table XVI below. There are several unusual features which should be observed. The apparent conductivity (J_z/E'_z) increases with increasing pressure and, furthermore, for low pressures the apparent conductivity decreases with increasing time. Both of these effects are physically improbable.

PRESSURE (μHg)	TIME (μsec)	E'_z (v/m)	J_z (amp/m^2) x10^7	σ_A (mho/m) x10^4
100	2	1750	1.4	0.8
100	3	3100	1.8	0.6
250	3	1000	1.5	1.5
250	4	1450	2.0	1.4
500	3	420	1.7	4.0
500	4	400	1.8	4.5
500	5	320	2.0	6.3
500	6	20	1.9	10.5

TABLE XVI

APPARENT CONDUCTIVITY IN JOULE REGION

E'_z = Electric field in plasma (Table VIII)
J_z = Current density in plateau region (figure 37.-42.)
σ_A = J_z/E'_z is the apparent conductivity.

In an attempt to understand these unusual results let us consider the processes which occur in the Joule heated region of the plasma. As we have seen that the plasma is moving with a constant radial velocity at the times of interest (refer to figures 58. and 59.), we choose to view the plasma from the frame of reference moving with this radial velocity.

We have seen in Table XVI that the axial electric field E_z' is not zero in this frame of reference, and with crossed E and B fields we can expect a Hall effect. The $\underline{E} \times \underline{B}$ force acts upon both electrons and ions and tends to move them both radially inward. Because of these drifts a pressure gradient is established which exerts an outward force on both electrons and ions. However, the mobility of the electrons is much greater than the mobility of the ions and thus we obtain a net force on the electrons in an inward direction and a net force on the ions in an outward direction. The plasma is at rest in this particular frame of reference and these opposing forces must be balanced by a space charge electric field which keeps the ions and electrons from separating. Thus we have a radial electric field.

Now in exactly the same way, this radial electric field, crossed with the magnetic field, results in a drift of particles in the axial direction. The difference of particle mobilities results in the creation of an axial space charge electric field. A diagram illustrating the directions of these fields and forces is given in figure 69.

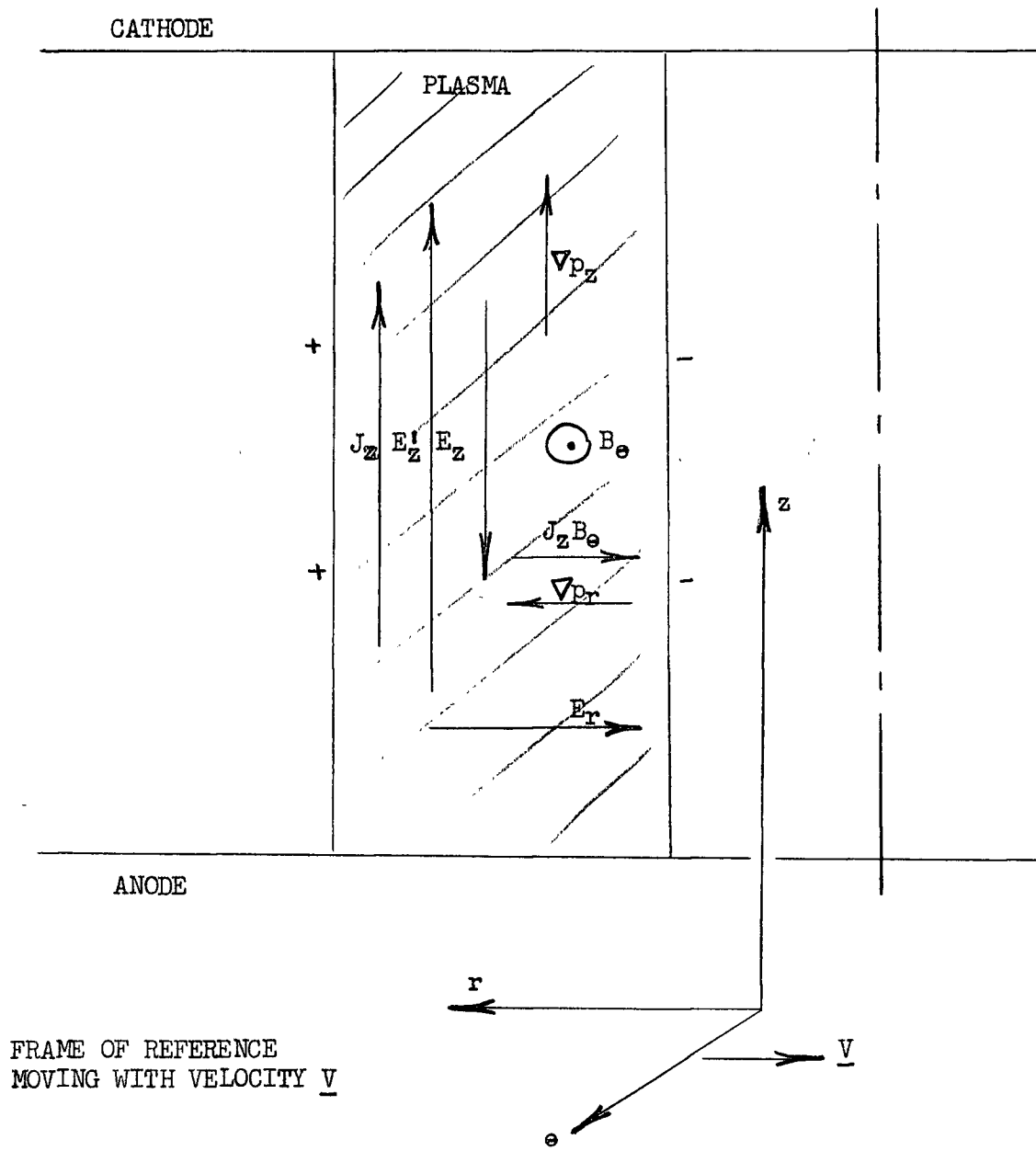

FIGURE 69. ELECTROMAGNETIC FIELDS IN THE JOULE REGION

B_θ	Magnetic Field
J_z	Current Density
E'_z	Induced Axial Electric Field
E_z	Space Charge Axial Electric Field
E_r	Space Charge Radial Electric Field
∇p	Pressure Gradient

15.0 PROPOSED MODEL OF THE Z-PINCH DISCHARGE (CONT'D.)

If we return to section 10.2 where we originally calculated E_z', we see that we made the assumption that the space charge electric fields were negligible. If this assumption is incorrect, then we must recalculate E_z' and this may account for the discrepancies observed in the apparent conductivity which have been discussed.

We can obtain an estimate of the radial electric field from our experimental measurements, for we know that the plasma is moving with constant velocity (see figures 58. and 59.)

We consider a Lorentz approximation of the plasma (Spitzer (1956) pg.83) i.e., the ions are at rest in this frame of reference and the electrons do not interact with one another. The electrons, however, have no net radial motion in this frame and hence the net force on the electrons must be zero. That is,

$$J_z B_\theta - \nabla_r p - n_e e E_r = 0 \qquad 15.1$$

If we use the fact that,

$$\underline{J} = \frac{1}{\mu_0} \nabla \times \underline{B} \qquad 15.2$$

and if we integrate the above expression through the thickness of the plasma, we have

$$\left(\frac{B^2(r)}{2\mu_0} + p(r) \right) \Bigg|_{r = r_{in}}^{r = r_{out}} - \int_{r_{in}}^{r_{out}} n_e \, e \, E_r dr = 0 \qquad 15.3$$

15.0 PROPOSED MODEL OF THE Z-PINCH DISCHARGE (CONT'D.)

PRESSURE (μHg)	TIME (μsec)	r_{in} (m)	r_{out} (m)	$B(r_{in})$ (wb/m^2)	$B(r_{out})$ (wb/m^2)
100	3	.040	.051	.30	.49
250	4	.040	.052	.30	.50
500	5	.037	.052	.23	.50

PRESSURE (μHg)	$p(r_{in})$ (nt/m^2) x10^4	$B^2(r_{in})/2\mu_o$ (nt/m^2) x10^4	$B^2(r_{out})/2\mu_o$ (nt/m^2) x10^4	p_E (nt/m^2) x10^4
100	3	3.5	9.5	3
250	6	3.5	10	.5
500	8	2	10	.0

TABLE XVII

ELECTRIC FIELD PRESSURE

where r_{in} and r_{out} are the radial position of the inner and outer edge of the luminous plasma as determined from figure 54. That is, the difference between the sum of kinetic and magnetic pressures evaluated at the outer and inner plasma boundaries gives a measure of the "electric field pressure".

$$\langle p_E \rangle = \langle n_e e\ (r_{out} - r_{in}) E_r \rangle = \frac{B^2(r_{out})}{2\mu_o} - \frac{B^2(r_{in})}{2\mu_o} - p(r_{in}) \qquad 15.4$$

Since we assume that the plasma sweeps up all of the initial gas there can be no particles outside the plasma column, and thus the kinetic pressure at the outer plasma boundary must be zero.

The value of the kinetic pressure at the inner boundary is determined from the shock wave model of section 14.2. The values of $B(r_{in})$ and $B(r_{out})$ may be determined from figures 43. - 45. The calculation is presented in Table XVII and it may be seen that the effect of the radial electric field is negligible for the case of 500 μHg, but the effect increases with decreasing pressure until the radial field has an effect upon the plasma which is comparable to the kinetic pressure for the case of 100 μHg. Certainly in this latter case we are not justified in neglecting space charge electric fields effect.

Since we can neglect space charge effects in the investigation of plasma dynamics for the plasma created in 500 μHg initial pressure of argon, we choose this case for our study of the Joule heated region. In particular, we wish to show that the Joule heated region is one of high temperature and low density compared to the shock heated region.

High Temperature:

In the 500 μHg case, the apparent conductivity as determined from Table XVI is:

$$\sigma_A = \frac{J_z}{E'_z} = 5 \times 10^4 \text{ mho/m} \qquad 15.5$$

and this corresponds to the conductivity considered by Spitzer ((1956) pg. 84):

$$\sigma = \frac{T^{3/2}}{250} \quad \text{mho/m} \qquad 15.6$$

Therefore, we obtain an estimate of the temperature in the Joule heated region of approximately 5.3×10^{4}°k. The experimentally observed conductivity is constant over the whole Joule region. (Refer to calculation of E_z' as a function of radius (Table VIII)), and graphs of J_z as a function of radius (figures 37. - 42.). This constant conductivity implies then, that there is a constant temperature in the Joule region. The temperature is high compared with the shock heated gas which has a temperature of 1.6×10^{4}°k (see Example 3., section 14.2).

Low Density:

If we can neglect space charge effects, we can also determine the radial dependence of the kinetic pressure (p), and hence the radial distribution of the particle density (n_j) in the Joule heated region.

$$n_j(r) = \frac{p(r)}{(1+\alpha+2\beta+\cdots)\, kT} \qquad 15.7$$

where
- k is Boltzmann's constant
- T is the particle temperature
- α, β are the degrees of single and double ionization respectively.

15.0 PROPOSED MODEL OF THE Z-PINCH DISCHARGE (CONT'D.)

Low Density: (Cont'd.)

As the radial electric field can be neglected, we have,

$$\nabla \left(\frac{B^2(r)}{2\mu_o} + p(r) \right) = 0$$

or,

$$\frac{B^2(r)}{2\mu_o} + p(r) = \text{constant} \qquad 15.8$$

We can determine the constant by evaluating the left hand side of the equation at the discontinuity between the Joule and shock heated regions. The kinetic pressure $p(r_D)$ is equal to the shock measured pressure of section 14.2. This last statement follows from the fact that the plasma is unaccelerated and hence the pressure must be constant across the discontinuity. Since we will show that the shock heated region is very thin, we make a negligible error in the magnetic field if we evaluate the field at the radial position of the "knee" of the current density curves (see figures 37. - 42.). We call this value $B(r_D)$.

Thus at 500 μHg:

$$\frac{B^2(r_D)}{2\mu_o} + p(r_D) = \text{constant} = \frac{(.23)^2}{8\pi \times 10^{-7}} + 8.2 \times 10^4 = 10.3 \times 10^4 \text{ nt/m}^2$$

In figure 70., we have sketched the radial dependence of the various parameters which we are considering in this section. We know that the magnetic field increases linearly with radius through the Joule region from figures 43. - 45.

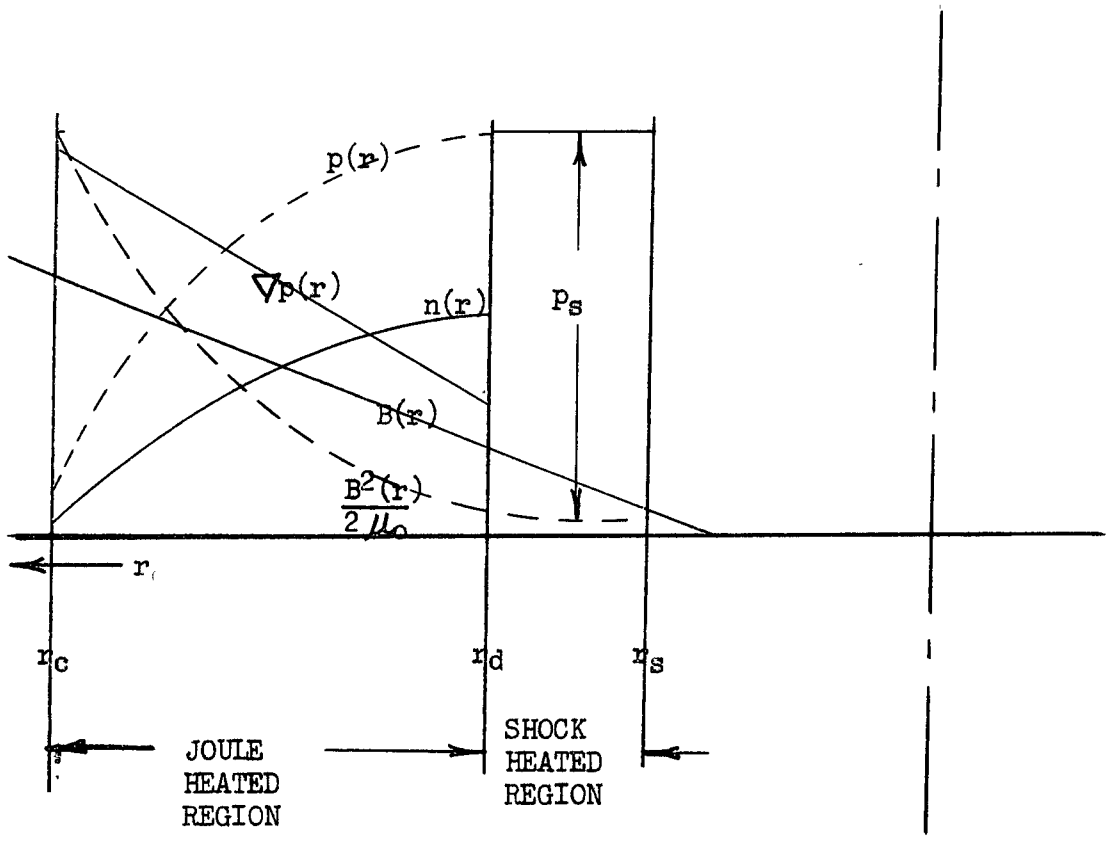

FIGURE 70. PLASMA PARAMETERS IN JOULE HEATED REGION

15.0 PROPOSED MODEL OF THE Z-PINCH DISCHARGE (CONT'D.)

Low Density: (Cont'd.)

For our special case of 500μHg at 5μsec after initiation of the discharge, we have,

$$B(r) = (18\ r - .44)\ wb/m^2 \qquad 15.10$$

where r is the radial position in meters.

Thus the kinetic pressure is given by equations 15.8, 15.9, and 15.10, as:

$$p(r) = 10.3 \times 10^4 - \frac{(18r - .44)^2}{8\pi \times 10^{-7}} \qquad 15.11$$

15.0 PROPOSED MODEL OF THE Z-PINCH DISCHARGE (CONT'D.)

Low Density: (Cont'd.)

If we use the value of temperature estimated above, and if we assume that the plasma is 100% doubly ionized argon (i.e. $\alpha = 0$, $\beta = 1$) then we can evaluate the particle density as a function of radius from equations 15.7, and 15.11.

$$n_j(r) = \frac{1}{3kT}\left(10.3 \times 10^4 - \frac{(18r - .44)^2}{8\pi \times 10^{-7}}\right) \qquad 15.12$$

Actually we wish to evaluate an average particle density for the Joule heated region.

$$\langle n_j \rangle = \frac{2\pi}{3AkT}\int_{r_D}^{r_C}\left(10.3 \times 10^4 - \frac{(18r - .44)^2}{8\pi \times 10^{-7}}\right) r\,dr \qquad 15.13$$

where A is the annular area bounded by
r_D = the radial position of the discontinuity
and r_C = the radial position of the current maximum

$$\langle n_j \rangle = .91 \times 10^{21}\int_{.037}^{.049}\left(10.3 \times 10^4 - \frac{(18r - .44)^2}{8\pi \times 10^{-7}}\right) r\,dr = 2.46 \times 10^{22}\,m^{-3}$$

The initial particle density n_o is known and thus we can determine the density ratio for the Joule heated region as:

$$\frac{\langle n_j \rangle}{n_o} = \frac{2.46 \times 10^{22}}{2.0 \times 10^{23}} = .1$$

15.0 PROPOSED MODEL OF THE Z-PINCH DISCHARGE (CONT'D.)

Low Density: (Cont'd.)

Hence the density ratio is indeed low compared to the shock heated density ratio of 14. (See Example 3., section 14.2).

The previous discrepancy in the particle density has arisen from the fact that the shock model calculations have predicted a density ratio of 14 while the observations give a value of approximately 4. This observed value can be determined from a measurement of the thickness of the plasma column. (If we assume that all of the initial gas has been swept up by the plasma.) That is,

$$\frac{\langle n \rangle}{n_b} = \frac{(r_o^2 - r_s^2)}{(r_o^2 - r_s^2)} \qquad 15.14$$

where r_o is the inner radius of the discharge vessel
r_c is the radius of the current maximum
and, r_s is the radius of the shock front.

For our particular case of 500 μHg at 5 μsec, we have,

$$\frac{\langle n \rangle}{n_b} = \frac{(.075^2 - .037^2)}{(.049^2 - .037^2)} = 4$$

Now we can resolve this discrepancy if we assume that we have a relatively thin, high density shock heated region and a thick, low density Joule heated region. In order to obtain the observed average density of the plasma, we estimate that the shock heated region forms

Low Density: (Cont'd.)

approximately 20% of the total plasma volume and the Joule heated region forms the remaining 80%. We expect a similar Joule heated region will explain the apparent density ratio discrepancy for the cases of 100 μHg and 250 μHg initial pressure. The shock theory predicts a density ratio of 14 for both cases (see section 14.2) while the observed value is 5 for 100 μHg and 4 for 250 μHg.

PART IV

CONCLUSIONS

16.0 DISCUSSION OF RESULTS

In Part I we have investigated the perturbation of the magnetic field by the probe which performs the measurement. This probe perturbation can not be neglected. An analogue experiment has been used to obtain a correction which compensates for this perturbation. This correction agrees extremely well with the theoretically determined correction given by Malmberg (1964) for the case of a plane current sheet.

A numerical procedure has been developed for the application of this correction to the measured magnetic field in the z-pinch discharge. This identical procedure can be used for any z-pinch or inverse pinch device. A feature which greatly simplifies this procedure is our use of a guide tube for the probe which is placed diametrically across the discharge vessel. The probe moves inside this guide tube and hence the perturbation is independent of the probe position.

The numerical computation is extended to determine the unperturbed current density distribution. We have tested the accuracy of this numerical program by using one of the measured magnetic fields from the analogue experiment. The resulting current density distribution should then be a δ- type current distribution at the radius corresponding to the current sheet. This test shows that the numerical approximation is quite poor. The computed current density maximum is only one quarter of the true current density, and there is a corresponding increase in the width

of the current distribution. Even so, this correction procedure increases the current maximum and decreases the current width by approximately 50% compared with the uncorrected calculations. This correction procedure gives a significant improvement in the detail of the current density distribution. Compare our results with, for example, those of Burkhardt (1958).

This improvement in measuring technique allows us to observe two features of the current density distribution which have not been observed by previous investigators of the z-pinch discharge. We observe a distinct maximum or peak in the current density at the outer edge of the plasma column. We also observe a "plateau" region in the current density. This is a region of constant current density which extends over the entire thickness of the luminous plasma. We will now discuss these two features.

A careful examination of possible error has been given in section 8.3 where we have shown that the measured magnitude of the current density peak is a lower limit of the true current density peak. Indeed, this measured peak may represent a very high, very thin spike in the true current density distribution. Since the mean free path for electrons in the Joule heated region (high temperature, low density) is large (several centimeters), and since the particle density is particularly low at the outer edge of the plasma (see figure 70.), this high current density may represent a beam of runaway electrons. (See Kruskal (1964)).

Note that this current peak is not due to a skin depth phenomenon as has been assumed in the snowplow and shock wave models. We have seen that the concept of skin depth requires careful examination for the case of a plasma which can create space charge electric fields. These fields can cancel the applied electric field in such a way that the plasma "sees" a constant electric field. Thus $w \rightarrow 0$ in the skin depth formula and the skin depth $\delta \rightarrow \infty$.

It is this rearrangement of electric fields in the plasma which allows the creation of the plateau region in the current density distribution. The magnitude of the current density over the plateau region is limited by the external circuit parameters of the discharge circuit rather than by any property of the plasma itself. The current density in this region is approximately 2×10^7 amps/m^2 for all initial gas pressures which have been used in this investigation.

An important result follows from the fact that the electric field as seen by the plasma is approximately constant with time. In this situation it is easy for the current to diffuse into the centre of the cylindrical current sheet. This is a disadvantage as far as heating the plasma is concerned for this means that a large fraction of the total current is inside the position of the shock front and thus has only a small influence upon the motion of the plasma. Experimentally, we have observed that approximately one third of the total discharge current lies inside the radius of the mass sheet. This effect

explains the discrepancy between observed and predicted collapse curves as reported by Curzon (1963a.). Their calculations predict a plasma collapse which is too rapid because they have assumed that the total discharge current causes the constriction. The same effects have been observed in the present investigation and they are discussed in detail in section 13.2.

In Part III of the thesis we have examined theoretical models of the z-pinch discharge. The snowplow gives a reliable prediction of the discharge current and the plasma radius as functions of time for the two cases of higher initial pressure (250 and 500μHg argon). At 100μHg argon the plasma constricts more rapidly than expected and this may be due to inefficient trapping of the gas particles at low pressures. Since particle trapping depends upon numerous atom-ion collisions, it is reasonable to expect that these collisions will be less frequent in a low density plasma.

In the shock wave model, if we can assume that we have thermal equilibrium in the region behind the shock front (and this is questionable), then we need only determine the shock front velocity and the initial gas density (or pressure) to calculate the pressure, temperature, density, degree of ionization, and the flow velocity of the plasma behind the shock front. The plane shock front theory which we have used restricts our predictions to those regions of large radius where the converging shock front is unaffected by the

cylindrical geometry. The predicted flow velocity is in excellent agreement with the measured values (see Table XIV). At 500μHg argon, where we obtain our most reliable results, we have a predicted temperature of 1.6 x 10^4°k ($\sim$1.4 ev.) and a kinetic pressure of 8.2 x 10^4 nt/m^2. The plasma is 70% singly ionized and 30% neutral argon. At 100μHg argon the plasma temperature is 2.3 x 10^4°k ($\sim$2 ev.), the kinetic pressure is 3.2 x 10^4 nt/m^2 and the plasma is 75% singly ionized and 25% doubly ionized argon. In all cases, the estimates are made when the radius of the shock front is approximately 4 cm.

For the three initial pressures which have been considered, the density ratio across the shock front is 14. Assuming that all the initial gas is swept up by the collapsing plasma, we can estimate the density ratio since we have measured the plasma thickness (see figure 53.). We obtain a density ratio of approximately 4 for the three gas presures.

To explain this discrepancy in the plasma density and to explain the high temperature ($\sim$5 ev.) which can be determined from the measured plasma conductivity, we have proposed an extension to the shock wave model. We suggest that the plasma consists of two layers. The inner layer corresponds to the shock heated plasma and the outer layer, which is much larger in volume (approximately four times), corresponds to a Joule heated region. This outer layer has a lower density ratio (.1) and a

higher temperature (5 ev.) than the shock heated region. The term "Joule heated" is used because we believe that this region is created during the initial stages of the discharge when the conductivity is low and Joule heating is, therefore, appreciable (see section 15.0).

The particle density and temperature in the Joule heated region could only be calculated for the investigations performed in an initial gas pressure of 500μHg argon. In this case we could neglect the effects of the radial electric field compared with the effect of the pressure gradient. It has been shown, however, that the radial electric field can not be neglected in investigations at lower initial pressures. In these cases the dynamics of the z-pinch is very complex and much more experimental investigation is required.

17.0 FINAL CONCLUSIONS

We divide our final conclusions into two classes - those which present an improvement in diagnostic technique and those which present new physical understanding of the dynamics in the z-pinch discharge.

DIAGNOSTIC TECHNIQUES

1. We have developed a high frequency, low noise magnetic probe and measuring circuit (section 3).

17.0 FINAL CONCLUSIONS (CONT'D.)

DIAGNOSTIC TECHNIQUES (CONT'D.)

2. We have developed a numerical program which corrects the measured magnetic field for the error due to the non-conducting hole in the plasma caused by the magnetic probe (section 5).

3. We have obtained an analytic solution to the snowplow equation which facilitates comparison of theory with experiment (section 13.1).

NEW PHYSICAL CONCEPTS

1. The region of high luminosity observed in photographs of the pinch coincides with the region of high current density - within our experimental error of $\pm$ .25 cm. (section 10.1).

2. There is a sharp maximum in the current density distribution at the outer edge of the plasma shell (section 8.2). This current peak is not due to skin depth effects, but is probably a current of runaway electrons (section 16).

3. There is a region of constant current density and constant axial electric field (as functions of radius)in the collapsing plasma shell. This is approximately 1 cm. thick for initial gas pressures ranging from 100 to 500μHg argon (section 8.2).

17.0 FINAL CONCLUSIONS (CONT'D.)

NEW PHYSICAL CONCEPTS (CONT'D.)

4. A large portion of the discharge current flows through the region inside the plasma shell and thus has little effect upon the plasma dynamics. For initial gas pressures of 100 - 500 μHg argon, this fraction is approximately one-third of the total current (section 13.2).

5. At the higher initial gas pressures (250 and 500 μHg argon) it is reasonable to assume that the plasma shell sweeps up all of the initial gas as it collapses. This is not a good assumption for lower initial gas pressures (100 μHg argon) (section 13.2).

6. The collapsing plasma shell actually consists of two separate regions. The inner region occupies approximately 20% of the total plasma volume and it has a relatively high particle density and low temperature. The remaining plasma volume forms the outer region which has a high temperature and a low particle density (section 15).

7. For the particular case of an initial gas pressure of 500 μHg argon, the temperature in the inner region has reached 1.6×10^{4} k and the temperature in the outer region has reached 5.3×10^{4} k at 5 μsec after initiation of the discharge. At the same time the particle density ratios are 14 and .1, respectively, as compared with the initial density (section 15).

18.0 PROPOSALS FOR FUTURE WORK

Perhaps the most remarkable result of the present investigation is the awareness of the complex nature of the z-pinch. However, the z-pinch is still simple compared to other experimental plasmas because of its well defined geometry and its high degree of reproducibility. These features make it an ideal plasma source to further consider the effects which we have observed in this investigation.

For example, there has been no experimental investigation of the initial stages of the z-pinch. In the very early stages of the pinch we have observed typical "Mach lines" which result from, most probably, a beam of electrons (see figures 51. and 52.). It has been shown that a reversal of polarity of the discharge electrodes still results in a flow from cathode to anode. From the photographs it appears that this flow of particles occurs at a distinct radial position - not uniformly. The effect might be caused by a radial distribution of electrons which falls off with increasing radius while the electric field rises with increasing radius because of the skin effect. The electron flow would occur at the position where the product of electron density and electric field were a maximum. It would be interesting to observe the radial position of the electron beam as a function of initial gas pressure and charging voltage.

There has been no experimental investigation of the initial formation of the discharge current at the vessel walls. This

could easily be done with a more sensitive magnetic probe than we have used here, and there are several interesting features to investigate. The phenomena of the delayed collapse has been observed by Curzon (1963 a.). The plasma starts to collapse toward the axis, it reforms at the vessel wall, and finally it does collapse. We have also observed an "accelerated collapse". For an initial pressure of 100 μHg argon, the plasma appears to be at the vessel wall in the first photographic frame and then in the next frame ($\sim$.25 μsec) it has moved approximately 3 mm. away from the wall. It remains here for approximately 0.5 μsec and then continues to collapse.

We have suggested in the present investigation that the Joule heated region of the plasma is created at this time, and it would be interesting to study the above phenomena in terms of the various magnetic, electric, and kinetic pressure forces. For example, the $\underline{J} \times \underline{B}$ force is strongly dependent upon the experimental configuration (in particular, the inductance), but the plasma dynamics resulting from the initial acceleration of the plasma mass by the force is strongly dependent upon the mean free path of the particles in the plasma, i.e. the plasma dynamics are strongly dependent upon the initial pressure. If the pressure is high, the $\underline{J} \times \underline{B}$ force and the inertial force will be balanced mainly by a pressure gradient. If the pressure is low the two forces will be balanced mainly by an electric field. The importance of these mechanisms can vary as the mean free path varies - especially in the initial stages.

There are many interesting problems which remain to be solved before the collapse stage of the z-pinch is understood. In section 15.0 we have demonstrated the presence of space charge electric fields in the plasma but we have been unable to include these fields in a dynamic model of the z-pinch. Indeed, the plasma is even more complex, because the axial drift velocity will result in an axial pressure gradient. Thus the mass density will increase in the plasma column as we look from cathode to anode. Thus the plasma column will collapse more rapidly at the cathode than at the anode. This "taper effect" has been observed in framing camera photographs of a nitrogen plasma by Curzon (1962). This means that there may be a radial component of the current density and thus the complete generalized Ohm's law should be considered. This is given by Rose (1961), page 126, as:

$$\frac{m_e}{n_e e^2}\frac{\partial \underline{J}}{\partial t} = \underline{E}_A + (\underline{V} - \frac{\underline{J}}{n_e e}) \times \underline{B} + \frac{\nabla p}{n_e e} - \frac{\underline{J}}{\sigma}$$

where m_e is the electron mass
n_e is the electron density
e is the electron charge
$\underline{E}$ is the electric field applied to the electrodes
$\underline{V}$ is the average plasma velocity
$\underline{J}$ is the current density
$\underline{B}$ is the magnetic field
∇p is the pressure gradient
and, σ is the conductivity.

APPENDIX I

CONSTRUCTION OF MAGNETIC PROBE

In this appendix we give a detailed description of the construction of a magnetic probe. These techniques are the result of several different attempts and the final procedure is fast and simple.

1. Using #40 B. & S. copperwire, (.003 in diameter), wind a 20 turn single layer solenoid on a 1mm. diameter wire form. (The coil can be set with nail polish).

2. Bend the wire form such that the probe coil is held in the chuck of a drill press, but perpendicular to the axis of rotation. Using the drill press twist the wire leads to the probe coil until the individual twists are approximately 1mm. in length. (The twist can be made very uniform by gluing the ends of the probe leads to the ends of a cardboard strip approximately 10 cm. in length.)

3. Obtain a piece of glass tubing of $\sim$1 mm. I.D. and $\sim$2 mm. O.D., and $\sim$ 20 cm. in length. Silver this tubing using the Rochelle Salt Process as described, for example, by Strong in "Procedures of Experimental Physics". (Several tubes can be silvered at once.)

4. Check that the silver layer is much thinner than the skin depth.
For silver: $\rho = 1.6 \times 10^{-8}$ ohm - m

or, $\sigma = 6 \times 10^{7}$ mho/m.

The skin depth is approximately .04 mm. at 30 Mc/s. The thickness of the silver layer may be estimated by measuring the resistance of the layer.

CONSTRUCTION OF MAGNETIC PROBE (CONT'D.)

$$R = \rho \times \frac{\text{length}}{\text{area}}$$

where,

$$\text{area} = \pi \times \text{O.D.} \times \text{thickness.}$$

(Our experimentally measured resistance is approximately .25Ω and this corresponds to a thickness of approximately .0002 mm.)

5. Thread the probe leads through the silvered tube. Cut the perspex end piece and bolt it to the "twinax" connector as shown in figure 2. Then solder the leads from the coil to the connector - including a connection from the silvered tube to the base of the connector. TEST ALL CONNECTIONS.

6. Using tape to form a mold, pour molding epoxy resin into the region between the perspex and the connector. Form a coating of epoxy over the silvered glass tube. (The epoxy sets more rapidly when heated for several minutes.

APPENDIX II

NUMERICAL PROGRAMS IN FORTRAN LANGUAGE

In this appendix we give the numerical programs for the two equations of section 5.0. In the "J-Method" solution we solve directly for the current density distribution and we then obtain the magnetic field from the current density. In the "B-Method" solution we solve directly for the magnetic field and indirectly for the current density. The "J-Method" is perferable as the solution requires a numerical integration rather than a numerical differentiation as in the "B-Method".

Both programs require the inversion of a large (80 x 80) matrix. Two "tricks" are required. First, we multiply all elements of the matrix to be inverted by two. This is necessary as all of the initial elements are less than or equal to one and hence the initial determinant is too small to be handled by the computer. Of course, we must then multiply all the elements of the inverted matrix by two to obtain the correct inversion. Second, we perform all inversion operations in double precision format to minimize round-off error. The fortran programs are given below.

J - METHOD SOLUTION

```
$
      DOUBLE PRECISION D, DET, R, S
      DIMENSION D(80,80), C(80,80)
C     C-MATRIX INCLUDES - 1/2
      CALL ZERO (C,80,80)
      DO 10  J = 2,8
      K = J + 7
      READ (5,15) (C(I,J), I = 1,K)
10    CONTINUE
15    FORMAT (12F6.3)
      DO 20   I = 9,80
```

NUMERICAL PROGRAMS IN FORTRAN LANGUAGE (CONT'D.)

J - METHOD SOLUTION (CONT'D.)

```
      C(I-8,I) =  .01
      C(I-7,I) =  .02
      C(I-7,I) =  .04
      C(I-5,I) =  .07
      C(I-4,I) =  .13
      C(I-3,I) =  .205
      C(I-2,I) =  .305
      C(I-1,I) =  .43
      C(I,I)   = -.43
      IF (I+1.LT.81)   C(I+1,I) = -.305
      IF (I+2.LT.81)   C(I+2,I) = -.205
      IF (I+3.LT.81)   C(I+3,I) = -.13
      IF (I+4.LT.81)   C(I+4,I) = -.07
      IF (I+5.LT.81)   C(I+5,I) = -.04
      IF (I+6.LT.81)   C(I+6,I) = -.02
      IF (I+7.LT.81)   C(I+7,I) = -.01
20    CONTINUE
      DO 30  I = 1,80
      DO 30  J = 1,I
      AI = I
      AJ = J
      C(I,J) = 2.* (C(I,J) + (AJ-.5)/AI)
30    CONTINUE
C     INVERSION
      DO 40  I = 1,80
      DO 40  J = 1,80
      D(I,J) = DBLE (C(I,J))
40    CONTINUE
      DET = 1.0D0
      DO 42  K = 1,80
      DET = DET*D(K,K)
      R = 1.0D0/D(K,K)
      D(K,K) = 1.0D0
      DO 44  J = 1,80
44    D(K,J) = R*D(K,J)
      DO 42  I = 1,80
      IF (I-K) 46,42,46
46    S = D(I,K)
      D(I,K) = 0.0D0
      DO 48  J = 1,80
48    D(I,J) = D(I,J) - S*D(K,J)
42    CONTINUE
      DET = DET*D(80,80)
      DO 50  I = 1,80
      DO 50  J = 1,80
      C(I,J) = 2*D(I,J)
```

```
50    CONTINUE
      WRITE (4) C
      CALL EXIT
      END
$
C     RESULTS IN M.K.S. UNITS
      DIMENSION D(80,80), C(80,80), B(80,80),
     1 BU(80), BP(80), DENS(80), DENSP(80), CN(26)
      READ (4) C
      READ (5,20) (CN(I) I = 1,26)
15    READ (5,25) PRESS, TIME, ANORM, CURR
      READ (5,30) (BP(I) I = 1,80)
20    FORMAT (6F7.5)
25    FORMAT (4F12.4)
30    FORMAT (12F6.2)
      DO 35  I = 1,54
      BU(I) = BP(I)* ANORM
35    CONTINUE
      DO 50  I = 45,80
      BU(I) = BP(I)*ANORM + CURR * CN(I-54)/850.
45    CONTINUE
      BP(1) = BU(1)
      BP(80)= BU(80)
      DO 55  I = 2,79
      BP(I) = (BU(I-1) + BU(I) + BU(I+1))/3.
55    CONTINUE
      CALL MATVEC (C,BP,DENS,80,80)
      DO 60  I = 1,80
      DO 60  J = 1,I
      AI = I
      AJ = J
      B(I,J) = 2.*(AJ - .5)/AI)
60    CONTINUE
      CALL MATVEC (B,DENS,BU,80,80)
      DO 65  I = 1,80
      DENS(I) = .796* (10.**9)* DENS(I)
65    CONTINUE
      WRITE (6,80) PRESS,TIME
      WRITE (6,90)
      WRITE (6,100) (I,BP(I),BU(I),DENS(I), I = 1,80
      IF (PRESS.LT.500.) GO TO 15
      IF (TIME.LT.8.)    GO TO 15
80    FORMAT(1H1,20H INITIAL PRESSURE OF F6.0, 6X,16H RESULTS
      FOR T = F6.0)
```

APPENDIX II (CONT'D.)

NUMERICAL PROGRAMS IN FORTRAN LANGUAGE (CONT'D.)

J - METHOD SOLUTION (CONT'D.)

```
   90   FORMAT  (1X, 67H RADIUS   MEASURED
        FIELD    TRUE FIELD    CURRENT DENSITY)
  100   FORMAT (I6,3E20.4)
        CALL EXIT
        END
```

B - METHOD

```
        DIMENSION C(80,80), D(80,80), E(80,80)
   C    C-MATRIX INCLUDES -1/2
        CALL ZERO (C,80,80)
```

SAME AS J-METHOD

```
   20   CONTINUE
        CALL ZERO (D,80,80)
        D(1,1) = 2.
        D(2,1) = -.667
        D(2,2) = 1.333
        D(80.79) = -.994
        D(80.80) = 1.006
        DO 30  I = 3,79
        AI = I - 2
        BI = I - 1
        CI = I
        DI = I + 1
        EI = 4*I - 2
        D(I,I-2) = AI/EI
        D(I,I-1) = BI/EI
        D(I,I)   = CI/EI
        D(I,I+1) = DI/EI
   30   CONTINUE
        CALL MULT (C,D,E,80,80)
        CALL UNIT (D,80,80)
        CALL ADD  (D,E,E,80,80)
        WRITE (4) E
        CALL EXIT
        END
```

APPENDIX II (CONT'D.)

NUMERICAL PROGRAMS IN FORTRAN LANGUAGE (CONT'D.)

B - METHOD (CONT'D.)

```
$
C     RESULTS IN M.K.S. UNITS
      DOUBLE PRECISION D,DET,R,S
      DIMENSION C(80,80), D(80,80)
     1  BU(80), BP(80, DENS(80), DENSP(80), CN(26)
      READ (4) C
C     MULTIPLY MATRIX ELEMENTS BY TWO
      DO 40  I = 1,80
      DO 40  J = 1,80
      C(I,J) = 2.*C(I,J)
      D(I,J) = DBLE (C(I,J))
40    CONTINUE
      DET = 1.0D0

                                    SAME AS
                                    J-METHOD
50    CONTINUE
      READ (5,20) (CN(I)  I = 1,26)

                                    SAME AS
                                    J-METHOD
55    CONTINUE
      CALL MATVEC (C,BP,BU,80,80)
      DO 60  I = 2,78,2
      DI = I
      DENS(I) = ((DI+1.)*BU(I+1)-(DI-1.)*BU(I-1))/(8.*DI*3.14*
                10.**(-7))
60    CONTINUE
      DO 70  I = 2,78,2
      DI = I
      DENSP(I) = ((DI+1.)*BP(I+1)-(DI-1.)*BP(I-1))/(8.*DI*3.14*
                 10.**(-7))
70    CONTINUE
      WRITE (6,80) PRESS, TIME
      WRITE (6,90)
      WRITE (6,95) (I,BP(I),BU(I),DENSP(I),DENS(I), I = 2,78,2)
80    FORMAT (1H1,20H INITIAL PRESSURE OF F6.0,6X,16H RESULTS
      FOR T = F6.0)
90    FORMAT (1X,86H RADIUS  MEASURED FIELD
     1 TRUE FIELD  PERTURB DENSITY  CURRENT DENSITY)
95    FORMAT (I6,4E20.4)
      IF (PRESS.LT.500.) GO TO 15
      IF (TIME.LT.8.)    GO TO 15
      CALL EXIT
      END
```

REFERENCES

Allen, J.E. (1957) Proc.Phys.Soc. B70, 24

Anderson O.A.et.al.,(1957) Proc.3rd.International Conf.on Ionization Phenomenon in Gases(Venice),62.

Andrianov,A.M.et.al.,(1958) U.N. Peaceful Uses of Atomic Energy 31,348

Andrianov,A.M. Bazelevskaia, O.A. & Prokhorov, V.G.(1959) Plasma Physics 2,274

Burkhardt, L.C. & Lovberg,R.H. & Phillips, J.A. (1958) Nature 181,224

Curzon,F.L. & Churchill,R.J.(1962) Can.J.Phys.40,1191

Curzon,F.L.,Hodgson,R.T., & Churchill, R.J.(1963a.) Can.J.Phys.41,1547

Curzon,F.L.,Churchill,R.J., & Howard,R.(1963b.)Proc.Phys.Soc.81,349

de Hoffman,F. & Teller, E.(1950)Phys.Rev.80,692

Dippel,K.H., & Teckneberg W.(1959)4th.Ionization Conference 1,533

Ecker Von G.,Kroll, W., & Zoller (1962)Annalen der Physik 7,220

Folkierski, A., Frayne, P.G., & Latham, R.(1962) Nuclear Fusion (Supplement),627

Folkierski, A. & Latham, r.(1963)Phys.Fluids 6,1780

Gartenhaus, S.(1964)Elements of Plasma Physics (Holt Rinehart & Winston)

Harding,G.N.et.al.,(1958) U.N.Peaceful Uses of Atomic Energy 32,365

Hodgson,R.T.(1964)Ph.D.Thesis,University of British Columbia

Komelkov,V.S.,Skvortsov,U.V., & Tserevitinov,S.S.(1958) U.N. Peaceful Uses of Atomic Energy 31,374

Kruskal,M.D.,& Bernstein,I.B.(1964)Phys.Fluids 7,407

Kuwabara,S.(1963)Journal Phys.Soc. Japan 18,713

Lovberg,R.H.(1959) Ann.Phys.8,311

Malmberg,J.H.(1964)Rev.Sci.Instr.35,1622

REFERENCES
(CONT'D.)

Medley,S.S., Curzon,F.L., & Daughney,C.C.,(1965a.)Rev.Sci.Instr.36,713

Medley,S.S., Curzon,F.L., & Daughney, C.C.,(1965b.)Can. Journal Phys.43,1882

Moore, C.(1949) Atomic Energy Levels(U.S.Govt.Printing Office)

Resler,Lin & Kantrowitz, A.(1952) Journal Applied Phys.23,1398

Rose,D.J., & Clark,M.(1961) Plasma and Controlled Fusion(John Wiley & Son)

Rosenbluth,M.N.(1954) Report LA-1850 Los Alamos Scientific Laboratory, New Mexico, U.S.A.

Spitzer, L.(1956) Physics of Fully Ionized Gases(Interscience).